

Crystal Properties and Radiation Effects in Solid Molecular Hydrogens

B. J. Kozioziemski
Ph.D. Thesis

September 1, 2000

U.S. Department of Energy

Lawrence
Livermore
National
Laboratory

DISCLAIMER

This document was prepared as an account of work sponsored by an agency of the United States Government. Neither the United States Government nor the University of California nor any of their employees, makes any warranty, express or implied, or assumes any legal liability or responsibility for the accuracy, completeness, or usefulness of any information, apparatus, product, or process disclosed, or represents that its use would not infringe privately owned rights. Reference herein to any specific commercial product, process, or service by trade name, trademark, manufacturer, or otherwise, does not necessarily constitute or imply its endorsement, recommendation, or favoring by the United States Government or the University of California. The views and opinions of authors expressed herein do not necessarily state or reflect those of the United States Government or the University of California, and shall not be used for advertising or product endorsement purposes.

This work was performed under the auspices of the U. S. Department of Energy by the University of California, Lawrence Livermore National Laboratory under Contract No. W-7405-Eng-48.

This report has been reproduced directly from the best available copy.

Available electronically at <http://www.doe.gov/bridge>

Available for a processing fee to U.S. Department of Energy
and its contractors in paper from
U.S. Department of Energy
Office of Scientific and Technical Information
P.O. Box 62
Oak Ridge, TN 37831-0062
Telephone: (865) 576-8401
Facsimile: (865) 576-5728
E-mail: reports@adonis.osti.gov

Available for the sale to the public from
U.S. Department of Commerce
National Technical Information Service
5285 Port Royal Road
Springfield, VA 22161
Telephone: (800) 553-6847
Facsimile: (703) 605-6900
E-mail: orders@ntis.fedworld.gov
Online ordering: <http://www.ntis.gov/ordering.htm>

OR

Lawrence Livermore National Laboratory
Technical Information Department's Digital Library
<http://www.llnl.gov/tid/Library.html>

Crystal Properties and Radiation Effects in Solid Molecular Hydrogens

B. J. Kozioziemski
(Ph.D. Thesis)

September 2000

Crystal Properties and Radiation Effects in Solid Molecular Hydrogens

by

Bernard John Kozioziemski

B.S. (Worcester Polytechnic Institute) 1994

M.S. (University of California, Davis) 1996

DISSERTATION

Submitted in partial satisfaction of the requirements for the degree of

DOCTOR OF PHILOSOPHY

in

Engineering: Applied Science

in the

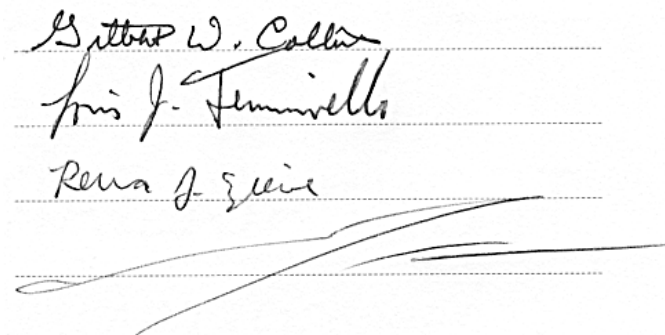
OFFICE OF GRADUATE STUDIES

of the

UNIVERSITY of CALIFORNIA

DAVIS

Approved:



The image shows three handwritten signatures on a background of horizontal dotted lines. The first signature is 'Gordon W. Collins', the second is 'Chris J. Fennivello', and the third is 'Rena J. Zieve'. Below these, there is a large, stylized signature that appears to be 'Bernard J. Kozioziemski'.

Committee in Charge

2000

Crystal Properties and Radiation Effects in Solid Molecular Hydrogens

Copyright 2000

by

Bernard John Kozioziemski

Crystal Properties and Radiation Effects in Solid Molecular Hydrogens

Abstract

The crystal lattice structure, growth shapes and helium generated by beta-decay of solid deuterium-tritium (D-T) mixtures have been studied. Understanding of these D-T properties is important for predicting and optimizing the target design of the National Ignition Facility (NIF).

Raman spectroscopy showed the D-T crystal structure is hexagonal close packed, common to the non-tritiated isotopes. The isotopic mixtures of both tritiated and non-tritiated species broadens the rotational transitions, especially of the lighter species in the mixture. The vibrational frequencies of each isotope is shifted to higher energy in the mixture than the pure components. The $J = 1-0$ population decreases exponentially with a $1/e$ time constant which rapidly increases above 10.5 K for both D_2 and T_2 in D-T. The conversion rate is nearly constant from 5 K to 10 K for both D_2 and T_2 at 7.1 hours and 2.1 hours, respectively.

The smoothing of D-T layers by beta decay heating is limited by the crystal surface energy. Deuterium and hydrogen-deuteride crystals were grown at a number of temperatures below the triple point to determine the surface energy and roughening transition. Several distinct crystal shapes were observed on a number of different substrates. The a facet roughens between $0.9 T_{TP}$ and T_{TP} , while the c facet persists up to the melting

temperature. This is very different from the behavior of the other rare gas crystals which grow completely rounded above $0.8 T_{TP}$.

Helium bubbles formed as a product of the beta decay were observed using optical microscopy and the diffusion of smaller bubbles measured with dynamic light scattering. Bubble diffusion coefficients as high as $2.0 \times 10^{-16} \text{ m}^2/\text{s}$ were measured for 10 - 50 nm bubbles. The bubbles move in response to a thermal gradient, with speeds between 1 $\mu\text{m}/\text{hour}$ and 100 $\mu\text{m}/\text{hour}$ for thermal gradients and temperatures appropriate to NIF targets.

Acknowledgements

My graduate work relied heavily on the assistance of many others who guided me through this learning experience. I would first like to thank my advisor, Gilbert Collins. His unending supply of new ideas and incredible energy kept me motivated to complete my degree. He was able to provide me with equipment, space, and manpower to complete the experiments as well as the knowledge needed to help make sense of the results. My Davis advisor, Yin Yeh, assisted me with the academic side, and provided useful insight on the light scattering measurements. Jim Sater was gracious enough to assist me with the tritium system design and operations, even though it displaced his own experiment, and discuss many other ideas. Don Bitter aided in understanding several different cryogenic design issues, as well as understanding various aspects of crystal growth. Tom Bernat and Jorge Sanchez provided many useful discussions on a wide variety of topics related to my research.

I would like to thank John Burmann, Russ Jones, Jim Pipes, and Walt Unites for their assistance in getting me up to speed working in the lab. Each has a variety of skills I needed to draw upon to design, construct, and operate each experiment. They were always willing to assist me, even though their time was in great demand. I also thank the Lawrence Livermore National Laboratory for financial support of my research and studies. And of course my family for all their support over the years.

Contents

List of Figures	vii
List of Tables	x
1 Introduction	1
1.1 General properties	3
1.2 Conventions	4
1.3 Goals	4
2 D-T crystal structure and Ortho/Para conversion	5
2.1 Background	5
2.2 Hydrogen molecules	6
2.2.1 Rotational states of hydrogen isotopes	7
2.2.2 D-T rotational conversion	8
2.3 Raman scattering	13
2.3.1 Rotational Raman spectrum	15
2.3.2 Vibrational spectrum	17
2.4 Experimental results	18
2.4.1 Experimental setup	18
2.4.2 $J=1 \rightarrow 0$ conversion rate	21
2.4.3 Rotational broadening	23
2.4.4 Vibrational transitions	32
2.5 Analysis	37
2.5.1 $J = 1 \rightarrow 0$ conversion rate	37
2.5.2 Rotational spectrum	38
2.6 Conclusions	39
3 Crystal growth and surface roughness	40
3.1 Background	40
3.2 Crystalline surface energy	45
3.2.1 Vicinal approximation	45
3.3 Roughening transition	47
3.3.1 Crystal growth	49
3.3.2 Kinetic roughening	51
3.3.3 Expected transitions	51

3.4	Experimental design	52
3.5	Experimental results	54
3.5.1	Crystals grown on copper	54
3.5.2	Crystals grown on silicon	57
3.5.3	Crystals grown on sapphire	60
3.6	Analysis	64
3.6.1	Identification of crystal planes	67
3.6.2	Surface roughness	68
3.7	Conclusions	69
4	Helium Evolution in D-T	71
4.1	Background	71
4.2	Gas bubbles in solids	76
4.2.1	Static properties: Pressure and size	76
4.2.2	Dynamic bubble properties	79
4.2.3	Diffusion calculations	83
4.2.4	Thermal migration	84
4.3	Bubble growth	87
4.3.1	Single bubble growth	89
4.4	Dynamic Light Scattering	89
4.4.1	Bubble scattering efficiency	94
4.5	Measuring correlation times	95
4.5.1	Polydisperse scattering	96
4.5.2	Application to slow systems	98
4.5.3	Self-beating, homodyne and heterodyne	99
4.6	Experimental design	102
4.6.1	Cryostat	102
4.6.2	Tritium handling system	104
4.6.3	Optical layout	105
4.7	Dynamic light scattering measurements	106
4.7.1	DLS at 19 K	107
4.7.2	DLS at 17.5K	108
4.7.3	DLS at 13 K	110
4.7.4	Temperature steps	115
4.7.5	Scattering wave vector dependence	116
4.8	Bubble growth and morphology	118
4.8.1	Coalescence	124
4.8.2	Bubbles driven by a thermal gradient	127
4.9	Analysis	133
4.9.1	Surface diffusion	133
4.10	Conclusions	134
5	Conclusions	137
	Bibliography	139

List of Figures

1.1	ICF target design	2
2.1	The diatomic molecule internal degrees of freedom	7
2.2	Rotational energy levels of hydrogens	8
2.3	J=1 molecules interacting via magnetic moment	11
2.4	Raman scattering	13
2.5	Raman experimental setup	19
2.6	Measured J=0-2 transitions in D-T	22
2.7	D ₂ in D-T J=1-3 intensity vs time	23
2.8	T ₂ in D-T J=1-3 intensity vs time	24
2.9	D ₂ and T ₂ J=1 concentration vs time	24
2.10	T ₂ J=1 population decay vs temperature	25
2.11	D ₂ J=1 population decay vs temperature	25
2.12	T ₂ and D ₂ decay constant vs temperature	26
2.13	D-T J=0-2 spectrum after 77 hours	27
2.14	Pure component J=0 D ₂ J=0-2 triplet	28
2.15	D ₂ J = 0-2 transition as H ₂ is added.	29
2.16	H ₂ J = 0-2 transition as H ₂ is added to D ₂	29
2.17	D ₂ rotational line shape as HD is added.	31
2.18	H ₂ rotational line shape as HD is added.	31
2.19	D ₂ in D-T vibrational transitions	32
2.20	T ₂ in D-T vibrational transitions	33
2.21	D ₂ in D-T vibrational energy shift with J = 1 concentration	34
2.22	T ₂ in D-T vibrational energy shift with J = 1 concentration	35
2.23	D ₂ vibrational spectrum as H ₂ is added to D ₂	36
2.24	D ₂ vibrational line as H ₂ is added to D ₂	37
3.1	Rough surface model	41
3.2	Vicinal surface	46
3.3	Macroscopic roughening transition	48
3.4	Atomic crystal surface	49
3.5	Surface nucleation	49
3.6	Growth of a crystal with a facet	51
3.7	Crystal growth cell	52
3.8	D ₂ crystals grown at 16.2 K	54

3.9	Tilted D ₂ crystals at 18.5 K	55
3.10	Flat D ₂ crystal at 18.7 K	55
3.11	HD crystal grown at 14.05 K	56
3.12	J = 0 D ₂ crystal grown at 16.65 K	57
3.13	D ₂ crystal growing at 18.68 K	58
3.14	D ₂ crystal at 18.72 K	58
3.15	D ₂ crystals display short range order	59
3.16	D ₂ crystals on Si substrate	59
3.17	HD crystal grown at 16.56 K	60
3.18	HD crystal at 16.6 K	61
3.19	Phase map of HD crystal	61
3.20	Surface profile of HD crystal	61
3.21	HD crystal at 16.6 K	62
3.22	D ₂ crystal grown at 15.7 K	63
3.23	D ₂ crystal grown at 15.7 K	63
3.24	D ₂ crystals grown at 15.7 K	64
3.25	D ₂ crystal growing near T _{TP}	65
3.26	D ₂ crystal grown on sapphire substrate	65
3.27	D ₂ crystal grown at 18.72 K	65
3.28	Neon crystals above T _R	66
3.29	Identification of crystal facets	66
3.30	Smoothing of a rough surface	68
4.1	³ He in a NIF target	72
4.2	D-T solid with ³ He bubbles at several temperatures	73
4.3	Calculated helium buildup in NIF target	74
4.4	NIF scale target with ³ He bubbles	75
4.5	Calculated number of ³ He atoms in a bubble	77
4.6	Bubble migration mechanisms	80
4.7	Calculated bubble diffusion constant	84
4.8	Calculated bubble diffusion constant vs temperature	85
4.9	Thermal migration velocity vs size	86
4.10	Thermal migration velocity vs temperature	86
4.11	Dynamic light scattering experiment	91
4.12	Illustration of dynamic light scattering source and signal	93
4.13	Bubble index of refraction	95
4.14	³ He bubble scattering cross section	96
4.15	Polynomial fit error	98
4.16	Intensity distribution with Poisson statistics	99
4.17	PMT Counting statistics	100
4.18	Cryostat dewar design	102
4.19	Cell layout	103
4.20	Palladium Bed	104
4.21	Light scattering optical layout	105
4.22	Measured scattered intensity at 19.5 K	107
4.23	Measured intensity autocorrelation at 19.5 K	108
4.24	Measured intensity distribution at 19 K	109
4.25	Measured intensity at 17.5K	109

4.26	Measured intensity autocorrelation at 17.5 K	110
4.27	Measured intensity at 13 K	111
4.28	Measured intensity autocorrelation at 13 K	111
4.29	Intensity distribution at 13K	112
4.30	Correlation time for 19 K, 17.5 K, and 13 K samples	113
4.31	Measured diffusion constants at 19 K, 17.5 K, 13 K	113
4.32	Scattering intensity change with sample heating	114
4.33	Intensity autocorrelation at 13 K, 18 K, and 19.5 K	114
4.34	Scattering intensity change with sample cooling from 17 K to 15 K	116
4.35	Intensity autocorrelation at 17 K and 15 K	117
4.36	Scattering intensity vs time using 488 nm and 830 nm light	117
4.37	^3He bubbles in D-T at 18.4 K	119
4.38	^3He bubbles in 250 μm D-T layer at 17.7 K	120
4.39	^3He bubbles in 250 μm D-T layer at 17.7 K, 7 hours	121
4.40	^3He bubbles in 80 μm D-T layer at 17.5 K	122
4.41	Bubble area vs time at 17.7 K	123
4.42	Bubble area vs time at 16.8 K	123
4.43	Bubble growth rate vs size	124
4.44	^3He bubbles coalescing	126
4.45	^3He bubble shape evolution at 17.7 K	128
4.46	Bubble position vs time	129
4.47	Bubble velocity as a function of thermal gradient	130
4.48	Bubbles trapped in D-T solid by defects	131
4.49	Bubble velocities at different temperatures and thermal gradients	132
4.50	Comparison of surface diffusion and vapor transport models	134
4.51	Modeled bubble size distribution	135

List of Tables

1.1	Physical properties of the hydrogen isotopes at the triple point	3
2.1	Rotational energy constant and $\Delta J = 2$ energies	8
2.2	Vibrational frequencies of H_2 , D_2 and T_2	17
2.3	T_2 and D_2 $1/e$ $J = 1-0$ times	26
2.4	T_2 and D_2 $J = 1-0$ decay times from NMR	27
2.5	$J = 0-2$ rotational line position	30
2.6	Measured $Q_1(0)$ and $Q_1(1)$ lines	33
4.1	Bubble diffusion variables and definitions	82

Chapter 1

Introduction

Ignition targets for inertial confinement fusion are composed of an outer spherical ablator layer with a $\approx 100 \mu\text{m}$ inner fuel layer of solid deuterium-tritium (D-T) and central core of D-T vapor, shown in figure 1.1. Non-uniformities in the ablator or D-T solid layer seed Rayleigh-Taylor instabilities during implosion.¹⁻³ These instabilities set limits on the roughness of the ablator and D-T solid surfaces for the National Ignition Facility (NIF). The D-T solid surface roughness needs to be less than $1 \mu\text{m}$ rms for successful NIF targets. In addition to the surface roughness limitations, current designs require targets with a vapor density of 0.3 kg/m^3 corresponding to the D-T vapor pressure at 18.3 K.

D-T layers are formed by beta decay heating of the tritium in the solid.⁴⁻⁶ The triton undergoes beta-decay with a half-life of 12.3 years, with ^3He , an electron, and an anti-neutrino as decay products. The electron carries a mean energy of 5 keV and subsequently causes ionization of hundreds of molecules and atoms.⁷ The energy released by the beta decay process is $\dot{Q} = 0.977 \text{ W/mole}$ for D-T. This self-heating generates a thermal gradient within the solid in a target, forcing the solid to move to minimize the overall thermal energy. The solid sublimates from thicker warmer regions to thinner cooler regions with

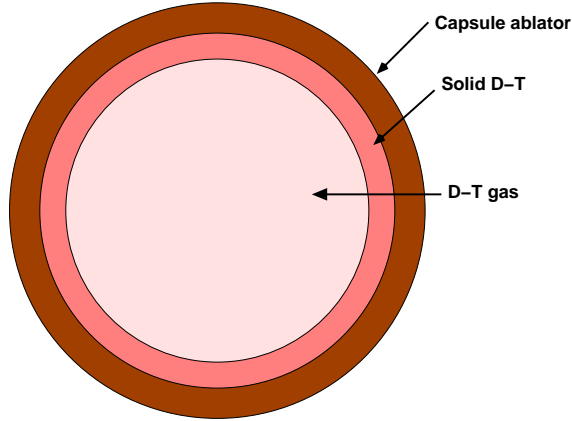


Figure 1.1: A typical NIF ignition target design. The solid D-T fuel is driven inward, compressing and heating the D-T vapor, by the radiation driven ablation of the capsule.

a time constant⁵ $\tau_{\text{DT}} = H_s/\dot{Q} \approx 30$ minutes, where $H_s = 1580$ J/mole is the D-T heat of sublimation. Recent experiments⁸ produced $100\text{ }\mu\text{m}$ thick D-T solid layers with a surface roughness as small as $1.2\text{ }\mu\text{m}$ rms. Ignoring other effects, this redistribution process would generate an extremely uniform solid layer if the ablator shell were isothermal. However, the surface energy increases when altering the surface structure and competes with the beta-layering to set a lower limit on the surface roughness.

The D-T solid often reaches a minimum surface roughness shortly after freezing. As the target ages, the roughness increases.⁹ ^3He generated by tritium decay has been suggested as a possible cause of this increasing roughness.^{6,9} The ^3He created in the solid persists as single atoms, clusters into bubbles, or escapes from the solid into the vapor. Helium in the vapor impedes the D-T diffusion and slows the redistribution of the solid, as was found experimentally by Hoffer and Foreman⁵ and predicted by Martin, Simms and Jacobs.⁴ Bubbles have been observed in the course of working with solid D-T, but a detailed study of their formation and migration has not been performed until now.

While the D-T layer shape is predominately determined by the triton heating and the isotherms in the capsule, the layer roughness depends in a complicated way on initial

nucleation and growth, surface free energy, grain boundary energy, and possibly radiation induced effects such as ^3He bubbles. These basic properties have not been investigated and are the subject of this thesis.

1.1 General properties

Isotope	T_{TP} (K)	P_{vap} (Pa)	ρ_s (m^3/mole)
H_2	13.96	7200	43200
HD	16.60	12400	45900
HT	17.70	14600	47100
D_2	18.73	17200	49000
DT	19.79	20100	50300
T_2	20.62	21600	51500

Table 1.1: Physical properties of the hydrogen isotopes at the triple point.⁷

The solid hydrogens form molecular crystals with binding energy of 1 kJ/mole.⁷ The different molecular species are mutually soluble. As such, they have relatively low triple point temperatures T_{TP} . The lattice potential parameters in a Lennard-Jones model are very close to those of the rare gases, namely neon. Most of what we know about the isotopes comes from studies on the non-tritiated isotopes. Tritiated isotope properties are estimated by scaling the mass and the quantum parameter. However, the beta decay radiation changes some properties in a non-mass related way. Radiation effects can destroy the lattice, alter rotational populations, and degrade thermal conductivity and electrical resistivity.

1.2 Conventions

Several conventions are used throughout this thesis. The first is the mixture designation. DT is used to designate a molecule composed of a deuteron and a triton. D-T, the mixture typically used in fusion research, refers to the mixture of 25% D_2 - 50% DT - 25% T_2 by number. Values of physical properties of D-T which have yet to be measured are estimated using either the mixture ratio of the properties, or simply using the DT value which often differ only slightly.⁷

Rotational populations are often referred to as either ortho or para. This notation is a bit confusing when discussing both D_2 and H_2 , where ortho refers to $J = 0$ and $J = 1$ populations, respectively. The reason for this is because the ortho designation refers to the most abundant room temperature population. In this thesis, rotational populations will be referred to as simply as either even or odd J , i.e. $J = 0$ and $J = 1$ as needed. A “normal” population signifies the room temperature $J = 1$ populations, 75% $J = 1$ for H_2 and 33% for D_2 .

1.3 Goals

This thesis explores several physical properties important for understanding D-T target performance. First, the crystal structure and rotational conversion times are measured for D-T to put our understanding on the same level as the other isotopes. Secondly, characterization of single crystal growth is made to help understand the D-T surface roughness and how beta-decay heating process symmetrizes the layers. Finally, the formation and migration of 3He bubbles from the beta decay is explored.

Chapter 2

D-T crystal structure and Ortho/Para conversion

2.1 Background

The hydrogen crystal structure is hexagonal close-packed (hcp) when grown from the vapor above 4 K or from the liquid phase.^{10,11} However, it is face-centered cubic (fcc) when grown or thermally cycled at low temperatures, if the solid is strained, or has a high $J = 1$ concentration^{10,12-14}. Additionally, Collins *et. al.* found H_2 and D_2 films deposited at $0.2 T_{TP} - 0.3 T_{TP}$ consisted of a mixture of fcc and hcp crystals, while those grown below $0.2 T_{TP}$ have a random close-packed structure.¹¹ Sullivan¹⁵ summarizes the hydrogen phase diagram $J = 1$ concentration dependence, and Silvera¹⁰ provides more detailed temperature and density dependence.

The (hcp) lattice structure is very similar to the (fcc) lattice. The molecular packing fraction is 0.74 and each molecule has twelve nearest neighbors in both structures.¹⁶ A small $\approx 10^{-3}$ K energy difference separates the two structures for H_2 , but a 100 K

energy barrier prevents transitions between the two structures.¹⁰ The lattice structure of the tritiated hydrogens, subject to constant radiation damage, ³He impurities, and a concentration of free atoms up to 1000 ppm¹⁷, is not known.

The $J=1 \rightarrow 0$ conversion rate is important for creating nuclear-spin polarized D-T, which has a 50% higher fusion cross section than the unpolarized nuclei.^{18,7,17,19} The details of the $J=1 \rightarrow 0$ process are important in producing the polarized spins^{17,19} as well as the fielding of polarized targets. Also, Collins *et. al.*²⁰ have modeled the atom diffusion constant in D-T based on the $J=1 \rightarrow 0$ conversion rate.

The Raman spectrum of the hydrogen isotopes has been investigated in detail both experimentally and theoretically for many years^{10,14,21-23}. Simple experimental design and data interpretation make Raman spectroscopy a useful characterization tool for many hydrogen properties. The Raman spectrum contains information on lattice structure, solid density, crystal orientation, and rotational population. The D-T crystal lattice structure is determined in this chapter from the $J = 0-2$ rotational Raman spectrum. The $J=1 \rightarrow 0$ conversion rate, also determined from the rotational Raman spectrum, is compared with results from previous NMR measurements.²⁰ The NMR measurements obtain the D_2 in D-T conversion rate indirectly through the T_2 NMR signal, whereas the Raman measurement directly samples both isotopes.

2.2 Hydrogen molecules

Diatomic molecules have rotational, vibrational, and nuclear spin internal degrees of freedom, illustrated in figure 2.1. The homonuclear hydrogen isotopes, H_2 , D_2 , and T_2 are subject to definite parity requirements on the molecular wave function. This parity requirement couples the internal degrees of freedom and leads to a metastable $J = 1$ rotational

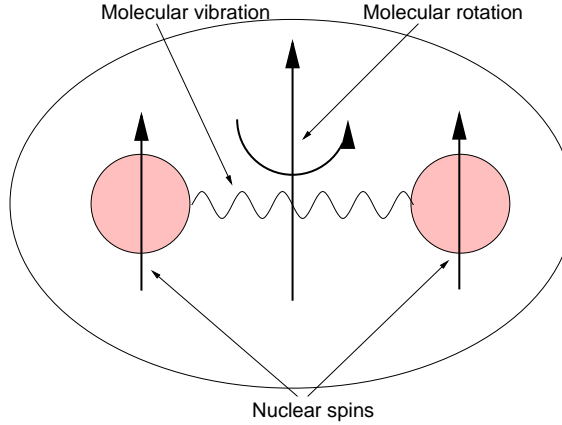


Figure 2.1: The nuclei of a diatomic molecule have rotational, vibrational, and nuclear spin internal degrees of freedom.

population at low temperatures.

2.2.1 Rotational states of hydrogen isotopes

The hydrogen isotopes are unique among molecular solids because the large intermolecular distance and small molecular interactions do not mix rotational energy states and J is a good quantum number.^{24,25} The energy of a quantum mechanical rigid rotator with moment of inertia μ in the rotational state J is

$$E(J) = \frac{\hbar^2}{2\mu} J(J+1) = B_0 J(J+1). \quad (2.1)$$

The small moment of inertia of the hydrogen molecules is responsible for the large separation in rotational energy levels. The values for B_0 and the rotational transition energies are listed in table 2.1.

The equilibrium number of molecules in a given rotational state is obtained from the Boltzmann distribution. In the low temperature and pressure equilibrium solid, nearly all molecules are in the $J = 0$ state. However, the rotational states are coupled to the nuclear spins by the wave function symmetry of the homonuclear molecules. The nuclear spin transition is forbidden, forcing rotational state changes of even ΔJ steps. Molecules

Isotope	B_0	ΔE	ΔE
		$J = 0 \rightarrow 2$	$J = 1 \rightarrow 3$
H ₂	85.3 K = 59.3 cm ⁻¹	512 K = 356 cm ⁻¹	853 K = 593 cm ⁻¹
HD	64.3 K = 44.7 cm ⁻¹	386 K = 268 cm ⁻¹	643 K = 447 cm ⁻¹
HT	57.2 K = 39.8 cm ⁻¹	343 K = 239 cm ⁻¹	572 K = 398 cm ⁻¹
D ₂	43.0 K = 29.9 cm ⁻¹	258 K = 179 cm ⁻¹	430 K = 299 cm ⁻¹
DT	35.9 K = 25.0 cm ⁻¹	216 K = 150 cm ⁻¹	359 K = 250 cm ⁻¹
T ₂	28.8 K = 20.0 cm ⁻¹	173 K = 120 cm ⁻¹	288 K = 200 cm ⁻¹

Table 2.1: Gas phase rotational energy constant B_0 and $\Delta J = 2$ transition energies for the hydrogen isotopes initially in the $J = 0$ and $J = 1$ states.⁷

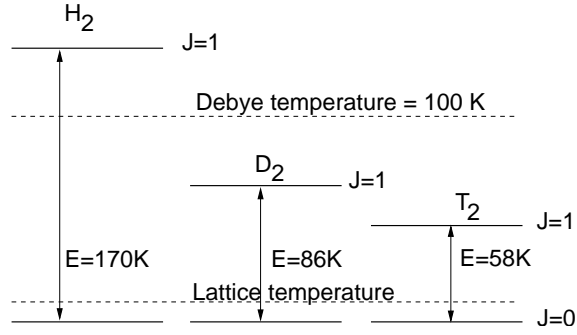


Figure 2.2: $J=1$ rotational energy of the homonuclear hydrogen molecules compared to the Debye temperature and the lattice temperature.

remain trapped in the $J = 1$ state even though the rotational energy is much larger than the lattice temperature.

2.2.2 D-T rotational conversion

The nuclei of the homonuclear isotopes are indistinguishable. Their wave functions are either anti-symmetrical or symmetrical under particle interchange depending on whether the nuclei are fermions or bosons, respectively.²⁶ The total wave function consists of the vibrational, rotational, and nuclear spin factors. The vibrational wave function depends only on the separation of the nuclei and is invariant under particle interchange. Hence, the parity of the molecular wave function depends only on the rotational and nuclear spin factors.

The spherical harmonics describe the molecular rotational wave function, given by $Y_J^m(\theta, \phi)$ for a molecule in rotational state J . Interchange of particles is equivalent to transforming $\theta \rightarrow -\theta$, which leaves $Y_J^m(\theta, \phi)$ unchanged for $J = \text{even}$ but takes $Y_J^m(-\theta, \phi) \rightarrow -Y_J^m(\theta, \phi)$ for $J = \text{odd}$. The nuclear spin composite wave function parity is determined for $I = 1/2$ nuclei spins according to the usual quantum mechanical angular momentum summation rules. The $|I = 1, m\rangle$ triplet and $|I = 0, 0\rangle$ singlet states are,²⁷

$$\begin{aligned} |1, 1\rangle &= |\uparrow\uparrow\rangle \\ |1, 0\rangle &= \frac{1}{\sqrt{2}}(|\uparrow\downarrow\rangle + |\downarrow\uparrow\rangle) \\ |1, -1\rangle &= |\downarrow\downarrow\rangle \\ |0, 0\rangle &= \frac{1}{\sqrt{2}}(|\uparrow\downarrow\rangle - |\downarrow\uparrow\rangle), \end{aligned} \tag{2.2}$$

where $|\uparrow\rangle$ is spin $m = +1/2$ and $|\downarrow\rangle$ is spin $m = -1/2$. The first three states are the same under interchange of the first and second spins, while the fourth changes sign and has negative parity. Hence, the nuclear wave function is symmetric under particle interchange for the $I = 1$ states and antisymmetric for the $I = 0$ state.

The total wave function must be antisymmetric for fermions, hence odd rotational levels are found only with spin $I = 1$ states, while even rotational levels are in the spin $I = 0$ state. These statistics apply to the T_2 molecules as well as H_2 , because the tritium nuclei are also $I = 1/2$. However, the D_2 nuclei are composed of a proton and neutron and are spin $I = 1$ bosons, necessitating a symmetric total wave function. The individual spins are added using the Clebsch-Gordon coefficients to yield states of total spin $I = 0, 1$, and 2 with wave functions $|I, m_i\rangle$,

$$\begin{aligned}
|0, 0\rangle &= \frac{1}{\sqrt{3}} (|m_1 = 1, m_2 = -1\rangle - |m_1 = 0, m_2 = 0\rangle + |m_1 = -1, m_2 = 1\rangle) \\
|1, 1\rangle &= \frac{1}{\sqrt{2}} (|m_1 = 1, m_2 = 0\rangle - |m_1 = 0, m_2 = 1\rangle) \\
|1, 0\rangle &= \frac{1}{\sqrt{2}} (|m_1 = 1, m_2 = -1\rangle - |m_1 = -1, m_2 = 1\rangle) \\
|1, -1\rangle &= \frac{1}{\sqrt{2}} (|m_1 = -1, m_2 = 0\rangle - |m_1 = 0, m_2 = -1\rangle) \\
&\dots
\end{aligned} \tag{2.3}$$

where the five $I = 2$ states have been omitted. The $I = 1$ triplet states are negative parity and the $I = 0$ and 2 states are positive under the interchange of m_1 and m_2 . The symmetry requirement on the total D_2 wave function is satisfied when $I = 1$, $J = \text{odd}$, or $I = 0, 2$ and $J = \text{even}$.

Molecules initially in even rotational states at high temperature populate the $J = 0$ level at low temperatures. Similarly, molecules that were initially in odd rotational states are found in the $J = 1$ level, even though it is a higher energy state than the $J = 0$. This meta-stable state persists until an external field causes a spin transition. The molecules reach equilibrium quickly at high temperatures and each m_I state is equally populated. The degeneracy of the even and odd I states gives the equilibrium, termed “normal”, ratio of 75% of the H_2 and 33% of the D_2 molecules in odd rotational states. This is the fraction of molecules in the $J = 1$ state immediately after cooling. Spin interactions with magnetic moments and electric quadrapole moments enable spin flips and conversion to the lower energy $J = 0$ states.

Figure 2.3 shows the $J = 1 \rightarrow 0$ self-conversion process for pairs of $J = 1$ molecules.

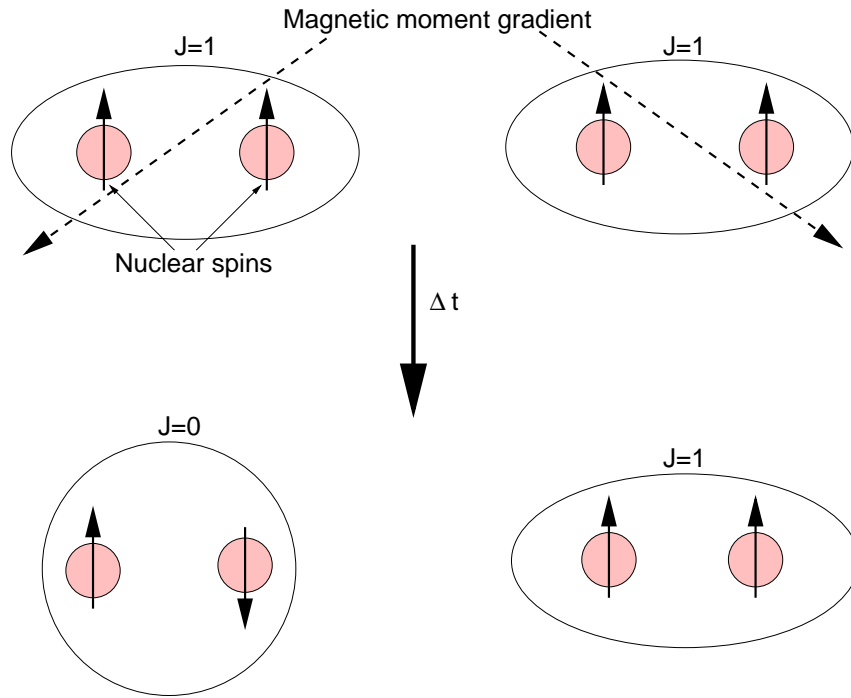


Figure 2.3: Neighboring $J=1$ molecules interact via their magnetic moments to convert nuclear spins. The nuclei within a molecule are subject to a different field because the field strength decreases with distance. After an interaction time Δt one nuclei spin is flipped and the rotational state drops into the $J = 0$ level.

The $J = 1$ molecules possess a magnetic moment which converts $J = 1 \rightarrow 0$ in neighboring molecules. The conversion rate depends on the concentration of $J = 1$ molecules, giving the second order rate equation $\frac{dn}{dt} = -kn^2$, for the number of molecules $n(t)$ in the $J = 1$ state. Additionally, D_2 $J = 0$, $I = 2$ molecules convert $J = 1$ states with approximately the same rate constant. The reaction appears as a first order process with the concentration of $J = 1$ molecules given by $c_1(t) = c_1(0) \exp(-kt)$. The measured self-conversion $1/e$ time is 140 hours for H_2 and 1900 hours for D_2 ⁷ and agrees well with the theory developed by Berlinsky and Hardy.²⁸

Any magnetic field interaction gradient causes $J = 1 \rightarrow 0$ conversions. The use of a material with a strong magnetic moment, such as paramagnetic oxides,⁷ as a catalyst is common. In D-T, the ions and atoms produced by the triton decay also increase the conversion rate.^{29,19,20} The large magnetic moments of the free atoms rapidly convert $J = 1$ molecules. Hence the $J = 1 \rightarrow 0$ conversion rate is much higher for tritiated than non-tritiated mixtures. The reaction is a first order rate process, since it depends only on the proximity of the atoms and the $J = 1$ molecules and the atom concentration is independent of time. D_2 molecules can also interact with an electric field gradient so ions and free electrons generated by the beta decay further speed up conversion.

Two time constants set the conversion rate of $J = 1$ molecules by atoms.^{29,19} The first is the interaction time required for $J = 1 \rightarrow 0$ conversion to take place. The second is the hopping rate of the atoms through the lattice. The $J = 1 \rightarrow 0$ conversion process is most efficiently when the two rates are equal. The atom spends just enough time near a $J = 1$ molecule to convert it before moving to another lattice site. The atoms remain in lattice sites longer than the interaction time at low temperatures where the diffusion rate is small. At higher temperatures, the atoms diffuse away from $J = 1$ molecules before

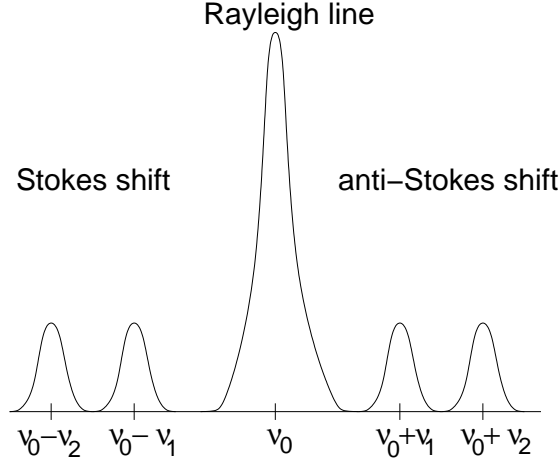


Figure 2.4: Emitted photon frequencies in a typical Raman scattering spectrum. The Rayleigh line is not shifted and has the same frequency ν_0 as the incident light. The Stokes shift is the photon loss of energy to the molecular states $\nu_1, \nu_2 \dots$ and the anti-Stokes shift is the photon energy gain from the molecules states.

conversion occurs.

Nuclear magnetic resonance measurements of the $J = 1$ T_2 and D_2 populations in D-T found the maximum conversion rate at 10 K. The NMR measurements observe the T_2 $J = 1$ population decay through the free induction decay and the D_2 through the nuclear spin relaxation time constant, dominated by the electric field quadrupole-quadrupole (EQQ) interaction.²⁰ As the $J = 1$ population decreases, the average distance between $J = 1$ molecules in the lattice is increased, reducing the EQQ interaction. The intensity of the Raman rotational $J = 0-2$ and $J = 1-3$ transitions is directly proportional to the number of molecules in the $J = 0$ and $J = 1$ states, respectively, and provides a confirmation of the EQQ model dependent NMR measurements.

2.3 Raman scattering

Inelastic light scattering, known as Raman scattering, is a shift in energy of the scattered light from the incident beam. Photon excitations or de-excitations of molecular vibra-

tional, rotational, or orientational states shift the energy of the scattered light. The transfer of energy from the photons to molecules is termed the Stokes shift and the molecule to photon energy transfer is the anti-Stokes shift (figure 2.4). The unshifted scattered light is Rayleigh scattering. In the low temperature systems of interest in this thesis, the upper molecular levels $J > 1$, $\nu > 0$, are not significantly populated and the anti-Stokes scattering is very weak.

Raman spectroscopy characterizes the molecular environment using the energy shifts in the molecular energy states. Raman scattering requires both a photon and either a roton or vibron to interact with the incident photon. Hence, Raman scattering is a second order process and is much weaker, by comparison, than Rayleigh scattering which requires only a single photon interaction with the incoming photon. In the language of perturbation theory, Rayleigh scattering is the first order perturbation expansion, while Raman scattering is second order.

This review of Raman scattering is similar to that presented by Ferraro and Nakamoto.³⁰ Although this example is specific to the vibrational molecular motion, the basic concepts also apply to rotations. The photon interaction with the molecule is treated as a perturbation of the simple harmonic oscillator (SHO). The unperturbed states are eigenstates of the SHO. The energy of state $|n\rangle$ is $E_n = \hbar\omega(n + 1/2)$. The incoming photon polarizes the molecule and the interaction Hamiltonian is

$$H = -\boldsymbol{\mu} \cdot \mathbf{E}. \quad (2.4)$$

The electric field is assumed to be weak so that the induced polarization is linear in E , $\mu = \epsilon\alpha E$, where α is the molecular polarizability. Polarizability is a function of the nuclei

separation, which can be expanded in a Taylor series of the vibrational coordinate q as

$$\alpha = \alpha_0 + \left(\frac{d\alpha}{dq} \right)_0 q, \quad (2.5)$$

where α_0 is the polarizability at the equilibrium separation. The coordinate q is expressed as an operator in the SHO formalism,

$$q = \sqrt{\frac{\hbar}{2m\omega}} (a^\dagger + a), \quad (2.6)$$

where a^\dagger and a are the harmonic oscillator creation and annihilation operators. Equations 2.6 and 2.5 are combined and substituted into 2.4 to give

$$H = \epsilon \left[\alpha_0 + \frac{d\alpha}{dq} \sqrt{\frac{\hbar}{2m\omega}} (a^\dagger + a) \right] E^2. \quad (2.7)$$

The first term in brackets does not mix vibrational states and is the source of Rayleigh scattering. The creation and annihilation operators couple states $|n\rangle$ and $|n \pm 1\rangle$. The creation operator increases the molecular vibrational energy and is the source of the Stokes shift, while the annihilation operator gives the anti-Stokes shift. The scattered photon energy is $E_s = E_i \mp \hbar\omega$, conserving energy.

2.3.1 Rotational Raman spectrum

The hydrogen vibrational and rotational excitations are useful in understanding molecular interactions. Vibrational energy changes with solid density and $J = 1$ concentration.^{23,31,22,32} Also, the rotational states are broadened by the crystal field and interactions with $J = 1$ quadrupole moments.^{21,14,23}

Information pertaining to the $J = 1$ concentration and the crystal lattice structure are contained in the rotational Raman spectrum. Using the independent polarizability approximation, the total scattering intensity for $\Delta J = 2$ is proportional to the number of

molecules in the initial rotational state J (N_J) by^{14,33}

$$I_J \propto N_J \frac{(J+1)(J+2)}{(2J+2)(2J+1)} \omega^3 |\langle \psi | \alpha_J | \psi \rangle|^2. \quad (2.8)$$

The polarizability matrix elements $\langle \psi | \alpha_{J=0} | \psi \rangle$ and $\langle \psi | \alpha_{J=1} | \psi \rangle$ differ by less than 1% for D_2 molecules and 2% between the T_2 and D_2 isotopes.^{34,35} Further, there is no phonon interaction because the rotational transition energies are larger than the Debye temperature (table 2.1). Hence, the ratio of the scattering intensities $I(J=1-3)/I(J=0-2)$ depends on the $J=1$ and $J=0$ ratio and is related to the number of molecules in the $J=1$ and $J=0$ states by

$$\frac{N(J=1)}{N(J=0)} = \frac{5}{3} \frac{I(J=1)}{I(J=0)}. \quad (2.9)$$

The rotational Raman spectrum provides a convenient measurement of the D-T isotope ratio in filled targets.^{33,36}

The $J=0-2$ spectrum indicates the crystal structure. The $J=2$ state has the five $m_J = 0, \pm 1, \pm 2$ sub-levels. In the solid composed solely of $J=0$ molecules, the crystal symmetry splits the degeneracy of the m_J levels. The hcp lattice structure gives rise to a triplet state, while the fcc lattice splits the m_J states into a doublet.^{21,23,11} The D_2 hcp $J=0-2$ transitions are²¹ 176.8 cm^{-1} , 179.4 cm^{-1} , and 182.0 cm^{-1} for the $m_J = \pm 1, \pm 2$, and 0 states, respectively.

The addition of $J=1$ molecules to the solid broadens the $J=0-2$ transition. Van Kranendonk calculates the broadening of the $J=2$ rotational states to be 20 cm^{-1} due to the anisotropic forces.²³ The hcp triplet structure becomes a continuous band as the $J=1$ population is increased.

The steady state $J=1$ population due to both thermal excitation as well as the radiation damage is less than 2% for all temperatures studied here.^{7,20} This is based on

both the thermal population as well as that produced by the triton decay and subsequent creation of free ions.

2.3.2 Vibrational spectrum

The vibrational energy state is shifted by intermolecular interactions and thus depends on the $J = 1$ concentration and the solid density.^{22,23,31,32} The $J = 1$ molecules are stretched slightly due to the centrifugal force and vibrate at a lower frequency than the $J = 0$ molecules. Transitions between the $\nu = 0$ and 1 states for $J = 0$ and 1, are denoted by $Q_1(0)$ and $Q_1(1)$. The values measured in previous works are listed in table 2.2 for homonuclear hydrogens. As expected from the harmonic oscillator model, the vibrational frequencies vary as $1/\sqrt{m}$ between isotopes.

Mode	H ₂ (cm ⁻¹)	D ₂ (cm ⁻¹)	T ₂ (cm ⁻¹)
Q ₁ (0) J = 0 solid	4149.8	2984.4	
Q ₁ (1) J = 0 solid	4146.3		
Q ₁ (0) normal solid	4151.8	2985.46	
Q ₁ (1) normal solid	4143.4	2982.48	
Q ₁ (0) J = 1 hcp solid	4152.4	2986.6	
Q ₁ (1) J = 1 hcp solid	4143.1	2981.5	
Q ₁ (0) vapor	4161.1	2993.5	2464.3
Q ₁ (1) vapor	4155.2	2991.4	

Table 2.2: Vibrational frequencies of the Raman H₂ and D₂ lines measured by Bhatnagar *et al.*²¹, Soots *et al.*,²² and Prior and Allin.^{37,38} The value for T₂ is from Edwards *et al.*³⁹

The $Q_1(0)$ and $Q_1(1)$ separation is easily resolved for both isotopes with the spectrometer used in this work. However, it is not easily possible to use the intensity ratio to measure the $J = 1$ concentration. The small energy difference leads to a coupling between the $J = 1$ and $J = 0$ molecules and an enhancement of the $Q_1(1)$ scattering cross section.^{24,31} The enhancement depends on $J = 1$ concentration and varies from 2 - 4 in H₂ and about 5 - 50 in D₂.²³ The expected T₂ enhancement is larger than D₂ because

the $Q_1(0)$ and $Q_1(1)$ energy difference decrease with increasing mass, evident in table 2.2. However, it will be shown that the mixture of isotopes further alters the relative scattering cross section.

The vibrational energy depends on the solid density. The coupling between molecules is larger when their separation is smaller and the increased coupling gives rise to an energy shift. The frequency shift is given as^{23,31}

$$\Delta\nu = \Delta\nu_0 - 6\epsilon \left(\frac{V_0}{V} \right)^2 c_J, \quad (2.10)$$

where c_J is the concentration of $J = 0$ or $J = 1$ molecules in the solid, V is the solid molar volume, and V_0 is the solid molar volume at zero pressure. $\Delta\nu_0$ is the single molecule coupling and is -7.0 cm^{-1} in $J = 0 \text{ D}_2$.²³ As the $J = 1$ population decays away the $Q_1(0)$ line shifts to lower energy, while the $Q_1(1)$ line shifts to higher energy.

2.4 Experimental results

2.4.1 Experimental setup

The D-T sample was a $800 \text{ }\mu\text{m}$ diameter glass shell filled with 25 atm of D-T gas at room temperature. The shell was originally filled with the 25-50-25 mixture of D_2 -DT- T_2 . Analysis of the Raman spectrum gave a ratio of 30-52-18 at the time of the experiments. The shell was glued to a sapphire window mounted in the cell shown in figure 2.5. Crushed indium provided the thermal connection between the sapphire window and cell. The cell was attached to the copper cold tip of a liquid helium cooled flow cryostat. Germanium resistance thermometers were used to monitor the cell temperature and provide feedback for a Lakeshore temperature controller. Temperature variations were $\pm 10 \text{ mK}$ over minutes, with slow drifts up to $\pm 200 \text{ mK}$ over the course of a day. The cell could be cooled

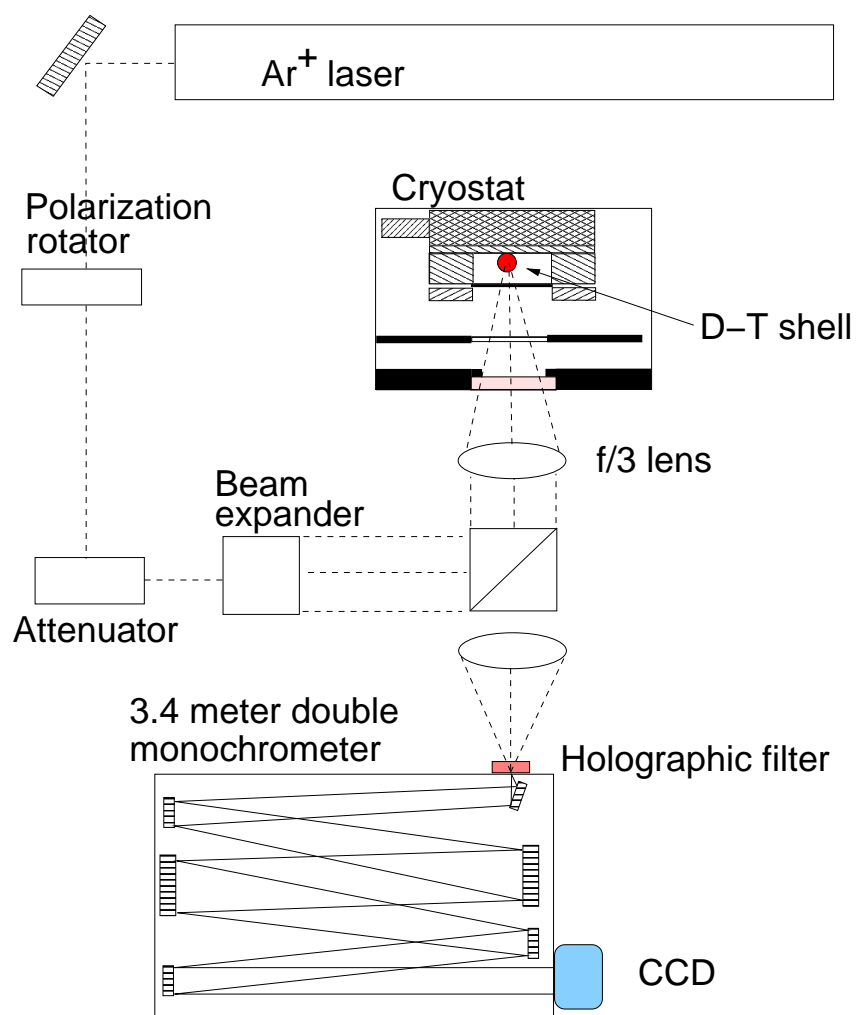


Figure 2.5: Layout of the Raman experiment.

down to 5 K.

For performing the Raman spectroscopic measurements, a Spectra Physics 171 argon ion laser was operated at 488 nm. The beam was expanded to 23 mm with a Galilean beam expander. The expanded beam was focused onto the sample with a Mitutoyo long working distance microscope objective. The backscattered light was collected by the Mitutoyo and focused onto the spectrometer by a doublet matching the 7.8 f/# of the spectrometer. A Kaiser Optical HSNF 488-1.0 holographic notch filter reduced the intensity of the Rayleigh scattered light, which would otherwise saturate the signal.

A Spex 1403 double monochromator with a pair of 1800 lines/mm gratings blazed for 500 nm was used to disperse the Raman signal onto a Princeton Instruments liquid nitrogen cooled CCD camera containing a CCD chip with 1152 x 298 pixels. The pure D₂ narrow line width gas phase rotational and vibrational lines were used as the primary spectrometer calibration. D₂ was used instead of the D-T shell because the pure component line positions are well known. The D₂ was added to the same cell, around the shell, the calibration included all collections optical elements as well as the spectrometer and CCD. The grating dispersion is wavelength dependent and was found to be 4.8 pixels per wavenumber for the D₂ rotational lines and 6.6 pixels per wavenumber for the D₂ vibrational lines. The large frequency separation between the J = 0-2 and J = 1-3 transitions required rotating the spectrometer grating between each set of lines. The ability to return the grating to the same position each time limited the ability to measure line shifts, especially for the sharp vibrational lines. However, the repeatability was typically better than the resolution of the spectrometer-camera system, 0.2 cm⁻¹. By starting below the desired wavenumber and rotating the spectrometer grating toward higher wavenumbers, backlash in the grating drive was minimized. The line positions varied less than ± 1 pixel

typically when operated in this manner.

2.4.2 J=1→0 conversion rate

Each run started with the D-T sample at room temperature for at least 8 hours before cooling. This was long enough for the D-T rotational population to equilibrate. The cryostat and target shell were quickly cooled to the desired temperature and likely resulted in polycrystalline solid samples. The measurements were started as soon as possible after cooling. Typical cooling time was less than 30 minutes from room temperature to the desired temperature.

The measured D-T rotational Raman spectrum is shown in figures 2.6 – 2.8 for a sample at 6 K. The spectrometer input slit width was 40 μm , or 0.4 cm^{-1} spectral bandpass for each spectra. The slit width was selected to provide as much resolution as possible in a reasonable collection time. Each spectra is the sum of three - 150 second long exposures. To reduce laser heating of the D-T and incorrect temperature dependence the laser was blocked between measurements.

The figures show the features typical of all runs. The T_2 J = 1 population decays away quickly with time and the J = 0-2 line is split into a triplet at low J = 1 concentration. The D_2 J = 1 population decays slower than the T_2 and the asymmetric J = 0-2 line shape remains broad throughout the run. The line widths for each species is in good agreement with Van Kranendonk's theory and previous experimental measurements.^{21,23} The line positions of the D-T spectrum agree with the values listed in table 2.1. After a day nearly all molecules are in the J = 0 state and the J = 1 Raman signals are below the noise level, about 4%, for both species.

The rotational populations were calculated from the ratio of the integrated line shape

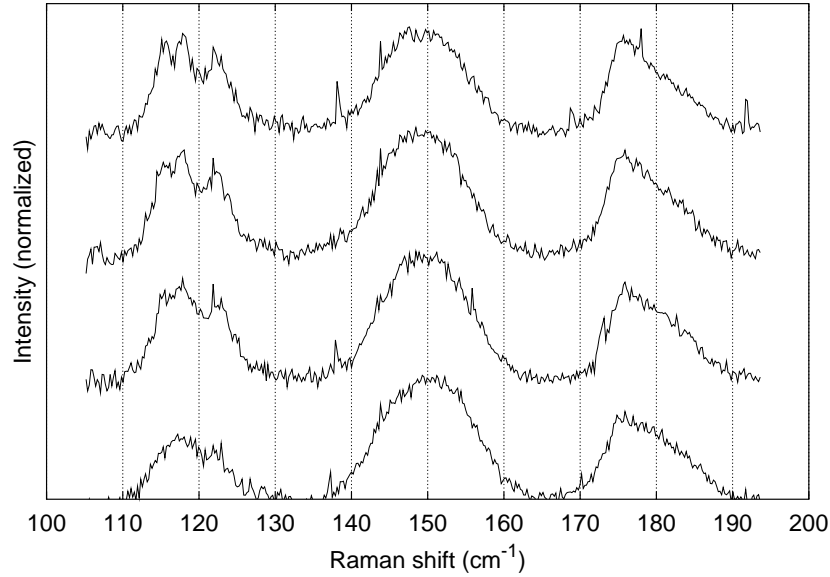


Figure 2.6: The $J=0-2$ transitions in D-T for each isotope as the $J=1$ population decays away. The transitions correspond to (from left to right) T_2 , DT, and D_2 molecules. The T_2 line shape is a triplet at the latest times, while the D_2 retains the asymmetric shape. The time since cooling from 77 K to 6.0 K is (bottom to top) 0.4 hours, 3.0 hours, 6.1 hours, and 13.2 hours.

intensity of each species. The D_2 and T_2 population are shown as the sample ages at 8.1 K in figure 2.9. The D_2 $1/e$ time is 5.2 hours compared to 1.1 hours for T_2 . Figures 2.10 and 2.11 shows the increased decay time at higher temperatures for T_2 and D_2 . The T_2 $J = 1$ population decreases very close to exponentially in each case and indicates the conversion is a first order process. This agrees with the model that conversion is caused by free atoms. The measured decay times for both D_2 and T_2 are shown in figure 2.12 and listed in table 2.3 for all runs. The values measured in the NMR measurements are shown as the lines in figure 2.12 and are listed in table 2.4. The measured values in this work do not change significantly until 10 K. For T_2 a slight minimum occurs at near 10 K, and the decay time increases significantly above 11 K. The D_2 time constant also increase rapidly above 10.2 K. The average ratio of D_2/T_2 time constants is 3.5 for measurements below 10 K, agreeing very well with the ratio of magnetic moments. The Raman measured

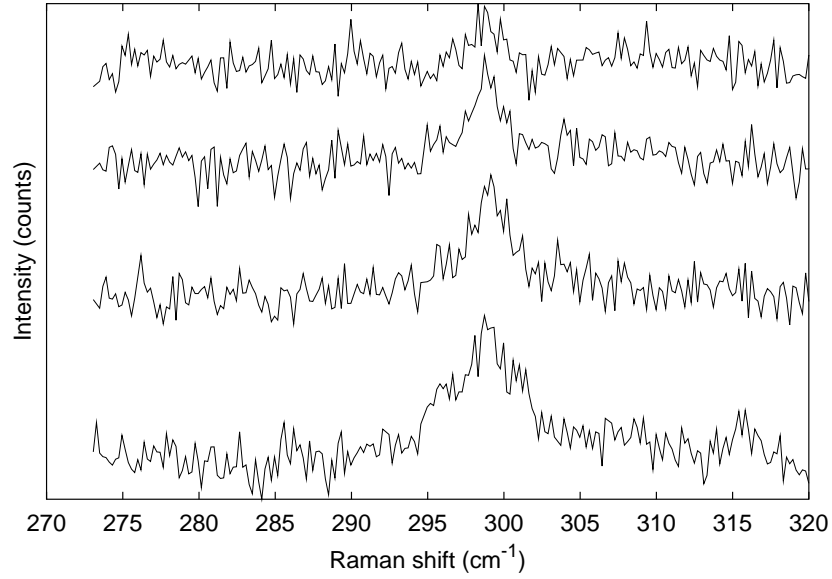


Figure 2.7: The D_2 $J=1-3$ transition vs time. The time since cooling to 6.0 K is (bottom to top) 0.53 hours, 3.1 hours, 6.3 hours, and 13.3 hours.

values for both T_2 and D_2 are larger than the NMR measurements, listed in table 2.4 by a factor of 2-4 above 8 K, but are comparable below 8 K.

2.4.3 Rotational broadening

Both the T_2 and the D_2 $J = 0-2$ degeneracy were expected to be split at low $J = 1$ concentration into the m_J sub-levels. However, the hcp triplet was observed only for T_2 even after 77 hours at 10.5 K, as shown in figure 2.13. The pure D_2 spectrum is shown in figure 2.14 with less than 1% $J=1$ for comparison. The D_2 triplet structure is easily resolved, and the peaks are listed in table 2.5. The values for pure D_2 agree with the measurements by Bhatnagar *et al.*²¹ for 20% $J = 1$. However, in contrast to the pure component H_2 and D_2 m_J splittings,^{21,23} the separation between peaks in T_2 is not symmetric.

In order to determine if the observed rotational structure is due to radiation damage or is a property of the mixture, the non-tritiated H_2 , HD and D_2 isotopes were mixed

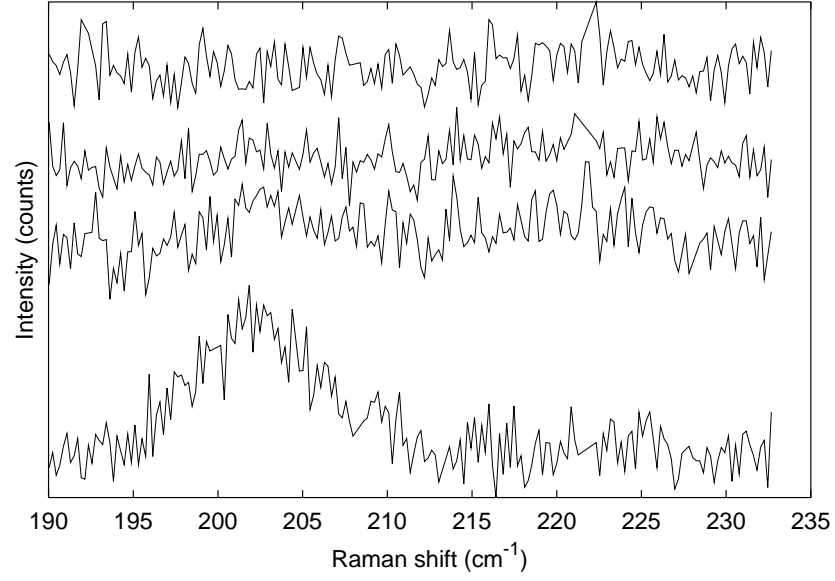


Figure 2.8: The T_2 $J=1-3$ transition vs time. The time since cooling to 6.0 K is (bottom to top) 0.25 hours, 2.8 hours, 5.9 hours, and 13.0 hours.

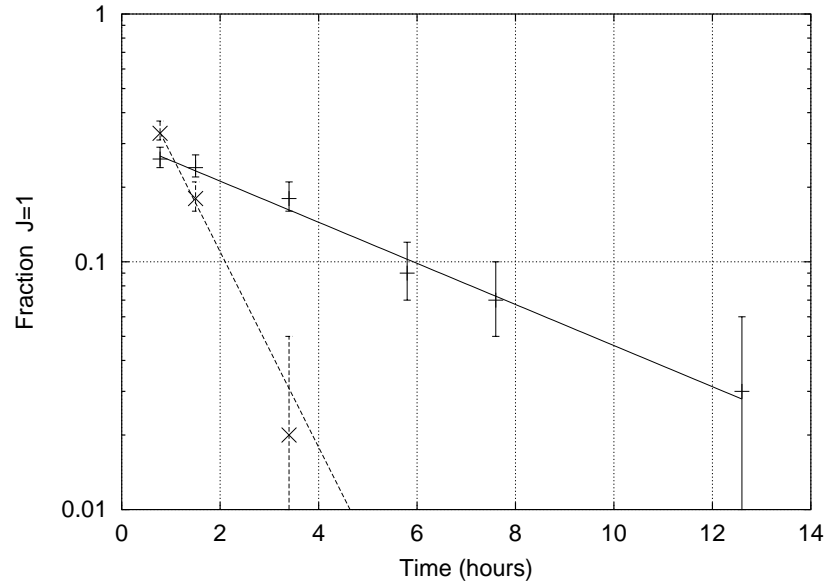


Figure 2.9: The measured T_2 (\times) and D_2 ($+$) $J=1$ concentrations vs time at 8.1 K. Both isotopes decay exponentially. The straight lines are least squares fits to the data.

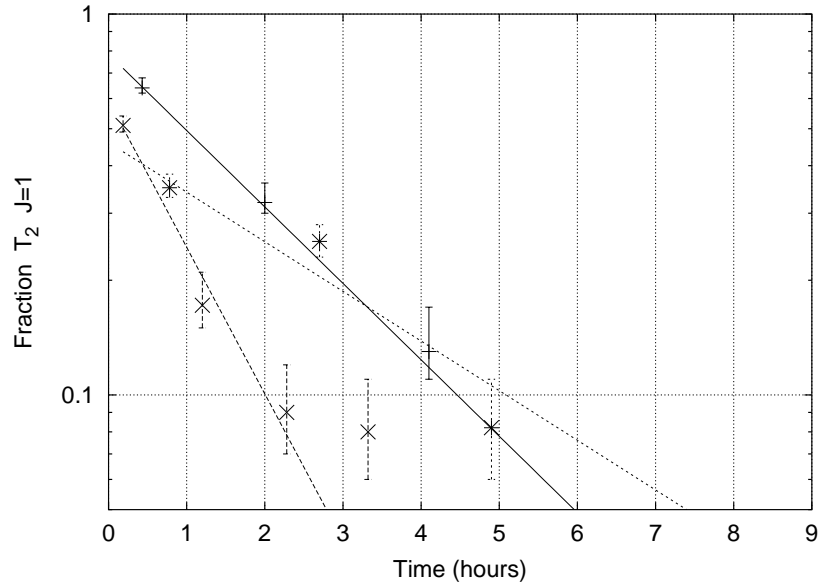


Figure 2.10: The measured T_2 $J=1$ fraction as a function of time after cooling. The straight lines are least squares fits to the data. The temperatures are 7.2 K (+, solid line), 10.2 K (\times , long dash), and 11.3 K (*, short dash).

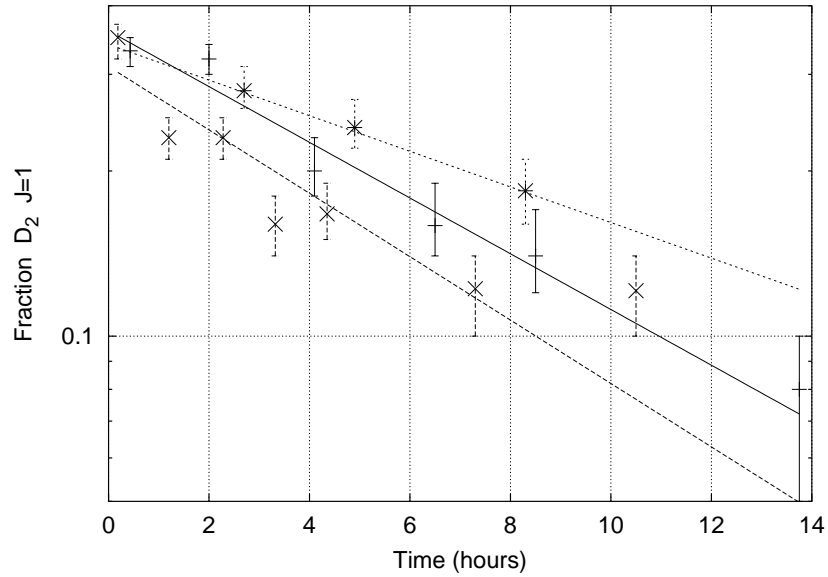


Figure 2.11: The measured D_2 $J=1$ fraction as a function of time after cooling. The straight lines are least squares fits to the data. The temperatures are 7.2 K (+, solid line), 10.2 K (\times , long dash), and 11.3 K (*, short dash).

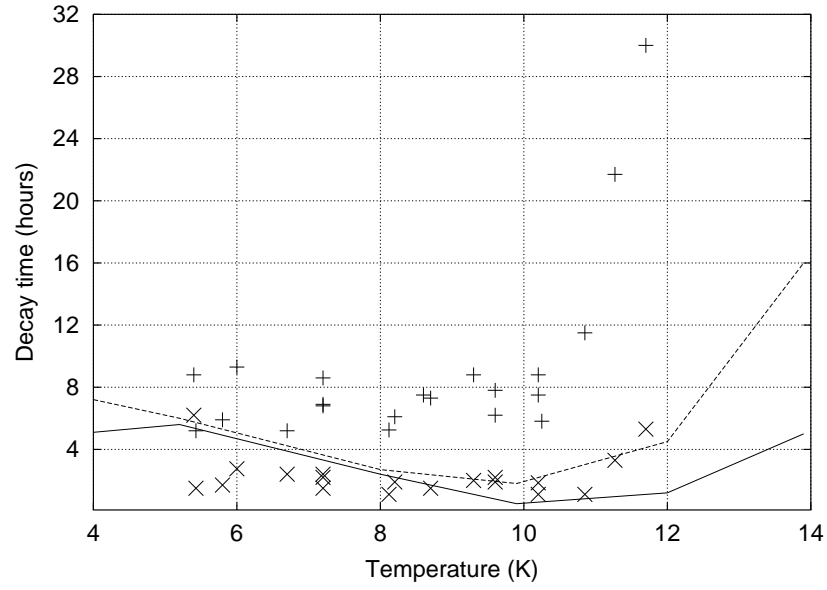


Figure 2.12: The T_2 (\times) and D_2 (+) measured decay times as a function of temperature. The solid line is the measured T_2 and the dashed line is the measured D_2 decay times from the NMR experiments.²⁰

Temp. (K)	$\tau(T_2)$ (hours)	$\tau(D_2)$ (hours)	$\tau(D_2)/\tau(T_2)$
5.4	6.1	9.1	1.5
5.4	1.5	5.3	3.5
5.8	1.7	5.9	3.5
6.0	2.8	9.1	3.2
6.7	2.4	5.3	2.2
7.2	2.2	8.3	3.8
7.2	2.4	6.8	2.8
7.2	1.5	6.9	4.6
8.1	1.1	5.2	4.7
8.2	1.9	6.1	3.2
8.6		7.5	
8.7	1.5	7.3	4.9
9.3	2.0	8.8	4.4
9.6	2.2	6.2	2.8
9.6	1.9	7.8	4.1
10.2	1.1	7.6	6.9
10.2	1.8	8.8	4.9
10.2		5.8	
10.8	1.1	15.5	14
11.3	3.3	22	6.6
11.7	5.3	30	5.7

Table 2.3: Measured $1/e$ times for T_2 and D_2 $J = 1 \rightarrow 0$ in this experiment.

Temp. (K)	$\tau(T_2)$ (hours)	$\tau(D_2)$ (hours)
5.2	5.6	6.0
8.0	2.4	2.7
9.9	0.5	1.8
12.0	1.2	4.5
13.9	5.0	16

Table 2.4: Measured 1/e times for T_2 and D_2 $J = 1 \rightarrow 0$ from the NMR experiment.²⁰

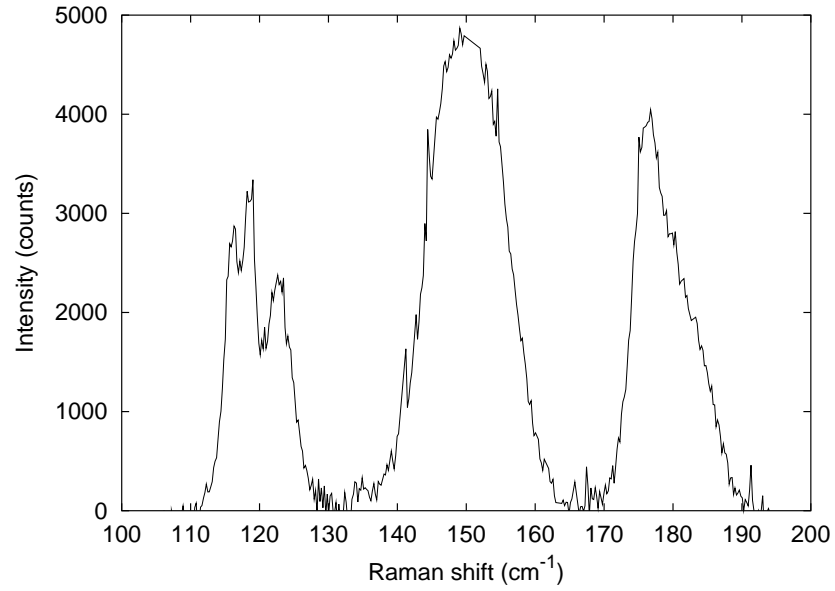


Figure 2.13: The D-T $J=0-2$ spectrum 77 hours at 10 K. The transitions are T_2 at 120 cm^{-1} , DT at 150 cm^{-1} , and D_2 at 179 cm^{-1} . Nearly all molecules are in the $J = 0$ state, but the D_2 rotational line remain broadened.

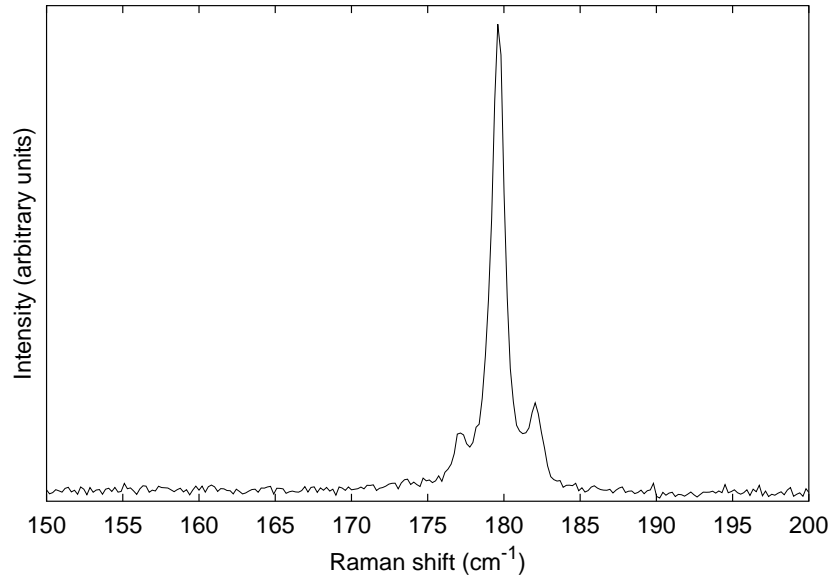


Figure 2.14: The pure $J=0$, D_2 $J = 0-2$ rotational transition. The line is much narrower and the triplet is well defined compared to D_2 in D-T.

and the rotational spectrum measured. Both D_2 and H_2 were catalyzed and converted to $J = 0$ before being mixed. The D_2 and H_2 had concentrations of $< 1\%$ and 4% $J = 1$, respectively, as measured from the rotational line intensities. The gases were mixed then condensed into the solid phase. The mixed solid was much larger than the D-T shell, hence the scattered intensity was larger and the minimum spectrometer slit width of $20 \mu\text{m}$ was used to obtain the minimum spectrometer bandpass of 0.2 cm^{-1} .

Figures 2.15 and 2.16 show the change in the D_2 and H_2 $J = 0-2$ rotational lines as H_2 is added to D_2 . The D_2 line shape is broadened upon adding only 13% H_2 to the sample, but the m_J splitting is still identifiable. Both H_2 and D_2 $J = 0-2$ transitions are broadened and the triplet structures are lost as the H_2 concentration is increased.

Figures 2.17 and 2.18 show the D_2 and H_2 $J = 0-2$ lines as HD to the mixture. The D_2 lines remain broader than the pure component, but the triplet structure is visible at 45-35-20 ratio of H_2 -HD- D_2 . Further, as shown in table 2.5, the separation between m_J levels

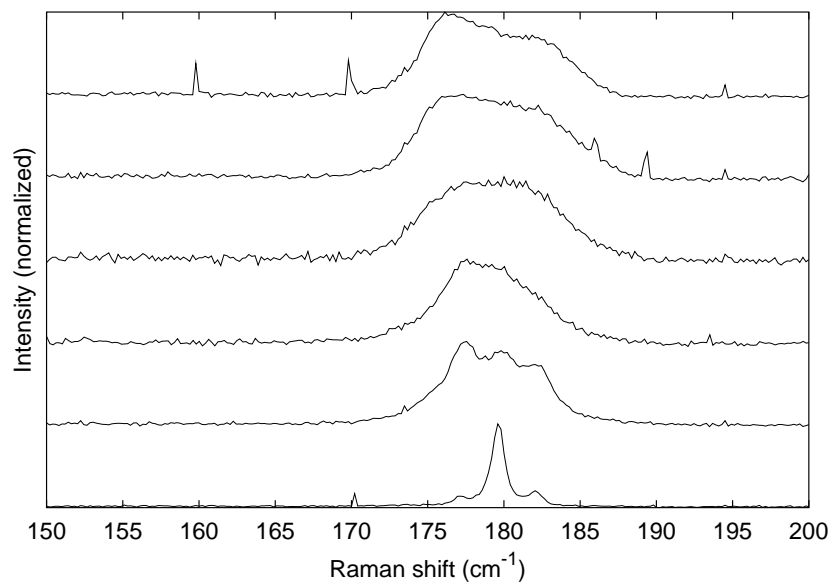


Figure 2.15: The D_2 $J = 0-2$ transition is broadened and the triplet structure is removed as H_2 is added. The amount of H_2 in the sample is (bottom to top) 0%, 13%, 24%, 33%, 47%, and 61%.

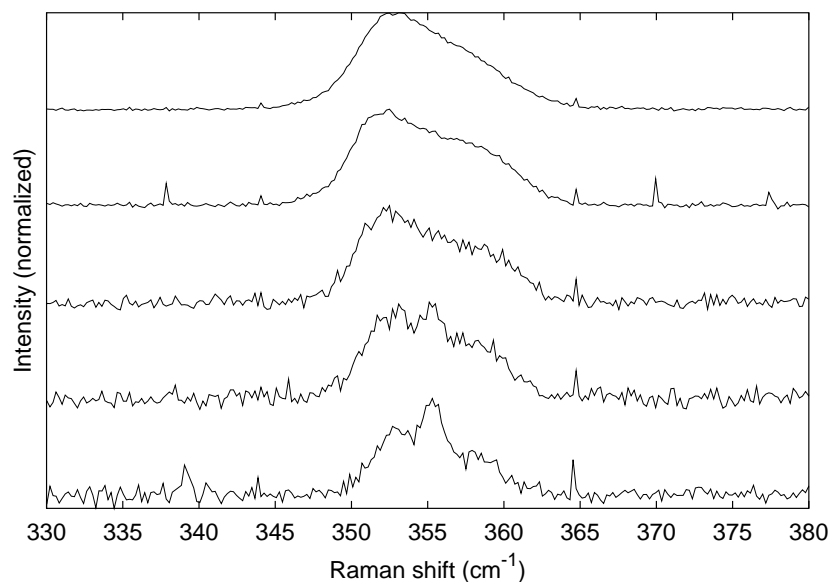


Figure 2.16: The H_2 rotational line as H_2 is added to D_2 . The triplet is initially broadened due to the residual $J=1$ component. The amount of H_2 in the sample is (bottom to top) 13%, 24%, 33%, 47% and 61%.

Isotope	Position (cm^{-1})	Splitting (cm^{-1})
D_2 in D_2	177.1	
	179.6	2.5
	182.1	2.5
D_2 in H-D mixture	176.5	
	178.8	2.3
	181.8	3.0
D_2 in D-T Center of mass Peak	178.8	
	176.8	
T_2 in D-T	116.3	
	118.8	2.5
	122.7	3.9
D_2 in D_2 (Bhatnagar <i>et al.</i>) ²¹	176.8	
	179.4	2.6
	182.0	2.6

Table 2.5: Solid phase $J = 0-2$ rotational line positions. The first four are values measured in this work, while the last provides reference values.

is no longer equal for D_2 in the mixture. The H_2 lines remain broad with no evidence of the triplet for any mixture ratio. It has an asymmetric line shape similar to that observed on D_2 in the D-T mixture. The rotational line shape observed in D-T is a result of the isotope mixture and is not due to radiation damage. The preferential broadening of the lighter isotopes in mixtures requires further investigation and its reason is not known at this time. Curiously, the line shape is similar to figure 18 of Hardy *et al.* for D_2 and H_2 under very different conditions.¹⁴ In their experiment, the $J = 0$ molecules were an impurity in the 97.8% $J = 1$ D_2 and the 96.7% $J = 1$ H_2 at 4 K. The D_2 is in the fcc state and the $J = 1$ molecules are claimed to be rotationally disordered. They attribute the asymmetric shape to the short range order of the $J = 1$ molecules.

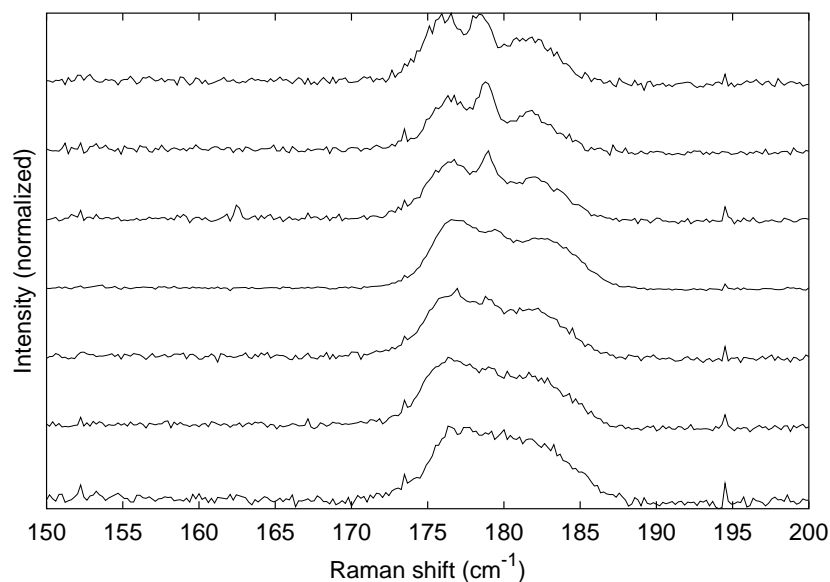


Figure 2.17: The rotational lineshape for D_2 as HD is added to the H_2 and D_2 mixture. The structure remains broad, but the triplet structure re-emerges. The percent of H_2 -HD- D_2 is (bottom to top) 67-0-33, 57-10-33, 52-18-30, 46-27-27, 45-35-20, 47-38-15, and 30-51-19.

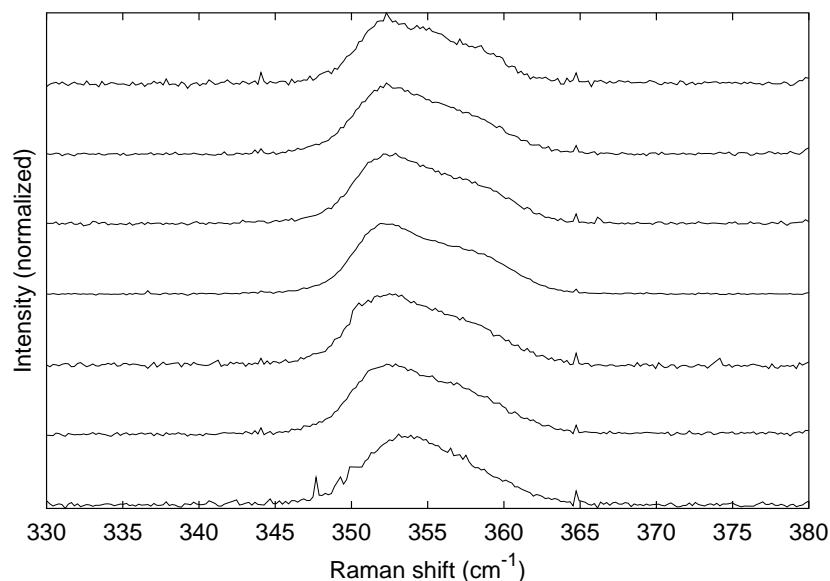


Figure 2.18: The H_2 rotational line shape as HD is added to the H_2 and D_2 mixture. The structure remains broad and has an asymmetrical shape similar to that observed for D_2 in D-T. The percent of H_2 -HD- D_2 is (bottom to top) 67-0-33, 57-10-33, 52-18-30, 46-27-27, 45-35-20, 47-38-15, and 30-51-19.

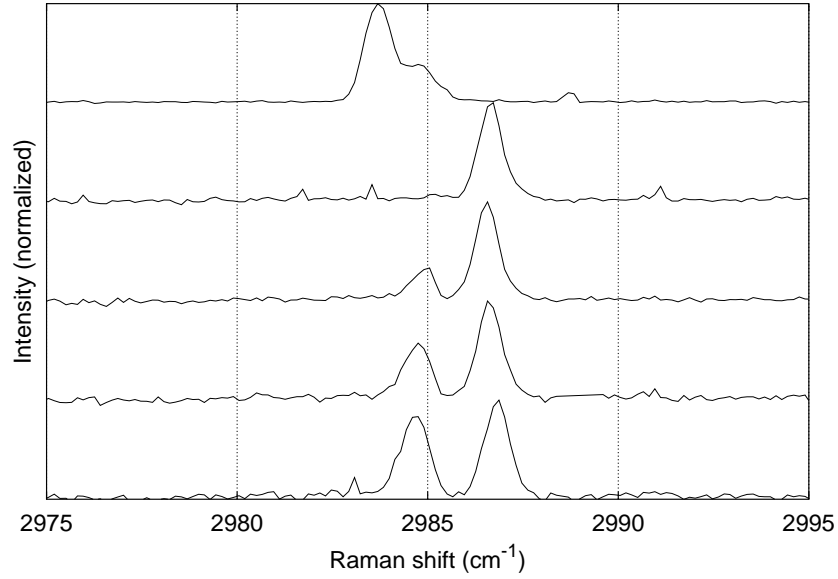


Figure 2.19: The D_2 in D-T vibrational lines as the $J=1$ population decays. The percent of D_2 in the $J=1$ state is (bottom to top) 30%, 19%, 10%, <2%. The top spectrum is pure D_2 with 5% $J=1$. The sample temperature was 8.0 K.

2.4.4 Vibrational transitions

The $Q_1(0)$ and $Q_1(1)$ lines of T_2 and D_2 in D-T were measured as the $J = 1$ population decayed away. Figures 2.19 and 2.20 show the vibrational lines for D_2 and T_2 respectively, where the $Q_1(0)$ line is the higher energy line in each case, and the pure component D_2 with 5% $J = 1$ is included for comparison with the mixture. Table 2.6 lists the measured $Q_1(0)$ and $Q_1(1)$ frequencies. The $J = 1$ concentration was not measured directly because the large separation between the rotational and vibrational lines prevented simultaneous measurement of the rotational lines. Instead, the $J = 1$ concentration was calculated from the previously measured time constants. The D_2 $Q_1(0)$ and $Q_1(1)$ lines are both shifted to higher energy by 1 - 2 cm^{-1} in the D-T mixture than in pure D_2 . The enhanced $Q_1(1)$ line intensity evident in the pure D_2 sample, is significantly reduced for both D_2 and T_2 in D-T.

There is a small shift in the vibrational energy as the $J = 1$ decays away. The measured

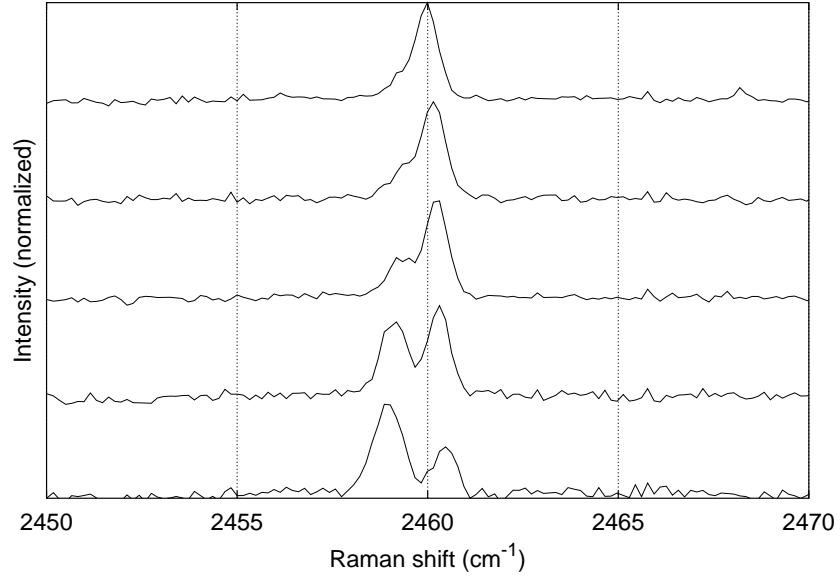


Figure 2.20: The T_2 vibrational lines as the $J=1$ population decays. The percent T_2 in the $J=1$ state is (bottom to top) 50%, 23%, 8%, 3%, <1%. The sample temperature was 8.0 K.

Species	Temp. (K)	$Q_1(0)$ (cm^{-1})	$Q_1(1)$ (cm^{-1})	$Q_1(0)-Q_1(1)$ (cm^{-1})
D_2 in D_2 vapor		2993.5		
D_2 in 5% $J = 1$ D_2 solid	8	2984.8	2983.7	1.1
D_2 in < 1% $J = 1$ D_2 solid	12.7	2984.8	2984.1	0.7
D_2 in 30% $J = 1$ D-T solid	8	2986.9	2984.7	2.2
D_2 in $J = 0$ D-T solid	8	2986.7	2985.2	1.5
D_2 in $J = 0$ 13% H_2	9	2984.9	2984.3	0.6
D_2 in $J = 0$ 33% H_2	8	2985.4	2984.8	0.6
D_2 in $J = 0$ 61% H_2	9.5	2986.6	2985.4	1.2
T_2 in 50% $J = 1$ D-T solid	8	2460.5	2458.9	1.6
T_2 in $J = 0$ D-T solid	8	2460.0	2459.2	0.8

Table 2.6: Measured $Q_1(0)$ and $Q_1(1)$ line positions for D_2 and T_2 .

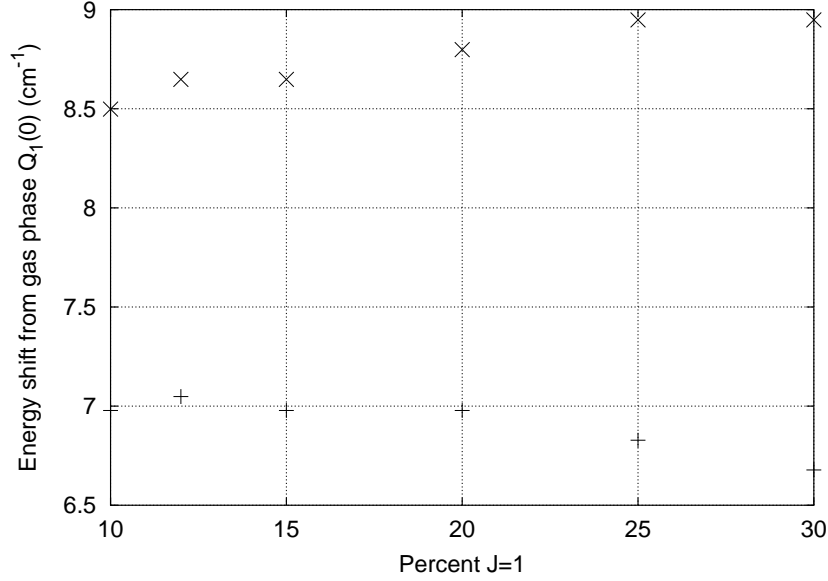


Figure 2.21: The shift in energy relative to the gas phase line of the D₂ Q₁(1) (×) and Q₁(0) (+) lines in D-T. The sample temperature was 8.0 K

energy shift from the gas phase Q₁(0) line is shown in figures 2.21 and 2.22. The Q₁(0) and Q₁(1) separation decreases as the J = 1 population decays, in qualitative agreement with equation 2.10. The relative shift is 0.9 cm⁻¹ in T₂ and 0.75 cm⁻¹ in D₂, and is larger than expected, as will be explained below.

The H₂-D₂ mixture serves as a reference for the D-T mixture as in the rotational case. The D₂ vibrational lines are shown in figure 2.24 as H₂ was added. As in D-T, the Q₁(1) intensity decreases compared to the Q₁(0) line. The enhanced Q₁(1) scattering cross section is lost in the H₂-D₂, as was observed in the D-T mixture. The decrease in the number of J = 0 molecules that can couple to the J = 1 molecule of the same isotope reduces the line strength. This is not simply because the J = 1 concentration has decreased, but rather is due to the inability of the J = 1 D₂ molecules to couple to the H₂ molecules because of the large energy difference.

Both the Q₁(1) and Q₁(0) lines are shifted to higher energy as H₂ is added. The shifts

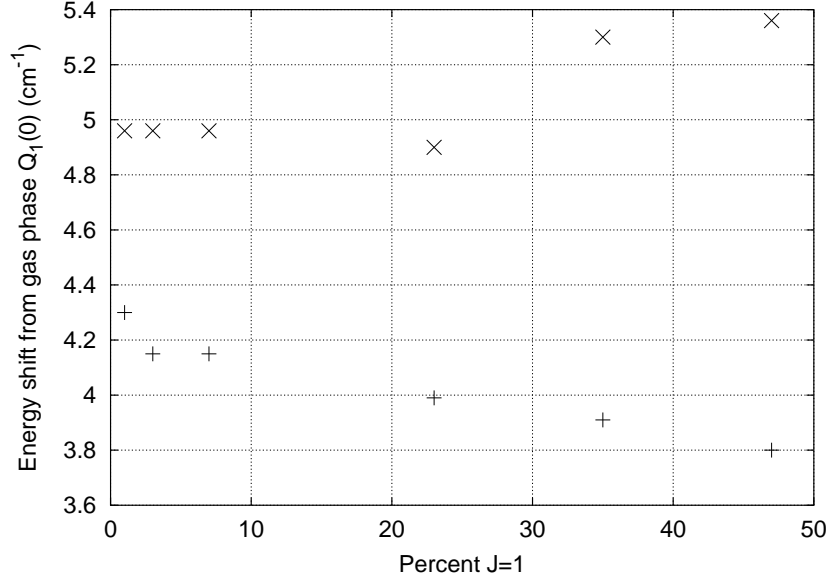


Figure 2.22: The shift in energy relative to the gas phase line of the T₂ Q₁(1) (×) and Q₁(0) (+) lines in D-T. The sample temperature was 8.0 K.

relative to the gas phase Q₁(0) line are shown in figure 2.24. The volume change upon mixing the isotopes was expected to be given by

$$V = c_{H_2} V_{H_2} + c_{D_2} V_{D_2}, \quad (2.11)$$

where c_i is the concentration of the i th species with molar volume V_i and the isotopes are assumed to completely mix. Then $(V_0/V)^2 = 0.86$ with V for a 50-50 mix of H₂ and D₂ and V_0 for pure D₂ using Souers'⁷ values for the 9 K solid molar volumes. The value of 6ϵ in equation 2.10 is 2.2 cm⁻¹, obtained from the D₂ pure component Q₁(0) shift with the J = 1 concentration varied as measured by Prior and Allin.³⁷ The expected Q₁(0) shift in a 50-50 H₂-D₂ mixture is only $(1 - 0.86) \cdot 2.2 \text{ cm}^{-1} = 0.31 \text{ cm}^{-1}$ from the pure D₂ solid. This clearly disagrees with the measured shift of 1.2 cm⁻¹ for a 50-50 mixture.

The correct behavior is obtained when c_J is taken as the concentration of J molecules for one particular isotope in the total mixture, not simply the concentration for each isotope. The coupling that leads to this shift is due to J = 0 neighboring molecules. Their

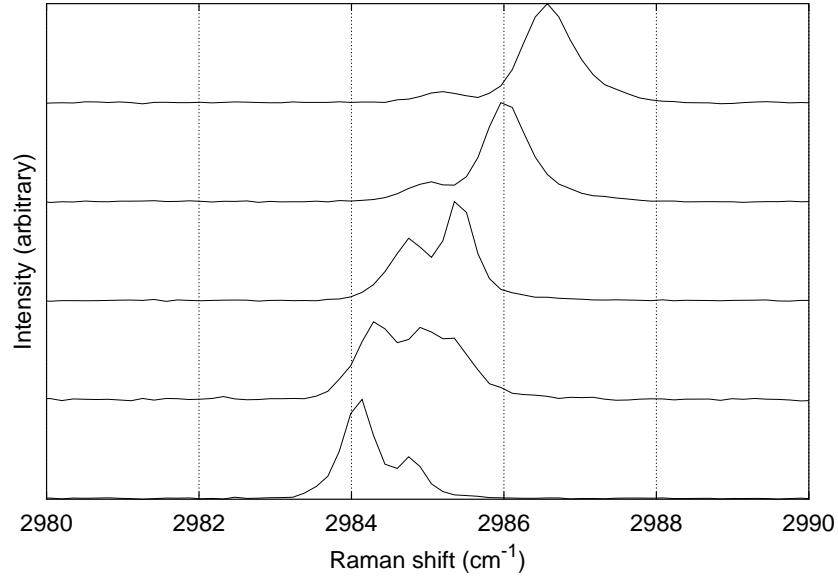


Figure 2.23: The D_2 vibrational spectrum as H_2 is mixed with D_2 . The amount of H_2 is (bottom to top) 0%, 13%, 33%, 47%, and 61%.

average density is decreased as the H_2 is added, because of the large energy difference between isotopes. The straight line in figure 2.24 is equation 2.10 with equation 2.11 used for V and $6\epsilon = 2.2 \text{ cm}^{-1}$. This agrees well with the data.

The D-T data is re-examined using this same formalism. Again, $6\epsilon = 2.2 \text{ cm}^{-1}$, the $Q_1(1)$ and $Q_1(0)$ lines should each move a maximum of

$$6\epsilon \left(\frac{V_0(D_2)}{V(D-T)} \right)^2 c_J = 2.2 \left(\frac{19.94}{19.40} \right)^2 (0.30) (0.33) = 0.23 \text{ cm}^{-1}, \quad (2.12)$$

where 0.30 is the ratio of D_2 in the D-T sample, and 0.33 is the change in $J = 1$ concentration, assuming an initial normal D_2 population decays to 0% $J = 1$. Both $Q_1(0)$ and $Q_1(1)$ are expected to shift the same amount, but in opposite directions so the expected relative shift is 0.44 cm^{-1} . The 0.75 cm^{-1} shift measured in figure 2.21 occurs for a $J = 1$ population decrease from 33% to 15%. While the $Q_1(0)$ line shifts close to the expected amount, the $Q_1(1)$ line shift much further than predicted by equation 2.12. Although the coupling constant of T_2 is unknown, it should not be very different from D_2 . The

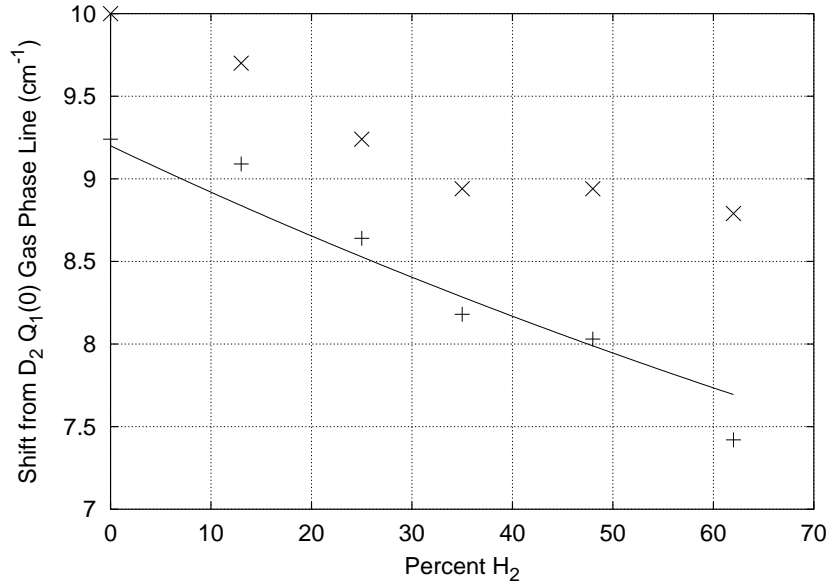


Figure 2.24: The energy shift of the deuterium $Q_1(1)$ (\times) and $Q_1(0)$ ($+$) as H_2 is added. The straight line is from equations 2.10 and 2.11 as described in the text.

measured T_2 shift is also much larger than predicted. Since the density shift required to account for the increased shift is unrealistic, either the coupling is increased in the D-T or another $J = 1$ dependent energy shift is responsible. Clustering of $J = 1$ molecules may account for some of the shift,²³ but this cannot be confirmed from the data.

2.5 Analysis

2.5.1 $J = 1 \rightarrow 0$ conversion rate

The Raman measurements of the $J=1 \rightarrow 0$ conversion rates in D-T are comparable to the previous NMR measurements for T_2 below 8 K. The D_2 conversion rate, however, is slower by a factor of 2 - 4 from 5 to 12 K. Thermal modeling of the Raman system indicates laser heating may be responsible for a 1 K difference between the D-T temperature and the GRT reading. This explains why the D_2 and T_2 decay times increase at a lower temperature than found in the NMR measurements, but does not explain the difference

in τ at lower temperatures.

The likely explanation lies in the difference in sample volumes for each experiment. The NMR experiment used 9×10^{-3} moles of D-T, whereas only 3×10^{-7} moles were used for the Raman experiment. The D-T layer is only $3 \mu\text{m}$ thick when uniformly distributed around the Raman shell. This very large surface-to-volume ratio in the Raman shell enables more of the beta particles to leave the sample, thereby reducing the number available for $J=1 \rightarrow 0$ conversions in the solid. Using Table 17.2 from Souers⁷ shows that 50% of the beta particle energy leaves the $3 \mu\text{m}$ D-T layer. Fewer atoms are created and the reduced atom density lowers the $J=1 \rightarrow 0$ conversion rate. From Sater *et. al.*,¹⁹ the steady state atom concentration goes as the square root of the atom production rate. Thus, only an increase of $\sqrt{2}$ in the decay time is accounted for by this model.

2.5.2 Rotational spectrum

The D-T $J=0-2$ rotational spectrum lineshape has a triplet splitting for the heavier isotope and an asymmetrically broadening for the lighter isotope which was also observed for the mixed, non-tritiated isotopes. Radiation damage does not alter the rotational spectrum of the isotopic mixture. The triplet structure on the $J = 0-2$ transition of the heavier isotope is due to the crystal field splitting in an hcp lattice. The origin of the asymmetric broadening of the $J = 0-2$ transition of the lighter species is currently unknown. One possible explanation is the lighter molecule is forced into a higher density lattice in the mixture than in the pure component. The higher density increases anisotropic interactions and broadens the $J = 0-2$ transition.⁴⁰ The pressure required to compress H_2 to the same density as in the $\text{H}_2\text{-HD-D}_2$ mixture is 20 MPa, compared to the triple point pressure of 7 kPa for H_2 .

2.6 Conclusions

The D-T mixture rotational and vibrational Raman spectra are very different from the pure component hydrogens, but agree well with the non-tritiated mixtures studied here. The radiation damage does not alter the lattice structure, and the D-T lattice is found to be hcp for all temperatures studied in this work. The broadened $J = 0-2$ transition was unexpected, but likely results from anisotropic interactions of the mixture.

A shift in vibration energy with $J = 1$ concentration was found and is explained by the concentration dependent molecular coupling. The $Q_1(1)$ intensity is not enhanced in the mixture as in the pure component because of the large vibrational energy difference between the isotopes.

Chapter 3

Crystal growth and surface roughness

3.1 Background

D-T layers in shells are formed and smoothed by the tritium decay heating. This process is called beta-layering. The surface roughness at 18.3 K of the best layers formed by beta layering is still too high for acceptable NIF ignition targets.^{1,8,9} Infrared heating of the solid or electrical heating of the vapor assists the beta heating and produces near NIF quality solid layers in plastic capsules.^{9,41,42} To better plan the target design and further reduce the layer roughness, the physical processes that set a lower limit on the solid roughness must be understood. The surface energy and the crystal facets of D-T have been neglected in previous theoretical treatments.^{4,5}

The D-T solid distributes itself in a thermal gradient to minimize the total surface and volumetric energy. While this is true for all solids, the process is typically slow. The high D-T vapor pressure near the melting temperature allows the beta layering process to

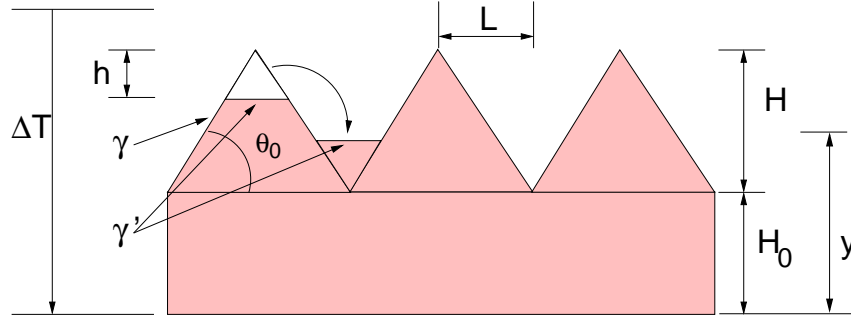


Figure 3.1: Exaggerated model of surface smoothing in a heat flux. The peak of one bump moves under the application of a heat flux to the valley. A new surface with energy γ' is created.

smooth the surface with a time constant of 30 minutes.^{4,6} As shown in the last chapter, D-T is not amorphous, and thus the surface energy depends on the crystal orientation of the surface. Hence, the surface energy of exposed crystal planes may increase as a result of the sublimation. Figure 3.1 shows a simple model of the surface evolution. The initial rough surface consists of triangles with a single crystal orientation exposed which has a surface energy γ . This array of triangles sits on a thick layer. The solid leaves the peak of one triangle to fill in the valley between them, reducing the roughness. In doing so, a surface with energy γ' is exposed. If the initial surface is assumed to minimize the surface energy, then γ' is necessarily larger than γ . The smoothing process ends when the increased surface energy is larger than the thermal energy decrease. The smoothing processes is further slowed if crystal growth proceeds by nucleation on the existing facets. The nucleation process is slower than continuous growth and an energy barrier must be overcome before the crystal grows.

The following simple model from Bernat⁴³ illustrates the smoothing process in a thermal gradient. The orientation dependent surface energy was added to Bernat's model to properly account for the solid anisotropy. Formally, the surface profile is found by

minimizing the total energy, a sum of the thermal energy and the surface energy,

$$E_T = \int_V e(x, y, z) d^3x + \int_S \gamma da. \quad (3.1)$$

e is the thermal energy density and γ is the surface energy. Only the two dimensional solution is considered for simplicity with the temperature gradient due to the bulk heating. For internal heating of \dot{Q} and thermal conductivity k , the temperature at a position y in the layer is

$$T(y) = \frac{\dot{Q}}{k} \left(y_s y - \frac{1}{2} y^2 \right), \quad (3.2)$$

where y_s describes the surface as a function of x , and the heat flux at the surface is set to zero. This model assumes there is little heat flow parallel to the surface.

The volume energy is

$$\int C \rho T dV = \int_{x=-L}^{x=L} dx \int_{y=0}^{y=y_s} C \rho \frac{\dot{Q}}{k} \left(y_s y - \frac{1}{2} y^2 \right) dy, \quad (3.3)$$

where C is the specific heat and ρ is the solid density. Integration over y gives

$$C \rho \frac{\dot{Q}}{k} \int_{x=-L}^{x=L} dx \left(\frac{1}{3} y_s^3 \right). \quad (3.4)$$

The surface is defined as a function of x according to figure 3.1,

$$y_s = \begin{cases} H_0 + h & x = -L \rightarrow -(L-l) \\ H_0 + (H + \frac{H}{L}x) & x = -(L-l) \rightarrow -l \\ H_0 + (H - h) & x = -l \rightarrow l \\ H_0 + (H - \frac{H}{L}x) & x = l \rightarrow (L-l) \\ H_0 + h & x = (L-l) \rightarrow L \end{cases}, \quad (3.5)$$

where h and l define the solid that has been moved.

Only the change in energy is important so $h = l = 0$ is used as the initial state. Integrating equation 3.4 and noting $h/l = H/L = \tan(\theta_0)$, the change in thermal energy is

$$\begin{aligned}\Delta E_T &= \frac{C\rho\dot{Q}}{3k\tan(\theta_0)} (8H_0h^3 - 3H^2h^2 + 4Hh^3 - 6H_0Hh^2) \\ &= \frac{C\rho\dot{Q}}{3k\tan(\theta_0)} (2H_0 + H)(4h^3 - 3Hh^2).\end{aligned}\quad (3.6)$$

In a similar manner the surface energy change is calculated using γ_0 as the facet surface energy and $\gamma(\theta) = \gamma_0 + \gamma_1|\tan(\theta - \theta_0)|$ as the energy of the newly exposed faces, tilted by $\theta - \theta_0$ from the initial facet. Multiplying the surface energy by the appropriate lengths gives the surface energy change

$$\begin{aligned}\Delta E_s &= 4\gamma(\theta_0)l - 4\gamma_0\sqrt{l^2 + h^2} \\ &= \frac{4h}{\tan(\theta_0)} \left(\gamma(\theta_0) - \frac{\gamma_0}{\cos(\theta_0)} \right).\end{aligned}\quad (3.7)$$

The surface is found by summing equations 3.6 and 3.7 and setting the derivative with respect to h to zero. This gives

$$h_{\min} = \frac{H}{4} \pm \frac{1}{2} \sqrt{\frac{H^2}{4} - \frac{4\Delta\gamma}{(2H_0 + H)\alpha}}, \quad (3.8)$$

where $\Delta\gamma = \gamma(\theta_0) - \frac{\gamma_0}{\cos(\theta_0)}$ and $\alpha = C\rho\dot{Q}/k$. The surface is perfectly smooth when $h_{\min} = H/2$. This is approached when $\Delta\gamma$ is small, or for α large. Two conditions are placed on this solution. The first is $\Delta\gamma$ must be positive, consistent with the initial surface being the low energy surface. To first order,

$$\theta_0 \leq 2\frac{\gamma_1}{\gamma_0} \quad (3.9)$$

defines a stable initial surface. Secondly, h_{\min} must be real, hence,

$$H^2 \geq \frac{16\Delta\gamma}{\alpha(2H_0 + H)}. \quad (3.10)$$

This defines the minimum perturbation height smoothed by bulk heating. The surface energy increase is larger than the thermal energy decrease if H is smaller than this size. If $\gamma(\theta_0)$ is known, then the minimum roughness obtainable for a specified heating can be calculated.

Formulation of a model for an applied heat flux F normal to the surface instead of bulk heating is similar, except $T(y)$ is linear in y instead of quadratic,

$$T(y) = \frac{F}{k}y. \quad (3.11)$$

The corresponding volumetric energy change is

$$\Delta E_V = \frac{C\rho F}{3k \tan(\theta_0)} (4h^3 - 3Hh^2), \quad (3.12)$$

which is combined with equation 3.7 to give

$$h_{\min} = \frac{H}{4} \pm \frac{1}{2} \sqrt{\frac{H^2}{4} - \frac{4\Delta\gamma}{\alpha'}}. \quad (3.13)$$

α' is $C\rho F/k$. This model differs from the bulk heating model in that the smoothing ability is independent of layer thicknesses H_0 .

These model assume the initial surface consists of a series of facets. However, if the surface is not faceted, then smoothing is much easier. There is no nucleation barrier for growth and γ is isotropic. The krypton and xenon rare gas crystals grow completely rounded above $0.8 T_{\text{TP}}$.^{44,45} At lower temperatures the crystals are faceted. The transition from a faceted to a rounded surface is known as the roughening transition. Calorimetry data confirm the existence of this transition for Ar and Ne at $0.8 T_{\text{TP}}$.^{46,47} A transition in H_2 was reported at $0.75 T_{\text{TP}}$ using heat capacity measurements of multilayer adsorption on MgO.⁴⁸ Since the hydrogen isotopes and rare gas crystals have similar lattice potentials the hydrogen crystals were also expected to grow rounded above $0.8 T_{\text{TP}}$ and the lower

transition temperature is thought to be due to the higher zero point motion in hydrogen. In order to understand the surface roughness of the D-T surface, both the surface energy and the roughening transition temperature must be determined.

3.2 Crystalline surface energy

The specific surface energy γ is the amount of work required to change the interfacial area.^{26,49,50} The density of molecules and the Van der Waal binding energy at the interface determines the interfacial energy. Crystals are anisotropic, in contrast to fluids, and γ depends on the crystallographic orientation of the exposed surface. In general, molecules in more densely packed surfaces have a lower γ than loosely packed faces. The equilibrium crystal shape (ECS) minimizes the crystal energy. In the absence of external fields the ECS is found by minimizing the surface energy and leads to the Wulff construction of the crystal shape.^{49,51–55} This geometrical construction of the ECS finds facets with area inversely proportional to their energy.

3.2.1 Vicinal approximation

Vicinal surfaces consist of flat facets with a series of steps, as shown in figure 3.2. The molecules on each step have fewer bonds, hence the energy of these slightly tilted surfaces is larger than the flat facet. The step density is proportional to the tilt angle θ so to first order $\gamma(\theta)$ is^{50,51}

$$\gamma(\theta - \theta_0) = \gamma_0 + \gamma_1|\theta - \theta_0|, \quad (3.14)$$

where γ_0 is the specific surface energy for flat facet corresponding to $\theta - \theta_0 = 0$, and γ_1 is the step energy. The absolute value is necessary because the surface energy increase is

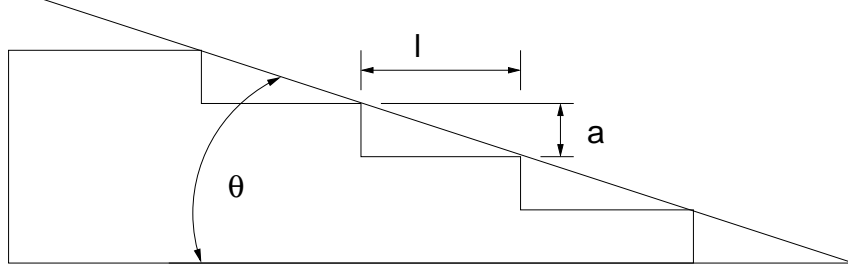


Figure 3.2: A vicinal surface tilted at an angle θ to the facet. Each step is a high and has a width l . The steps increase the surface energy.

independent of the slope direction. An obvious parameterization of $\gamma(\theta - \theta_0) = \gamma_0 \cos(\theta - \theta_0) + \gamma_1 |\sin(\theta - \theta_0)|$ fails to correctly describe the crystal shape, as will be shown shortly.

For simplicity, θ_0 is taken to be 0 in the following. $\gamma(\theta)$ is continuous at $\theta = 0$, but its derivative is not. Landau⁵¹ showed that the slope discontinuity is proportional to the facet size on the ECS using a variational approach. Simply, if γ_1 is large then the surface energy increases rapidly with angle. The flat facet is strongly favored in these cases. A point often overlooked is the relation between the crystal curvature and the second derivative of γ . In two dimensions, the curvature K of a surface is given by

$$K = \frac{y''}{(1 + y'^2)^{3/2}}, \quad (3.15)$$

where y' and y'' are the first and second derivative of the surface. The surface profile described by $y(x)$ is found using the Lagrange equation,

$$\frac{d}{dx} \frac{df}{dy'} - \frac{df}{dy} = 0, \quad (3.16)$$

with⁵¹

$$\int f dx = \int \left(\gamma(\theta) \sqrt{1 + y'^2} + \lambda y \right) dx, \quad (3.17)$$

where λ is the Lagrange multiplier required to ensure conservation of volume. Substitution

and differentiation gives

$$\frac{y''}{(1+y'^2)^{3/2}} \left(\frac{d^2\gamma}{dy'^2} (1+y'^2)^2 + 2 \frac{d\gamma}{dy'} y' (1+y'^2) + \gamma \right) = \lambda. \quad (3.18)$$

From equation 3.15, the factor in front of the parenthesis is the curvature, K . Using $y' = \tan(\theta)$ and the chain rule $\frac{dg}{dy'} = \frac{dg}{d\theta} \frac{d\theta}{dy'}$ the factor in parenthesis is,

$$\begin{aligned} & \frac{d}{dy'} \left(\frac{d\gamma}{dy'} \right) \frac{1}{\cos(\theta)^4} + 2 \tan(\theta) \frac{d\gamma}{d\theta} + \gamma \\ &= \frac{d}{d\theta} \left(\frac{d\gamma}{d\theta} \frac{d\theta}{dy'} \right) \frac{1}{\cos(\theta)^2} + 2 \tan(\theta) \frac{d\gamma}{d\theta} + \gamma \\ &= \frac{d^2\gamma}{d\theta^2} - 2 \tan(\theta) \frac{d\gamma}{d\theta} + 2 \tan(\theta) \frac{d\gamma}{d\theta} + \gamma \\ &= \frac{d^2\gamma}{d\theta^2} + \gamma = \tilde{\gamma}. \end{aligned} \quad (3.19)$$

Substituting into equation 3.18 gives

$$K \tilde{\gamma} = \lambda. \quad (3.20)$$

The crystal curvature is inversely proportional to $\tilde{\gamma}$, known as the surface stiffness. The form for $\gamma(\theta)$ in equation 3.14 with a slope discontinuity makes $\tilde{\gamma}$ infinite, hence $K = 0$ at $\theta = 0$. Away from the facet $\tilde{\gamma} = \gamma(\theta)$. Equation 3.20 shows why $\gamma(\theta) = \gamma_0 \cos(\theta) + \gamma_1 |\sin(\theta)|$ is not a good choice of parameterization. $\tilde{\gamma}$ is zero everywhere except at $\theta = 0$ where it becomes infinite. The crystal is described only by faceted surfaces, which is inconsistent with the roughening transition theory.

3.3 Roughening transition

The previous discussion considered did not include any entropy dependence and is considered valid only for $T = 0$ K. For non-zero temperatures the surface free energy is

$$E_s = \gamma A - TS_{\text{surf}}, \quad (3.21)$$

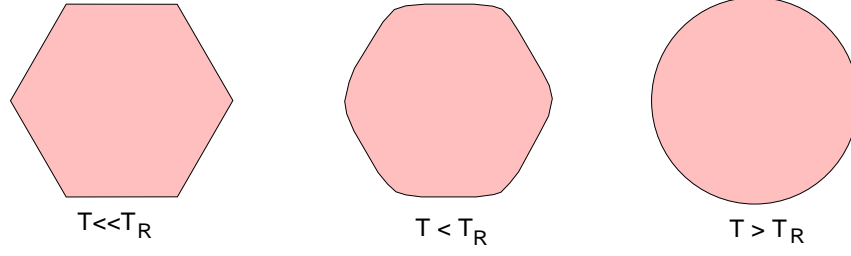


Figure 3.3: The equilibrium crystal shape evolution with temperature. At temperatures much lower than T_R the crystal is completely bounded by facets. Closer to T_R the facets are joined by curved regions. The facets vanish and the crystal is completely rounded above T_R .

where S_{surf} represents the surface entropy. The surface entropy is calculated from the number of different ways a step can be placed on the surface.⁵⁶ The roughening transition temperature T_R is the temperature when the entropy term is equal to the step energy.⁵⁷ Adding additional steps to the surface requires no additional energy. T_R is related to the surface stiffness of a crystal plane according to^{53,56,58–60}

$$T_R = \frac{2d^2\tilde{\gamma}(T_R)}{\pi k_b}, \quad (3.22)$$

where d is the spacing between same or parallel planes. From equation 3.20, the crystal curvature at the facet becomes non-zero at T_R . At this point $\gamma = \tilde{\gamma}$, so the surface energy can be found from T_R . The number of steps on the surface increases and the facet orientation is no longer pinned and the anisotropy in γ vanishes.^{61,62} On the macroscopic scale, the surface changes from a flat facet to a curved surface.^{63–65} The size of the facet shrinks as the roughening temperature is approached with more of the crystal joined by curved regions.^{54,65} Figure 3.3 shows the crystal shape for several temperatures relative to T_R . The shape change is also accompanied by a change in the crystal growth mechanisms.

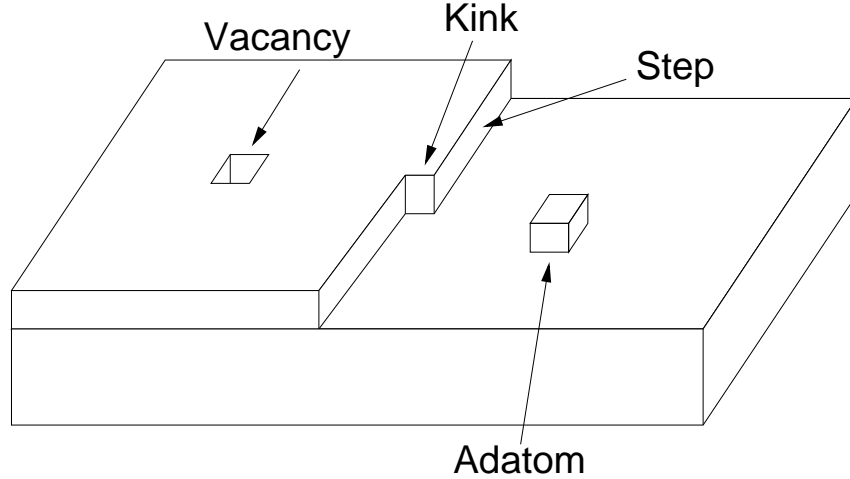


Figure 3.4: The attachment sites of a crystal surface. Each site binds attached molecules with different energies.

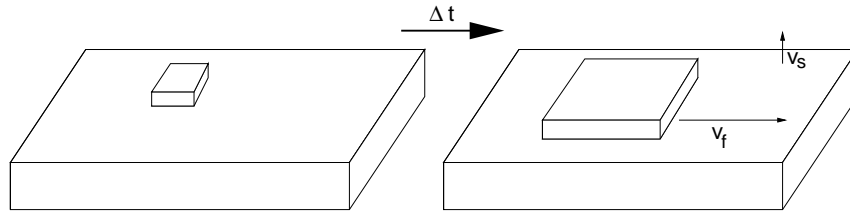


Figure 3.5: A faceted crystal grows when clusters larger than the critical size nucleate on the surface. Growth perpendicular to the surface is much slower than growth parallel.

3.3.1 Crystal growth

Crystals grow by attachment of new molecules to the surface. An atomically rough surface has a number of different molecular attachment sites. In the nearest neighbor approximation, the binding energy holding the molecule to the crystal is the nearest neighbor bond energy multiplied by the number of neighbors.^{50,55,61} For instance, as illustrated in figure 3.4, the ad-atom is held to the surface by one bond, a molecule adsorbed to the step has two bonds, the atoms occupying the kink position has three, and so on.

A faceted surface cannot grow continuously but instead requires nucleation of a molecular cluster larger than a critical size. Nucleation of a new layer on a crystal is similar to the nucleation of a new phase described by Gibb's formulation. The Gibb's free energy

for formation of a new phase is the sum of the volume and surface energy. The Gibb's energy of a spherical droplet of radius r is⁵⁰

$$\Delta G(r) = -\frac{4\pi r^3}{3v_l}\Delta\mu + 4\pi r^2\gamma, \quad (3.23)$$

where v_l is the droplet molecular volume, $\Delta\mu$ is the difference in chemical potential between the two phases, and γ is the surface energy. The Gibbs energy increases for $r < R_c$ and decreases for $r > R_c$, where R_c is the critical size where $\frac{dG}{dr} = 0$. This is the nucleation barrier to growth of a new phase. Clusters smaller than R_c cannot grow, and it is only thermodynamic fluctuations which create nuclei larger than R_c that enables growth.^{26,50,56}

For crystal facets, a simple growth process is two dimensional growth for a flat interface. Since there are no attachment sites for new molecules, an atomically flat surface grows only when thermodynamic fluctuations produce clusters larger than the critical radius.^{50,58} These clusters continue to grow as new molecules arrive at their surface until the entire surface is covered by the new layer, as shown in figure 3.5 Further growth is prevented until a new stable cluster is formed on the surface.

By contrast, roughened crystal planes grow rapidly.^{50,58,56} Molecules arriving at the surface attach to any of the numerous sites available on a rough surface. In this case, only the flux of atoms to the surface limits the crystal growth rate. When a crystal is bounded by both facets and rough regions, growth perpendicular to the rough surface is much faster than the facet.^{50,66,54} Growth proceeds much faster parallel to the facets, increasing their size at the expense of the faster growing direction, illustrated in figure 3.6. Growth proceeds until the crystal is completely bounded by facets.

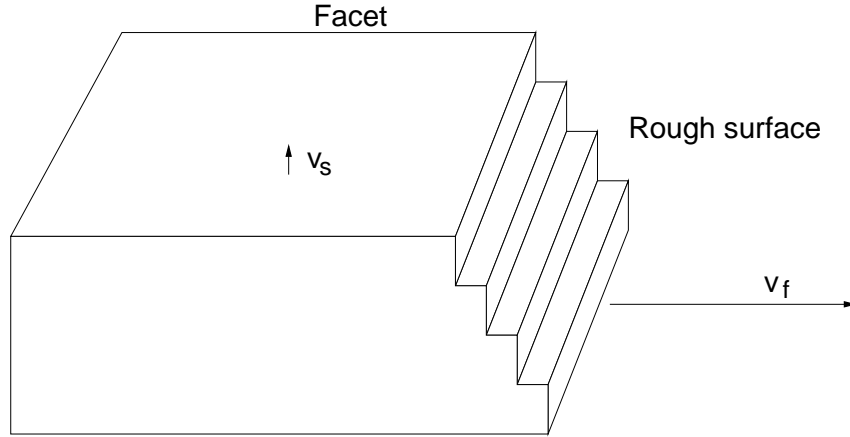


Figure 3.6: Growth of a crystal with one face faceted and the others roughened. Growth perpendicular to the roughened surface leaves a large faceted face.

3.3.2 Kinetic roughening

The above discussion assumes that the growth of crystals occurs near equilibrium for ideal crystals. However, for systems that are not in equilibrium, the crystal may become kinetically roughened.^{50,56} Simply, the atoms arrive at the surface much more rapidly than they find their equilibrium positions. This occurs for instance when the super-saturation is very high and the crystal equilibrium vapor pressure is low. In this case, the rate molecules leave the surface is much lower than their arrival rate and the crystal is grows out of equilibrium.

Defects in crystals lead to growth of an otherwise atomically flat surface. Dislocations which intersect the surface serve as a constant site for new growth. Growth fronts which spiral around such sources allow the surface to grow continuously.⁵⁶

3.3.3 Expected transitions

The rare gas crystals discussed in section 3.1 all have the fcc lattice structure, in contrast to the hcp hydrogen lattice. ^4He crystals are also hcp and their properties should be similar to the hydrogen crystals. Three distinct crystal planes of ^4He crystals grown

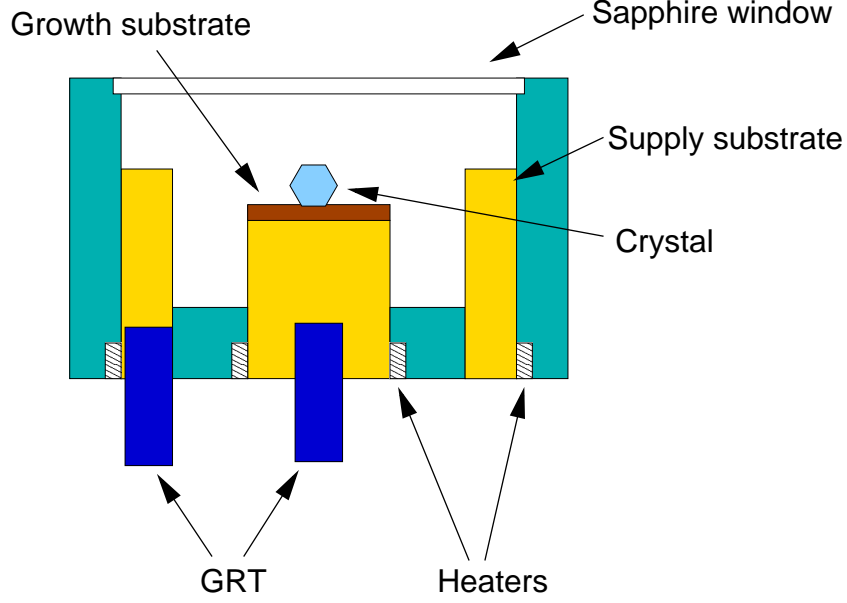


Figure 3.7: Crystal Growth Cell.

under pressure from the superfluid roughen.^{58,67-71} The transitions are $T_r^{(1\bar{1}01)} = 0.3K < T_r^{(10\bar{1}0)} = 0.9K < T_r^{(0001)} = 1.3K$. The surface energy is determined only by the bond energy and crystal plane, hence the same transition ordering and ratios are expected for the hcp hydrogen crystals. D_2 and HD were used in the following experiments.

The roughening transition is determined by the disappearance of crystal facets as done for Xe and Kr^{44,45} and ^4He .^{58,67-71} The growth velocity provides another indication of roughened planes. Growth perpendicular to facets is much slower than for roughened surfaces. However, the supersaturation could not be determined accurately enough to establish the growth rate dependence on supersaturation as done for ^4He .^{58,71}

3.4 Experimental design

The cross section of the crystal growth cell is shown in figure 3.7. A copper cylinder and ring were brazed into the stainless steel cell body. The stainless steel provided the thermal

standoff required to independently control the supply and growth substrate temperatures. Wire wrapped heaters and calibrated germanium resistance thermometers (GRT) were used to control and monitor the two temperatures. A capacitance manometer monitored the vapor pressure in the cell and was used, along with the known D_2 triple point, to calibrate the GRTs. The deuterium equation of state from Souers⁷ and the GRTs agreed to within 0.05 K. A diamond turned copper disk, a $\langle 111 \rangle$ cut silicon wafer, and a sapphire disk were used as growth substrates. The substrates were attached to the copper cylinder using AirProduct's Cry-con grease.

The cell was attached by a crushed indium gasket to the liquid helium cooled heat exchanger of the Oxford Instruments Special Variox optical cryostat (not shown). A liquid nitrogen cooled radiation shield surrounded the growth cell and heat exchanger. The 2 mm thick c axis cut sapphire windows on the cell and outer vacuum jacket and the 0.5 mm thick BK-7 window on the radiation shield allowed optical access. The cell temperature was stable to within ± 5 mK over several hours. The D_2 and HD gases were high purity research grade with 99.98% and 97.0% purity. Except where noted, the D_2 J = 1 concentration was close to the normal concentration of 33%.

A frequency stabilized HeNe laser ($\lambda = 632.8$ nm) was used in a Michelson interferometer to study crystal facets. The interference pattern was collected with a microscope and imaged onto a Sony XC-77RR CCD video camera. The video signal was recorded on a VCR and the images were digitized with an 8 bit RasterOps Video ColorBoard 364. A Phase Shift Technologies white light phase shifting interferometer was used in a few cases to reconstruct the crystal surface.

The crystals were grown from the vapor as follows. The solid was initially deposited on the supply substrate. The growth substrate temperature was lowered relative to the

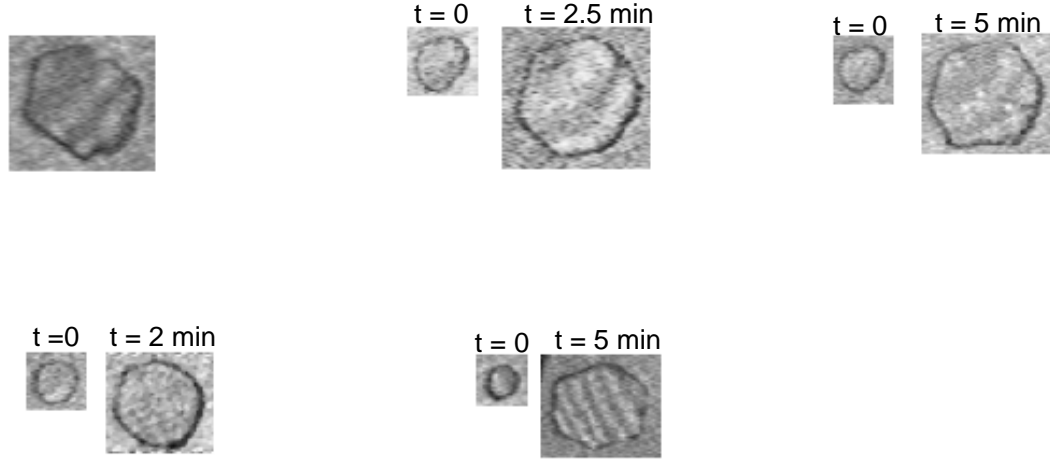


Figure 3.8: D_2 crystals grown at $16.2\text{ K} = 0.86\ T_{TP}$. The crystal was repeatedly grown and evaporated and tends to grow faceted.

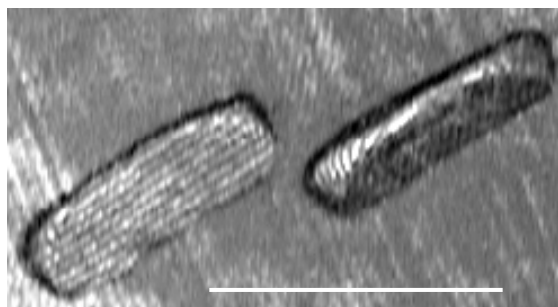
supply substrate until crystals nucleated. The initial nucleation typically produced many randomly oriented polycrystalline crystals. If a crystal was found that was not polycrystalline, the crystals were evaporated until only a small seed remained. The crystal was then re-grown from the seed at the desired rate.

3.5 Experimental results

D_2 and HD crystals were grown on the three different substrates from about $0.8\ T_{TP}$ to T_{TP} . Below $0.8\ T_{TP}$ the crystals approach equilibrium very slowly. Most of the nucleated crystals were randomly oriented and polycrystalline. However, several distinct single crystal shapes were observed. These crystals are presented here for each of the three substrates and for a number of temperatures.

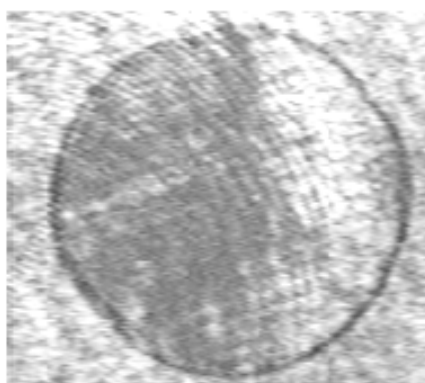
3.5.1 Crystals grown on copper

Figures 3.8 – 3.10 show D_2 crystals grown on the copper substrate. The images in figure 3.8 show a crystal repeatedly grown and evaporated to a small seed at 16.2 K , $0.86\ T_{TP}$.



400 μm

Figure 3.9: D₂ crystals grown from the vapor at 18.53 K. The facet is tilted relative to the substrate, as indicated by the interference fringes.



475 μm

Figure 3.10: D₂ crystal grown from the vapor at 18.7 K. The facet is parallel to the substrate.

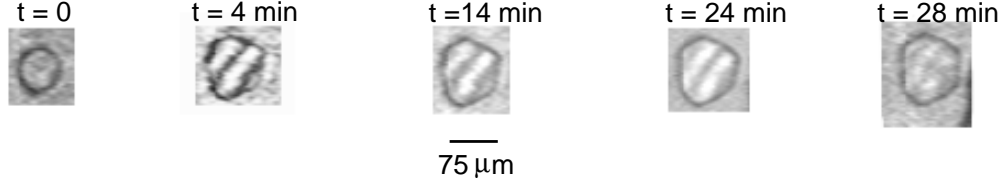


Figure 3.11: HD crystal grown at $14.05 \text{ K} = 0.85 T_{\text{TP}}$. One facet is nearly parallel to the substrate and a series of other facets are apparent on the sides of the crystal.

The growing crystal is hexagonal with faceted edges dominating the shape. The crystal is not an equilateral hexagon, however, and the facet lengths are different. The corners are slightly rounded and in one case the growing crystal is significantly rounded. In contrast, the crystals grown near T_{TP} lack the hexagonal shape. Instead, the crystals are often disks or bar like structure seen in figures 3.9 and 3.10. The length of the crystals in figure 3.9 grew about $1.0 \mu\text{m/s}$, while the radius of the crystal shown in figure 3.10 grew at $3.0 \mu\text{m/s}$. The interference fringes indicate that the bars consists of at least one facet. It is unclear whether a second, distinct facet exists on the bars. The bar like crystals are likely the disk shape crystals which nucleated with the c facet tilted relative to the substrate.

Figures 3.11 and 3.12 show HD and $J = 0 \text{ D}_2$ crystals, respectively. Both the $J = 0$ and HD crystals exhibited shapes similar to the normal D_2 crystals grown at the equivalent fraction of T_{TP} . The HD crystals grown at $14.05 \text{ K} = 0.85 T_{\text{TP}}$, are hexagonal, similar to the D_2 crystals. Although the crystal grows only a few microns after the first four minutes, the shape changes becoming more hexagonal as time progresses. The $J = 0 \text{ D}_2$ crystal grown at $16.65 \text{ K} = 0.89 T_{\text{TP}}$ is not hexagonal. Rather, the curved regions dominate the shape and the facets are smaller than the lower temperature crystal. At lower temperatures the $J = 0 \text{ D}_2$ crystals grew with a shape nearly identical to the normal D_2 crystals.



Figure 3.12: $J = 0$ D_2 crystal grown at $16.65 \text{ K} = 0.89 \text{ T}_{\text{TP}}$.

3.5.2 Crystals grown on silicon

D_2 crystals grown on $\langle 111 \rangle$ silicon are shown in figures 3.13 – 3.16. The single crystals grown near T_{TP} are almost exclusively bar shaped, similar to those grown on the copper substrate. However, in contrast to crystals grown on the copper substrate, the length was measured to be 20 times larger than the width in some cases when grown on the silicon substrate. The crystal in figure 3.13 grew with rates $2.2 \mu\text{m/s}$ in length, and $0.15 \mu\text{m/s}$ in width. The crystal in figure 3.14 was grown slower, at $0.15 \mu\text{m/s}$ in length, and less than $0.005 \mu\text{m/s}$ in width.

Another striking feature of crystals growth on silicon was the parallel growth, as shown in figure 3.15. The growth rate averaged $2.8 \mu\text{m/s}$ in length, and $0.45 \mu\text{m/s}$ in width for all crystals. Growth was not always in the same direction, as shown in figure 3.16. However, the difference in growth direction is very close to 45° , coinciding with the silicon symmetry. It appears the silicon substrate preferentially orients D_2 crystal growth.

However, not all crystals grew as bars, as shown in figures 3.17 and 3.18. The radius grew at $0.18 \mu\text{m/s}$ for figure 3.17. The growth rate of the crystal in figure 3.18 is $1.3 \mu\text{m/s}$ and $0.4 \mu\text{m/s}$ for the outer and inner radii, respectively. These HD crystals consists of a flat facet which joins the curved surface with a discontinuous change in slope. Figures 3.19

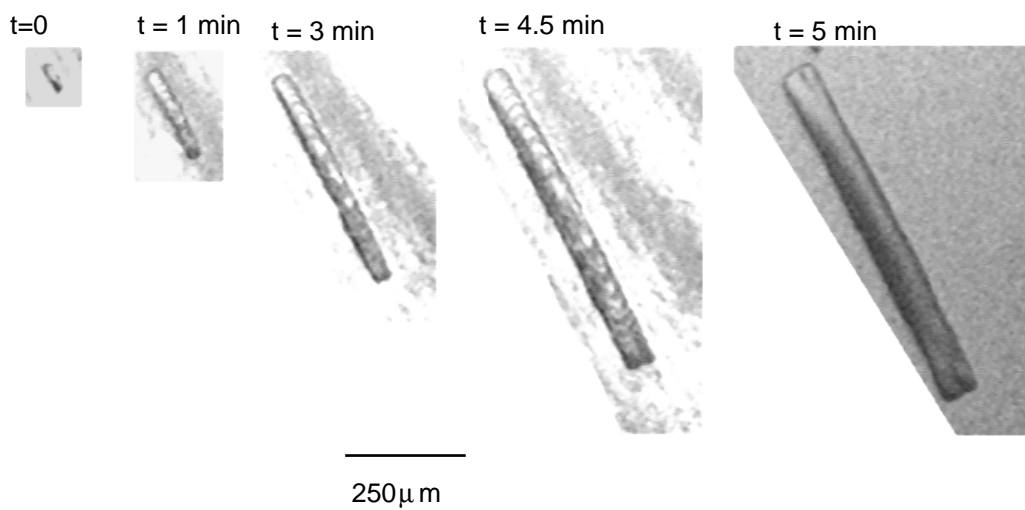


Figure 3.13: D_2 crystal grown at 18.68 K on Si substrate.

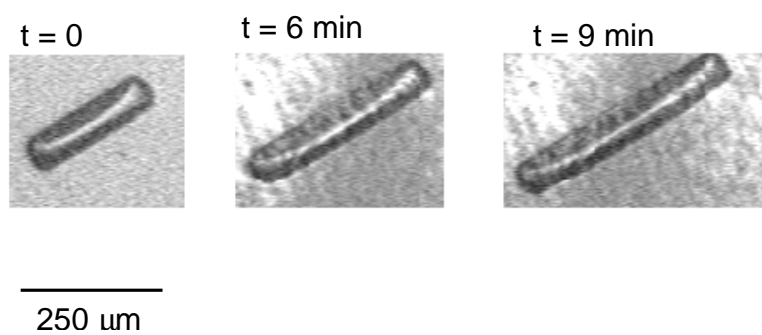
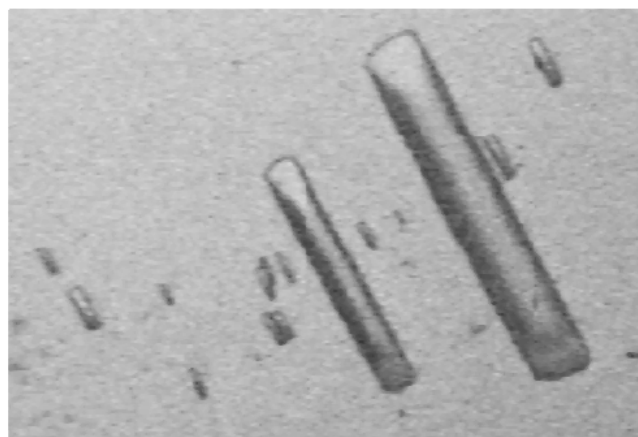


Figure 3.14: D_2 crystal grown at 18.71 K.



450 μ m

Figure 3.15: D₂ crystals grown at 18.68 K show a striking short range order.

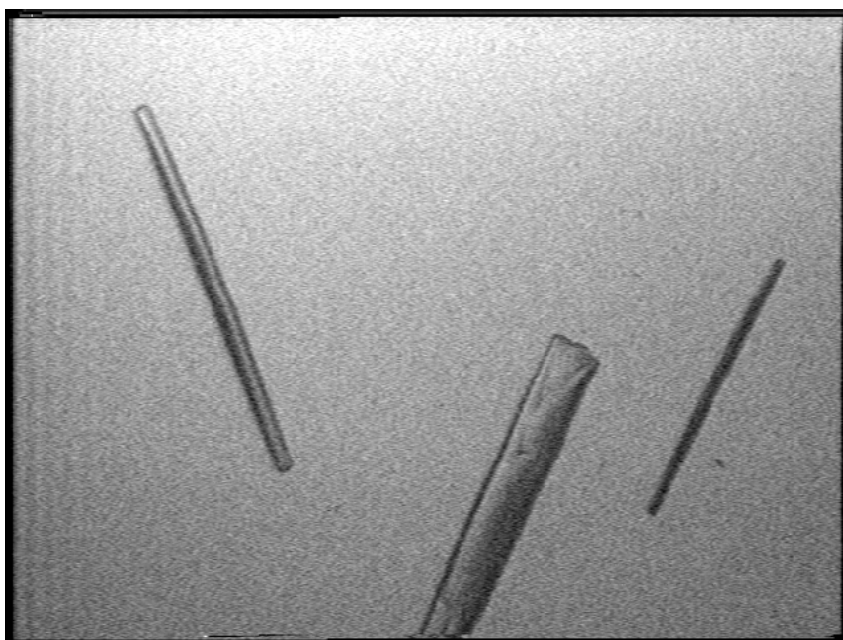


Figure 3.16: D₂ crystals grown at 18.68 K on the Si substrate. The angle between the left most crystal and the two on the right is $45^\circ \pm 5^\circ$.

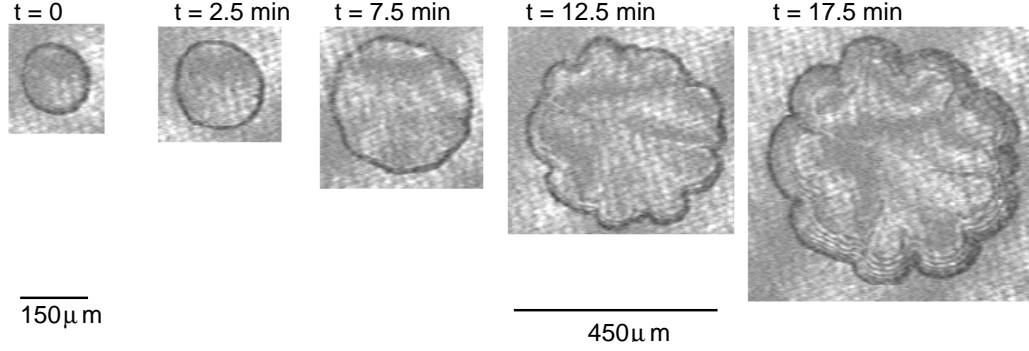


Figure 3.17: HD crystal grown at 16.56 K.

and 3.20 shows the reconstructed surface for figure 3.18 from the white light interferometer.

These images make both the facet and the slope discontinuity readily apparent.

The facets are not perfectly flat, however. A number of defects are visible in figure 3.17 near the facet edge and may be the source for the rather rapid growth perpendicular to the facet. Similarly, the lower right corner of the facet in figure 3.18 is significantly distorted, especially in the later images.

Figure 3.21 shows an HD crystal grown near T_{TP} . It was initially grown by evaporating from a very large crystal, then re-growing while it was still large. This crystal looks identical to figure 3 of Carmi *et al.*,⁷² and the a and c directions are identified by comparison with their work. The round shape indicates the a faces are roughened while sharp c faces are faceted. This crystal was evaporated down to a small seed and re-grown. Its shape was a very long bar shape crystal, very similar to those shown earlier for D_2 .

3.5.3 Crystals grown on sapphire

The D_2 crystals grown on c axis cut sapphire are shown in figures 3.22 – 3.26. As for the copper substrate, the low temperature crystals are hexagonal. The crystal in figure 3.22 is grown at $15.7\text{ K} = 0.84 T_{TP}$ very slowly over 1.5 hours. The initial growth rate was

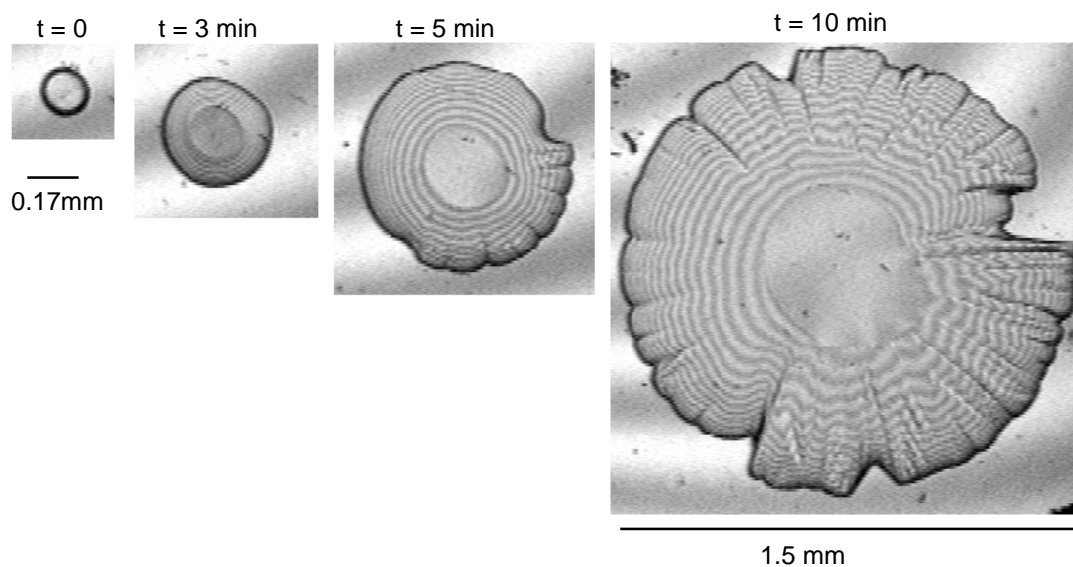


Figure 3.18: HD Crystal grown from the vapor at 16.6 K. The interference fringes are from the white light interferometer. The curved sides meet the flat top with a discontinuous slope change.

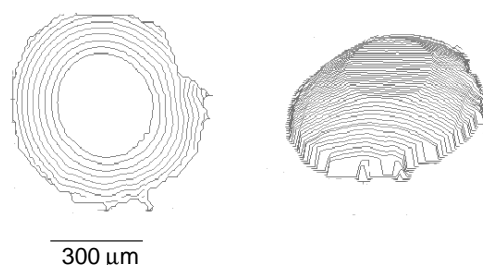


Figure 3.19: Phase map and reconstructed surface from the phase shifting white light interferometer. The contour spacing on the left image is $1.1 \mu\text{m}$ per contour.

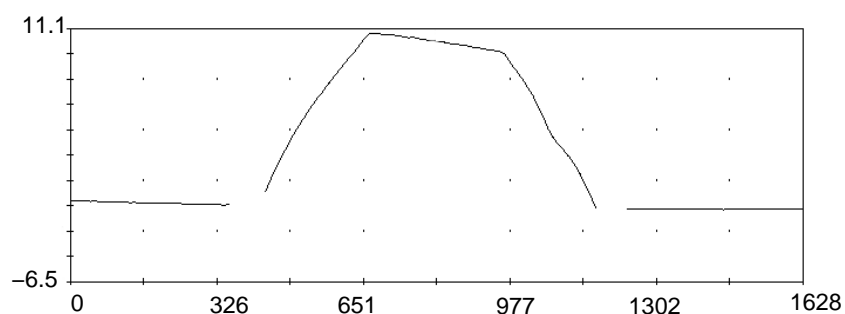


Figure 3.20: Surface profiles for the HD crystal using the white light interferometer through the center of the crystal. The absolute crystal height is unknown because the interference fringes are too steep to be tracked where the crystal meets the surface. Both scales are in microns.

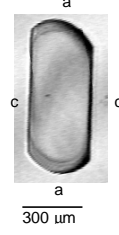


Figure 3.21: HD crystal grown at 16.6 K. The top and sides appear flat, but the front is rounded. The c and a faces are identified with a similar crystal in figure 3 of Carmi *et al.*⁷²

0.08 $\mu\text{m/s}$, and slowed to 0.0019 $\mu\text{m/s}$ after the first six minutes. Flat facets are visible throughout the growth, even though the shape continues to evolve. The single crystal grows very little during the observation. By contrast, a polycrystalline crystal growing under the same conditions is shown in figure 3.23, with the crystal from figure 3.22 seen in the upper right corner of the last image. Two smaller crystals grew into each other to make the crystal in the first image. The dramatic difference between the growth of a single, faceted crystal and that of a poly-crystal is obvious. The poly-crystal starts with several of the hexagonal faces, but its evolution is very different from the single crystal. It grows many times faster than the single crystal, and it deviates significantly from the hexagonal shape, although some evidence of the initial shape is still visible at 1.1 hours. The crystal defects where the smaller crystals initially grew together are clearly visible on all images. These defects provide nucleation sites for nearly continuous growth compared to the single crystal.

A triangular shape is also observed at 0.84 T_{TP} , in addition to the hexagonal crystal. Figure 3.24 shows crystals that nucleated with a triangular shape. These crystals were grown from a higher super-saturation than the hexagons and do not appear to be an equilibrium shape. The corners of the upper right and lower left crystals in the image become rounded as the crystal continues to grow.

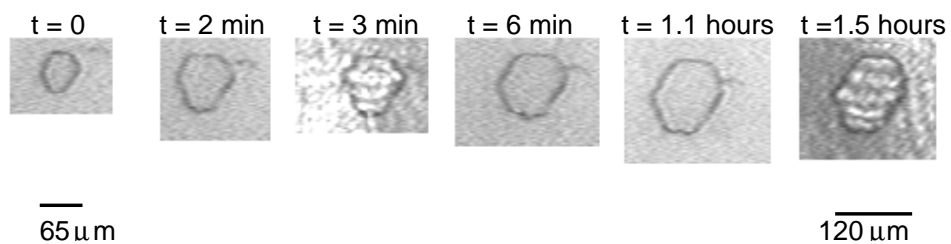


Figure 3.22: D_2 crystal grown at $15.7\text{ K} = 0.84\text{ T}_{TP}$ from the vapor.

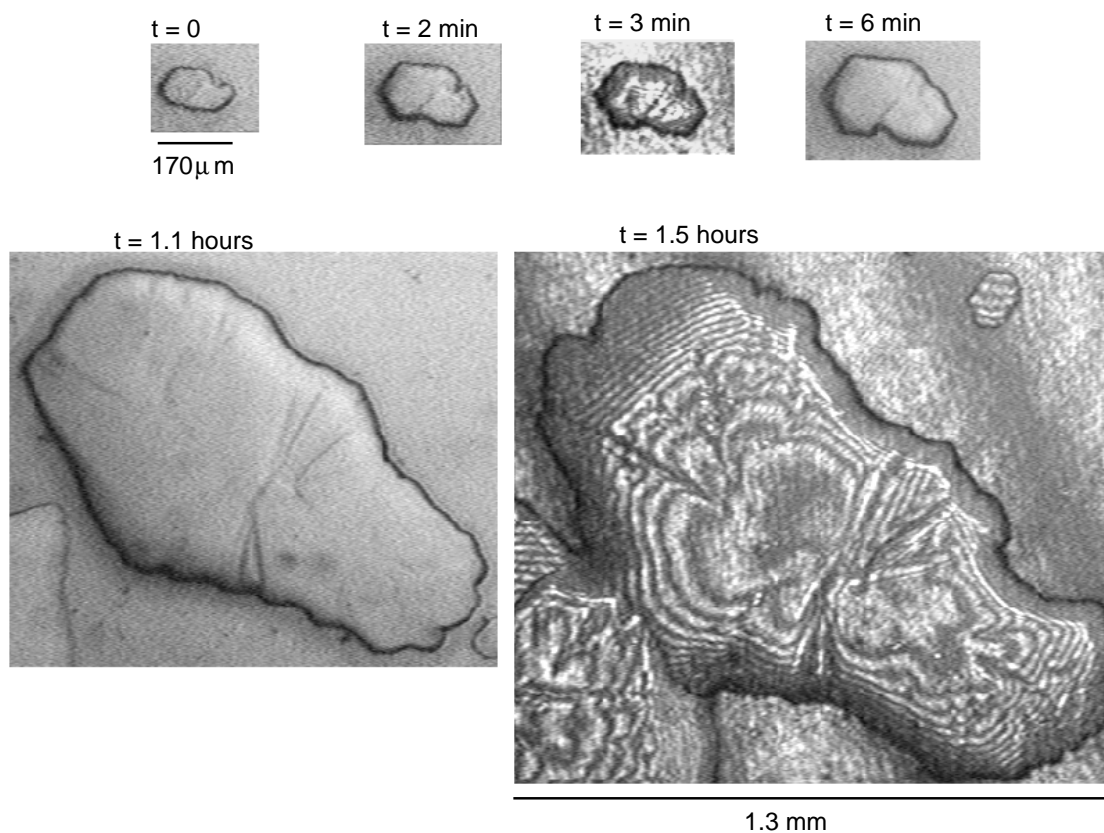


Figure 3.23: D_2 crystal grown under the same conditions as in figure 3.22. The initial defects allow continuous growth, compared to the crystal in figure 3.22, which is visible in the upper right corner of the last image.

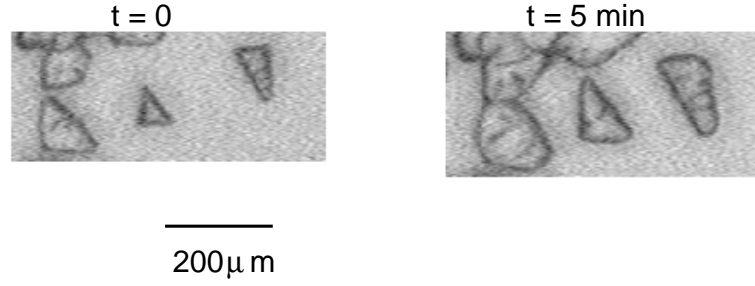


Figure 3.24: D_2 crystals grown from the vapor at $15.7\text{ K} = 0.84\text{ T}_{\text{TP}}$ on the sapphire substrate. The crystals nucleated rapidly and take the triangular shape.

D_2 crystals grown near T_{TP} are similar to the HD crystals grown on silicon, shown in figure 3.25. The inner and outer radii grew at $0.08\text{ }\mu\text{m/s}$ and $0.15\text{ }\mu\text{m/s}$, respectively. The flat facet joins the curved sides with a discontinuous slope change. Again, a defect in the upper right of the facet is the likely source for continued growth perpendicular to the facet. Similarly, the bar like crystals were also observed on the sapphire substrate, as seen in figure 3.26. Finally, in contrast to crystals grown on both silicon and copper, a few crystals grown near T_{TP} had a hexagonal shape. Figure 3.27 shows a crystal that does not have facets, but its shape does have hexagonal symmetry. Its equivalent radius grew at $0.057\text{ }\mu\text{m/s}$. The shape becomes even more round as it continues to grow, with little of the initial hexagonal symmetry present after 15 minutes.

Figure 3.28 shows neon crystals grown under similar conditions as the D_2 and HD crystals. The neon crystals grow nearly isotropically, in marked contrast to the hydrogens. In particular, no facets are visible above 0.8 T_{TP} for neon crystals.

3.6 Analysis

The presence of crystal facets and the difference in growth rates between the single crystal and the poly-crystal indicates the D_2 and HD crystals have two facets up to $0.89\text{ T}_{\text{TP}}$.

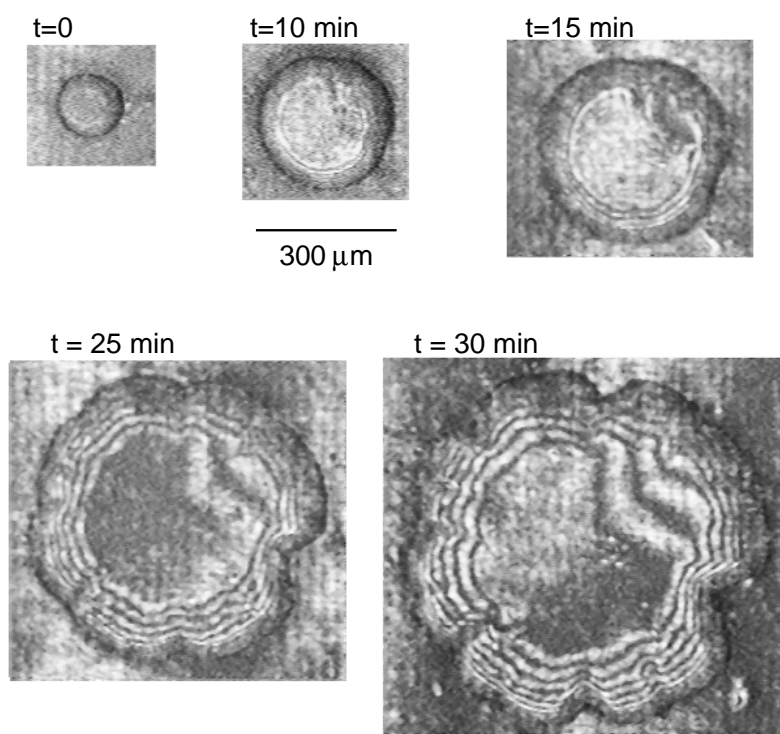


Figure 3.25: D_2 crystal growing from the vapor at 18.72 K.



Figure 3.26: D_2 crystal grown on the sapphire substrate.

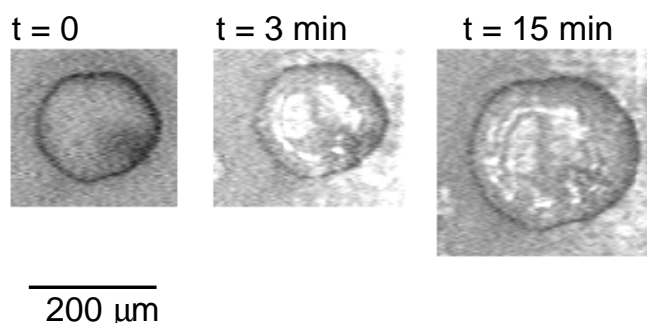


Figure 3.27: D_2 crystal grown from the vapor at 18.72 K.

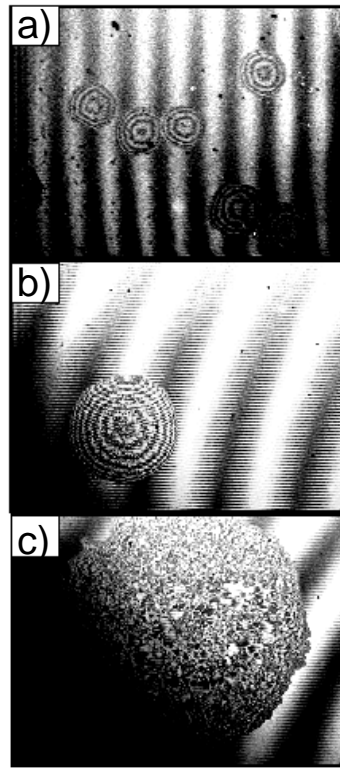


Figure 3.28: Neon crystals grown above their roughening temperature. Their shape is very different from that observed for both D_2 and HD crystals.

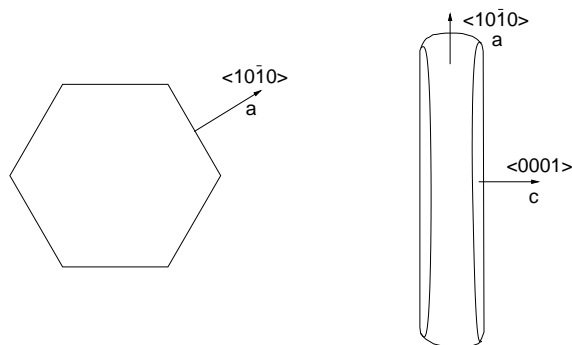


Figure 3.29: Identified crystal facets. The a-faces are the sides and the c-face is parallel to the page for the hexagon. The c-face is the long face on the bar crystal, while the roughened a-face is the smaller side.

Closer to T_{TP} round crystals with one facet are observed. The large difference in growth velocities of the bar crystals indicates the long side is faceted, while the short side is a roughened crystal plane.

3.6.1 Identification of crystal planes

The facets are identified as follows. The faces of the hexagonal shaped crystals are the easiest to label. The two facets with the highest T_R are the $\langle 10\bar{1}0 \rangle$ and the $\langle 0001 \rangle$ families of planes, with $\langle 0001 \rangle$ being the higher of the two.^{58,68,73,62} The hexagonal symmetry is used to designate the $\langle 10\bar{1}0 \rangle$ as the sides of the hexagon and the $\langle 0001 \rangle$ as the planes parallel to the substrate, as shown in figure 3.29. Similarly, the facet on the flat, round crystals grown near T_{TP} is the c facet. The c facet is the long sides of the bar shaped crystals, while the short side is a roughened a facet, based on the identification by Carmi *et al.*⁷² for ^4He crystals and the relative growth rates in the two directions.

The 6 a facets are the same length on an ideal crystal below the roughening temperature. However, the a facet lengths of a given hydrogen crystal are not identical, as seen in figures 3.11 and 3.22. Furthermore, the crystals were often composed of both round and faceted a faces, as shown in figures 3.8 and 3.12. The interaction with the substrate likely plays a role in the growth rate of facets. The non-equilateral a facets were also observed on ^4He grown free of the substrate,⁷¹ and were attributed to surface defects on the facets themselves.

The roughening transition of the a facet is between $0.9 T_{TP}$ and T_{TP} . T_{TP} is used to set an upper bound on the roughening transition. $T_R^{(0001)}$ is obtained by scaling from $T_R^{(10\bar{1}0)}$ by the same ratio of 1.33 found for ^4He crystals. Then $D_2 T_R^{(0001)} = 25 \text{ K}$, which allows an estimate of $6.0 \times 10^{-3} \text{ J/m}^2$ for the surface energy of the (0001) plane at T_R .

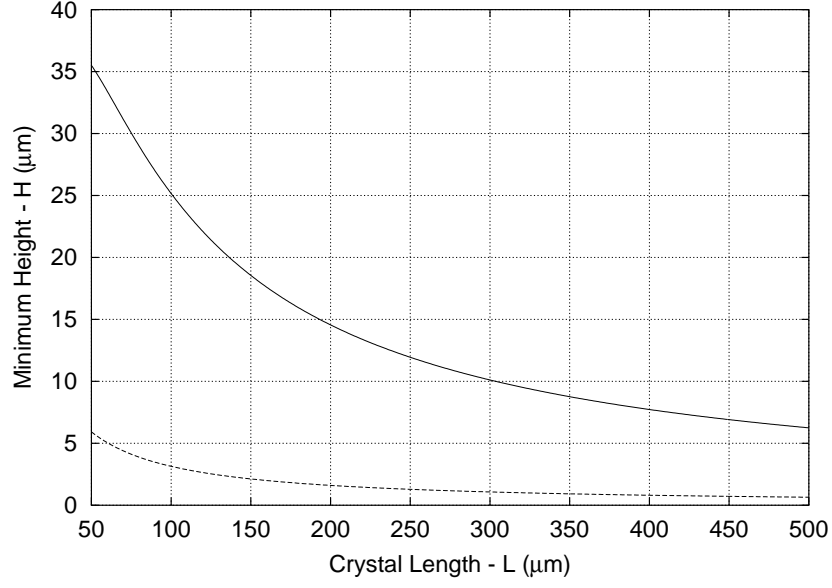


Figure 3.30: Minimum size perturbations that can be smoothed by bulk heating as a function of their length for native beta heating (solid) and 10 times the beta heating power (dashed). Smaller crystals are harder to smooth than large ones.

For comparison, the liquid D₂ surface tension is⁷ $3.8 \times 10^{-3} \text{ J/m}^2$ at T_{TP} .

3.6.2 Surface roughness

The surface roughness of a layer described in section 3.1 is calculated using γ as determined above. The minimum perturbation size smoothed by bulk heating as described by equations 3.10 and 3.8 is calculated as a function of the crystal length L for a $100 \mu\text{m}$ thick layer. The essential features are illustrated using the estimated value $\gamma_0 = \gamma_1 = 6.0 \times 10^{-3} \text{ J/m}^2$. Figure 3.30 shows the minimum height H that can be smoothed for a crystal of length L using both the native beta heating rate and ten times that amount, as is typical using infrared heating to enhance the beta heating.⁴² The thermal energy change cannot compensate for the increased surface energy for smaller values of H .

The figure shows that smaller crystals are much more difficult to smooth than large crystals. This indicates the ideal NIF target consists of a small number of large crystals.

A recent survey of D-T layers grown in shells confirms this model.⁷⁴ Layers formed by supercooling liquid D-T have many crystals with length scale of 100-200 μm produced by the rapid solidification. The surface roughness after several beta layering time constants is much higher than layers produced by slowly cooling through the melting temperature, resulting in crystals with length scales on the order of 500-1000 μm . The highly idealized model neglects the variations in initial crystal sizes and orientations observed in physical systems. A better model must incorporate the initial nucleation and growth for a super-cooled liquid as well as the grain boundary energy and capsule curvature⁷⁵ in determining the initial surface structure. However, this model and surface energy describe the behavior observed for hydrogen crystals grown on flat surfaces with an applied heat flux.⁴³

3.7 Conclusions

The D_2 and HD crystals grow very different from the rare gas crystals near their respective melting temperatures. The c facet persists until the crystal melts for the hydrogen isotopes. The a facet exists up to at least $0.89 T_{\text{TP}}$. In contrast, all rare gas crystals, except ^4He , grow completely round above $0.8 T_{\text{TP}}$. The low energy facets compete with the thermal energy and set a lower limit on the surface roughness of a D-T layer in a shell. Further, recent observations of D-T layers grown in shells indicates layer roughness is correlated with the crystal growth.⁷⁴ The shape of crystals grown in shells resembles those presented in this chapter. Solidification proceeds by supercooling, which produces many small crystals, slow growth of several bar-shaped crystals, or slow growth with a single growth front. Supercooling results in the roughest layers as the small crystals resist thermal smoothing. A single slow growth front produces smoother layers than multiple growth fronts because there are fewer grain boundaries.

The surface energy and crystal planes were identified for several crystal shapes grown from the vapor. We need to determine the effect, if any, the shell curvature has on growing crystals in NIF targets. This requires crystal growth of isotopic mixtures from the liquid phase. The lower interfacial energy of the solid–liquid interface reduces T_R , possibly enabling observation of the c facet roughening. Experiments growing crystals free of the substrate are needed to eliminate substrate effects similar to those observed on silicon.

Of particular interest is the shape of bubbles in the solid. A bubble has the same shape as a crystal of the same volume because the shape is determined only by the surface energy. Additionally, the bubble exists in the bulk solid, eliminating any external effects such as the substrate in crystal growth. The composition of the gas phase has little effect on the surface energy because the gas density is much lower than the solid density. Therefore, ^3He bubbles in D-T are expected to have the same shape as a freely growing D-T crystal, hexagonal cylinders when grown below the a face roughening temperature. The ^3He produced by beta-decay leads to several other interesting features discussed in the next chapter.

Chapter 4

Helium Evolution in D-T

4.1 Background

The recent demonstration of smooth, uniform D-T solid layers in NIF scale targets^{4,5,8,41,42} is a significant advance and makes understanding ^3He in targets more important. The ^3He produced ages the target, potentially reducing the targets yield. Predicting target performance and optimizing the design requires knowing the ^3He concentration in the D-T solid and vapor regions and how it changes with time, temperature, and layer thickness.

The ^3He can stay as atoms in the lattice, diffuse to the center vapor region, or nucleate and coalesce into bubbles, as illustrated in figure 4.1. The ^3He reduces target performance in the following ways. First, ^3He in the center vapor region increases the pressure and particle density, requiring more driver energy to compress the vapor and raise the temperature. The thermal conductivity of the vapor is increased as ^3He is added, decreases the thermal smoothing of the D-T solid surface.^{4,6} Finally, ^3He bubbles in the D-T solid seed hydrodynamic instabilities which would degrade capsule performance.

Figure 4.2 shows the progression of bubbles in a layer. Near T_{TP} the helium diffuses

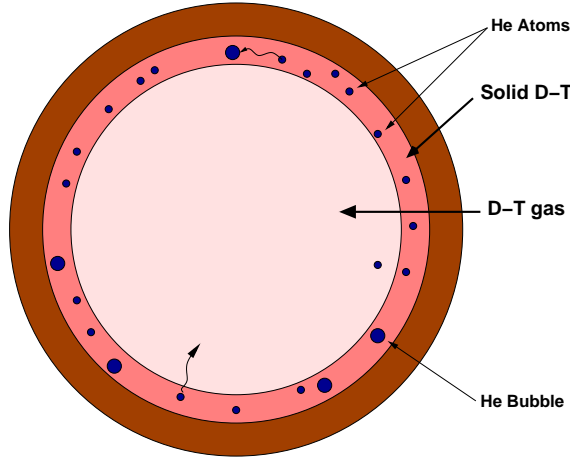


Figure 4.1: The ^3He atoms can remain in the solid, diffuse into the vapor region, or coalesce into bubbles.

rapidly through the layer. Bubbles larger than $10\ \mu\text{m}$ grow in layers thicker than $100\ \mu\text{m}$, while no bubbles are observed in thinner layers. As the temperature is lowered the number of bubbles increases, while their size decreases. Bubbles larger than $\approx 1\ \mu\text{m}$ are not observed below 16 K. However, D-T becomes cloudy, indicating scattering from bubbles on the order of the wave length of light. Below 10 K the layers remain clear.

Tritium is converted into ^3He at a rate of 0.015% per day. At this rate it takes only a few weeks for the ^3He to have a significant impact on target performance. The D-T vapor is at much lower density than the solid allowing its contribution to the ^3He production to be neglected. Assuming rapid ^3He diffusion and a low steady state ^3He concentration in the solid, the ^3He number density in the vapor region is

$$n(t) = \frac{\frac{4}{3}\pi (a^3 - (a-l)^3) \rho \alpha}{\frac{4}{3}\pi (a-l)^3} t, \quad (4.1)$$

where a is the shell radius, l is the layer thickness, ρ is the D-T density in moles/ m^3 , α is the D-T activity in Bq/mole, and t is the time in seconds since the target was filled. Using the D-T density of 5.03×10^4 moles/ m^3 and activity⁷ $\alpha = 1.07 \times 10^{15}$ Bq/mole, a $100\ \mu\text{m}$ thick D-T layer in a 1 mm radius shell has $n(t) = 2.01 \times 10^{19} t\ 1/(\text{m}^3 \cdot \text{s})$. Figure 4.3

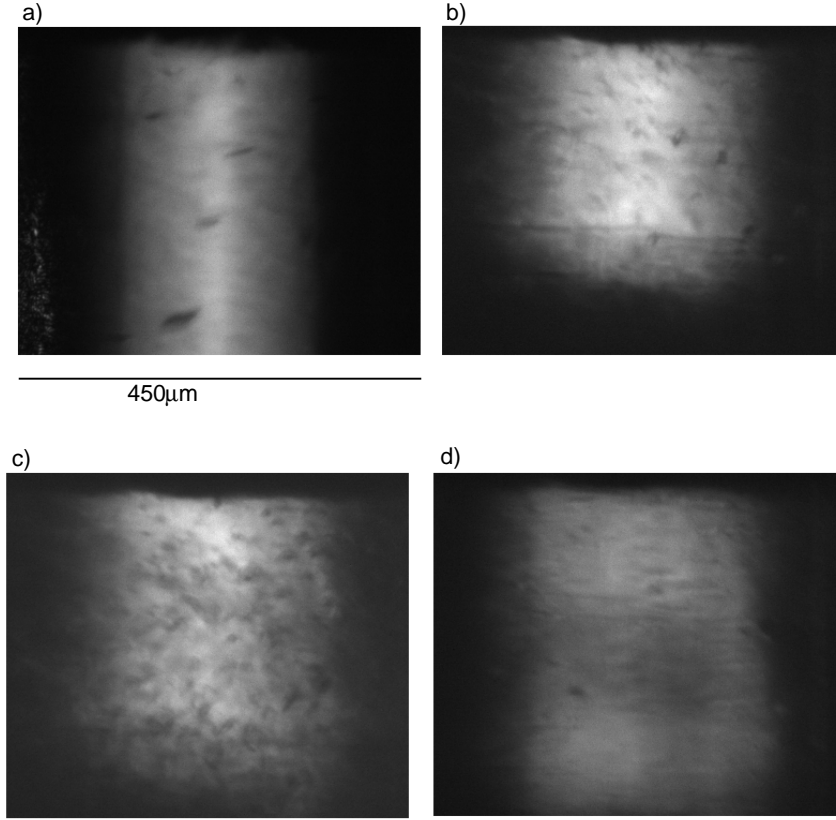


Figure 4.2: D-T at several temperatures. The bubble size distribution is time and temperature dependent. The temperature and ages for each image are: a) 30 hours at 19.5 K, b) 5 days at 18 K, c) Sample in b) 12 hours after temperature was reduced to 17 K, d) 24 hours at 13 K.

shows that the ^3He reaches the 18.3 K D-T vapor density in 21 days. The increased gas density decreases the target yield by roughly $1/3$ according to figure 112 of Lindl.¹ This rapid buildup of ^3He severely constrains the target handling time.

Not all the ^3He diffuses into the vapor region. Instead, the concentration of ^3He in the solid increases in time until it reaches a steady state, at which point the ^3He is going into the vapor at the same rate as it is being generated in the solid. The concentration and time to reach steady state are calculated using the 1-D diffusion equation. The boundary conditions used set the concentration and atom flux to zero at the solid – vapor and D-T – capsule interface respectively. The steady state concentration for a layer of thickness l

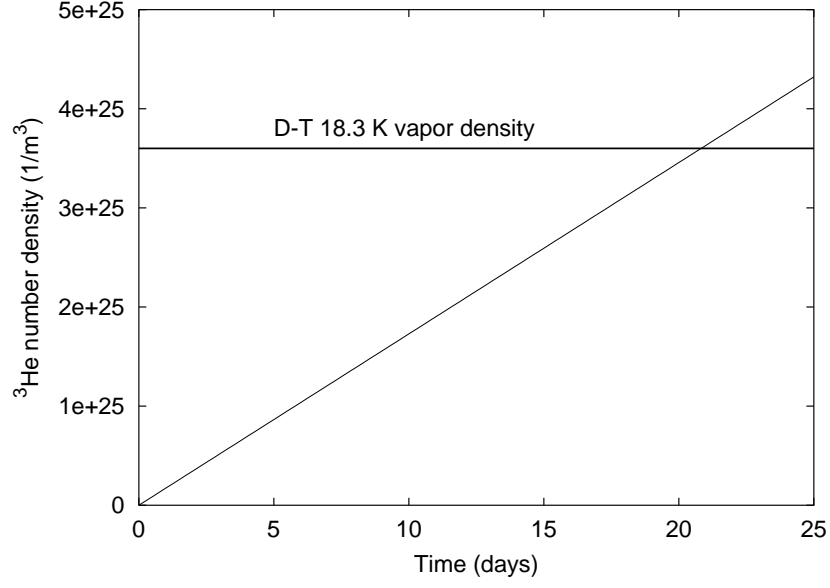


Figure 4.3: Number density of ^3He in the vapor region of a NIF scale target. The required D-T vapor density for NIF is shown for comparison.

is

$$\nu_{\text{He}} = \frac{G}{2D} (l^2 - x^2), \quad (4.2)$$

where $G = 1.78 \times 10^{-9} \text{ 1/s}$ is the ^3He generation rate from the beta decay, D is the diffusion coefficient, and x is the distance from the solid-plastic interface. Steady state is approached with a time constant

$$\tau_{\text{ss}} = \frac{4l^2}{\pi^2 D}. \quad (4.3)$$

Storing the targets at low temperatures reduces the ^3He in the vapor region by decreasing the ^3He diffusivity. However, as more ^3He is trapped in the solid the number of bubbles increases. Figure 4.4 shows a $170 \text{ }\mu\text{m}$ thick D-T layer that was cooled from 19.7 K to 17.8 K over 17 hours. This figure shows several micron sized features in D-T that grew in with time and are not seen in pure D_2 . These features are similar to those seen in the early work by Hoffer and Foreman⁶ who interpreted them as ^3He bubbles.

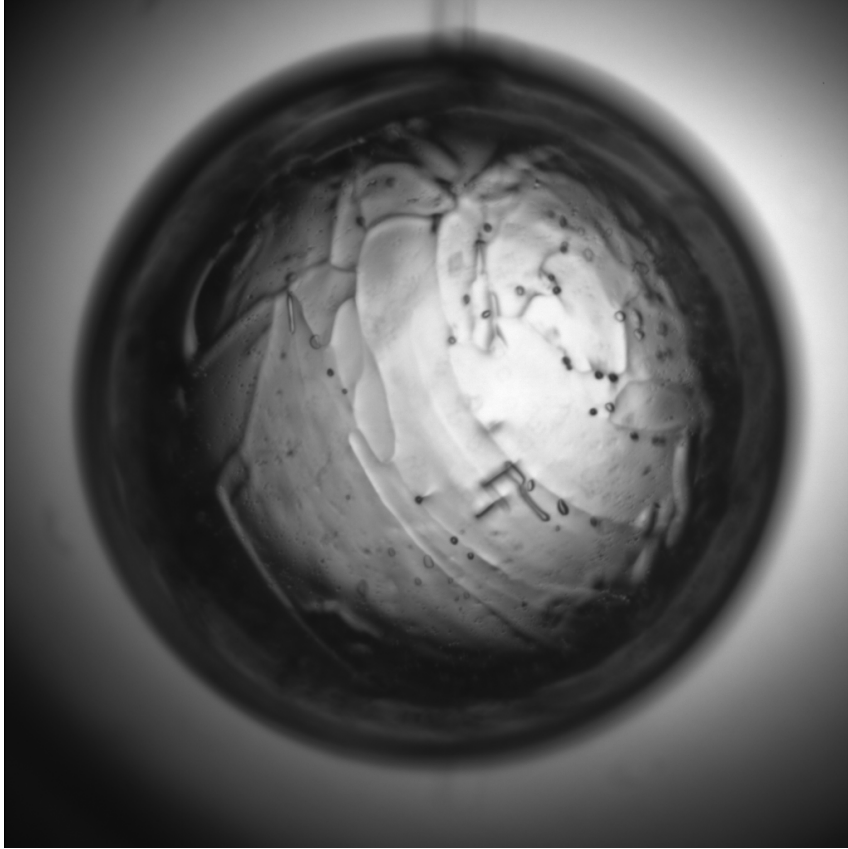


Figure 4.4: A 2 mm diameter shell with 170 μm thick D-T layer slow cooled to 17.8 K over 17 hours. ^3He bubbles are visible as dark spots throughout the layer.

The bubbles seed Rayleigh-Taylor instabilities during implosion similar to the D-T-vapor interface roughness. No modeling exists to predict the target performance of D-T with bubbles, but it is reasonable to expect the roughly the same effect as a surface perturbation of the same scale. We are most concerned with a bubble distribution that seeds perturbations for modes 100 and lower, or 60 μm and larger length scales in 2 mm diameter shells.¹

The ^3He buildup and bubble formation must be understood to ensure optimum target performance. The experiments presented in this chapter measure bubble growth rates and mobility as the D-T ages at several temperatures. The experiments cover several different ranges of sizes and properties of the ^3He bubbles. Dynamic light scattering probes

bubbles smaller than the wavelength of light while microscopy tracks bubbles larger than a few microns. The bubble diffusion, growth rate, and response to a thermal gradient are reported here.

4.2 Gas bubbles in solids

The buildup of gas atoms in a solid is not unique to tritium and has been studied extensively in conjunction with the gas atom implantation in fusion reactor walls as well as fission products in fissile materials.^{76–83} While these systems serve as a starting point for understanding ^3He bubbles in D-T, the high D-T vapor pressure, low surface energy and temperature compared to previous studies of gases in solids extends the parameter space of experimental conditions and theory. Further, typical experimental investigations use TEM and SEM to observe bubbles in the solid and are often limited to either studying bubbles near the surface or sectioning after specified irradiation and anneal sequences. TEM and SEM are not easily applicable to solid hydrogen. Instead, the hydrogens are optically clear allowing studies of bubbles with light scattering and optical microscopy experiments. Previous theoretical treatments of gas bubbles in solids are reviewed with the differences for ^3He in D-T pointed out.

4.2.1 Static properties: Pressure and size

Helium atoms produced in a solid migrate within the solid by vacancy and interstitial diffusion^{84,85} and can interact with other atoms to form small, stable clusters of atoms and vacancies. Clusters take on gas phase properties as they grow and more vacancies are incorporated to reduce the stress in the surrounding solid.⁷⁶ There is no stress in the solid when the bubble is in equilibrium and the internal bubble pressure is balanced by

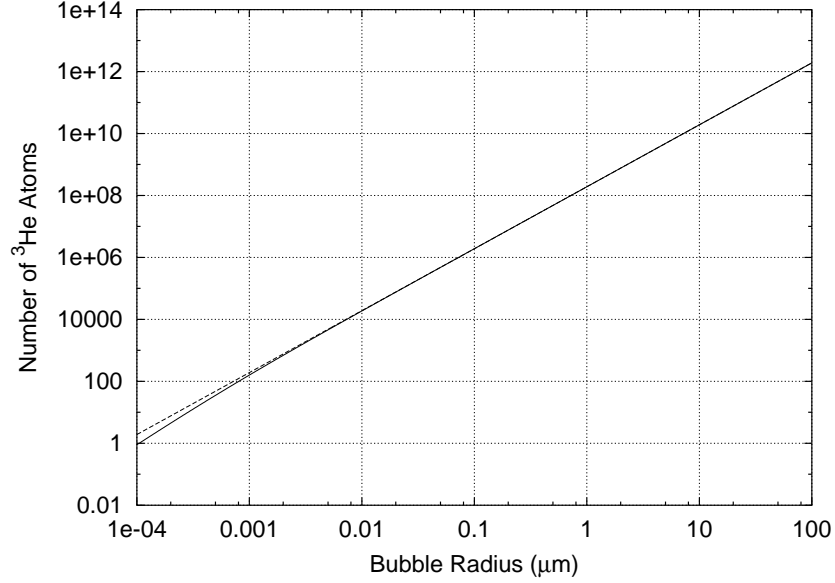


Figure 4.5: Calculated number of ^3He atoms in a bubble as a function of bubble radius using the Laplace pressure. Both the viral expansion (solid) and ideal gas (dashed) equation of state are shown. There is little difference for bubbles larger than 1 nm.

the surface energy^{77,86} according to the well known Laplace pressure,²⁶

$$\Delta P = \frac{2\gamma}{r}. \quad (4.4)$$

ΔP is the excess pressure within a bubble of radius r in a material with surface energy γ . The excess pressure decreases with increasing size and goes to zero for a flat interface. Typical metals have a surface energy 100 times larger than D-T at their respective melting temperatures^{78,87} and hence a much larger excess bubble pressure for a given bubble size.⁸⁶ Furthermore, most metal systems of interest are studied at room temperature and above. Whereas the small helium bubbles are at very high pressures in metals,⁸⁶ helium bubbles in D-T are much lower in pressure. The gas equation of state determines the number of atoms in a bubble. The simplest case is the ideal gas law, which gives

$$PV = \frac{2\gamma}{r}V = nkT,$$

which for a spherical bubble reduces to

$$n = \frac{8\pi\gamma r^2}{3kT}. \quad (4.5)$$

The ideal gas law is valid for nearly all possible bubble sizes in D-T. Figure 4.5 shows the the number of atoms in a bubble determined using both the ideal gas law (dashed line) and the viral expansion (solid line), $PV = n(1 + Bn/V)kT$, where $B = -5.3 \times 10^{-30} \text{ m}^3/\text{molecule}$ for helium.⁸⁸ There is little difference until the bubble radius is less than 1 nm, much lower than the ≈ 50 nm for bubbles in metals.^{76,89} Hence, the ideal gas law is a very good approximation for all bubble sizes in D-T.

A sufficient supply of vacancies is required for the bubble to remain in equilibrium as additional gas atoms are added.^{76,89} An estimate of the number of vacancies arriving at the bubble surface is obtained using the equilibrium vacancy concentration in D-T,⁹⁰

$$n_{\text{eq}} = N \exp\left(-\frac{E_v}{kT}\right). \quad (4.6)$$

n_{eq} is the equilibrium number of vacancies in a solid with N molecules and vacancy formation energy E_v . The D-T E_v of⁹¹ 137 K gives a vacancy concentration of 7×10^{-4} at 19 K. The rate vacancies arrive at a bubble surface, and hence the time it takes a bubble to reach equilibrium, is obtained using Chandrasekhar's equation for the number of diffusion particles crossing an absorbing screen,⁹²

$$4\pi DR\nu \left(1 + \frac{R}{(\pi Dt)^{1/2}}\right), \quad (4.7)$$

where R is the bubble radius, ν is the vacancy concentration, and D is the vacancy diffusion coefficient. The D-T vacancy diffusion constant of⁹¹ $\approx 10^{-13} \text{ m}^2/\text{s}$ gives the vacancy arrival rate at a 10 nm bubble of 2.5×10^5 vacancies per second. Compared with the 2×10^4 helium atoms in a 10 nm bubbles, the bubbles should quickly reach equilibrium.

The vapor pressure of metals^{78,87} and uranium dioxide^{93,94} are much lower than D-T, even at a significant fraction of their respective melting temperatures. The metal or ceramic vapor make up an insignificant fraction of the gas bubble in those experiments. However, for helium bubbles in D-T, the D-T vapor must be taken into consideration. The total pressure in a bubble is the sum of the D-T vapor pressure, P_{vap} , and the Laplace pressure,

$$P_T = \frac{2\gamma}{r} + P_{\text{vap}}. \quad (4.8)$$

Using the triple point D-T vapor pressure of 2.01×10^4 Pa and $\gamma = 6.0 \times 10^{-3}$ J/m² from section 3.6.2, the D-T vapor pressure is greater than the Laplace pressure for bubbles larger than 0.6 μm . This is in striking contrast to previous investigations of bubbles in metals in which the solid pressure is negligible over all bubble sizes of interest. The high D-T vapor pressure gives rise to different bubble migration mechanisms than most metals.

4.2.2 Dynamic bubble properties

Several groups have reported Brownian motion of bubbles in solids.^{78,82,95} Brownian motion of gas bubbles in solids is different from the traditional particle suspended in a fluid. In the latter case, a solid particle moves in response to the stochastic collisions with the surrounding liquid molecules. The fluid molecules are much smaller than the suspended particle, hence the fluid particles have a higher velocity at a given temperature. Because the stochastic force has a mean value of zero, the mean particle displacement is also zero, but as characteristic of Langevin processes, the mean square displacement is non-zero.⁹⁶

Bubbles in a solid are not subject to an external Langevin force, nor do the gas atoms colliding with the bubble significantly move the strongly bound solid molecules at the surface. Instead, the solid molecules at the bubble surface are subject to continuous

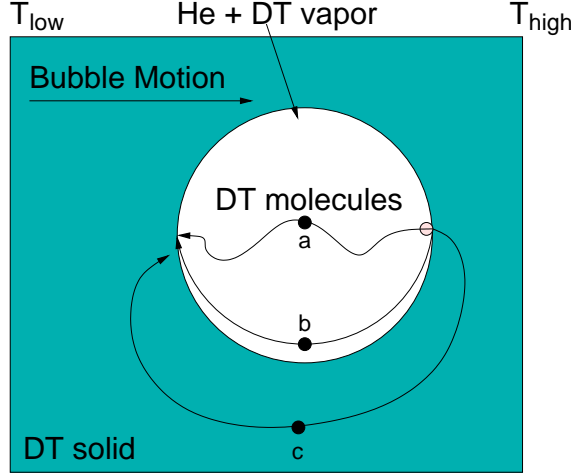


Figure 4.6: Possible migration mechanisms for bubbles in solids after Nichols⁷⁷ and Goodhew.⁷⁸ The bubble center of mass moves when D-T molecules travel by vapor transport (a), surface diffusion (b), or volume transport (c).

evaporation and re-condensation as well as surface diffusion. These random processes are the source of the stochastic motion of the bubble. When one molecule leaves the surface and moves to another part of the bubble, the bubble center of mass moves proportional to the ratio of the molecular volume to bubble volume. This is similar to the fluid example where the motion of the large particle is much smaller than the surrounding fluid. Even though there are no collisions as in the case of fluids, the resulting bubble motion still takes on Brownian characteristics.

Three transport mechanisms are available to atoms at the surface of a bubble, volume transport, surface diffusion, and vapor transport.^{77,78,81,93} These three mechanisms are shown schematically in figure 4.6. Vapor transport is the result of evaporation of molecules from one point on the bubble surface and subsequent condensation at another surface site. Volume transport occurs when solid molecules leave the bubble surface and move, either interstitially or by vacancy transport, into the bulk material. Finally, the diffusion of molecules along the bubble surface also results in net motion of the bubble. In each case the bubble moves opposite the direction of the molecules. Properties of the solid and

bubble, such as temperature, bubble size, and surface energy determine which of the three processes dominates the bubble diffusion. Additionally, if the bubble surface is faceted then the diffusion may be further limited by the slow nucleation rate.

In addition to Brownian motion, bubbles move in response to an external driving force, such as stress fields^{77,97} and thermal gradients.^{77,93} The self-heating of D-T makes the thermal migration, known as the Soret effect for single atoms,^{98–100} particularly relevant. The velocity of a bubble can be related to the driving force F and the diffusion constant D using the Nernst-Einstein equation,^{77,78,96}

$$V = \frac{DF}{kT}. \quad (4.9)$$

Nichols⁷⁷ has derived the expressions for both the bubble diffusion constant and the velocity in response to a thermal gradient for the three transport mechanisms. For surface diffusion (SD),

$$D_{\text{SD}}^b = \frac{3D_s\lambda\Omega}{2\pi r^4} \quad (4.10)$$

$$V_{\text{SD}}^b = \frac{2D_s\nu_s\Omega Q_s^*}{kT^2r} \frac{3K}{2K + K'} \nabla T_\infty, \quad (4.11)$$

for vapor transport (VT),

$$D_{\text{vt}}^b = \frac{3}{4\pi} \frac{D_g\Omega^2\alpha_v P_{\text{vap}}}{kTr^3} \quad (4.12)$$

$$V_{\text{vt}}^b = \frac{D_g\Omega\alpha_v P_{\text{vap}}\Delta H_s}{k^2T^3} \frac{3K}{2K + K'} \nabla T_\infty. \quad (4.13)$$

and for volume transport (VOL),

$$D_{\text{vol}}^b = \frac{3D_{\text{vol}}\Omega}{4\pi r^3} \quad (4.14)$$

$$V_{\text{vol}} = \frac{2D_{\text{vol}}Q_{\text{vol}}^*}{kT^2} \frac{(K - K')}{2K + K'} \nabla T_\infty. \quad (4.15)$$

The binary gas diffusion coefficient, D_g is given by kinetic theory,

$$D_g = \frac{2kT}{3P_T\sigma} \sqrt{\frac{2kT}{\pi} \left(\frac{1}{m_1} + \frac{1}{m_2} \right)}, \quad (4.16)$$

Table 4.1: Variable definitions and values

Variable	Definition	Value for D-T	Ref.
D_s	Surface diffusion coefficient		
D_g	Gas diffusion coefficient	equation 4.16	
D_{vol}	Volume self-diffusion coefficient	$3.4 \times 10^{-5} \exp(-372/T) \text{ m}^2/\text{s}$	91
λ	Surface jump distance		
σ	Gas collision cross section		
α_v	Gas non-ideality parameter	≈ 1	
Ω	Molecular volume of the solid atoms	$3.3 \times 10^{-29} \text{ m}^3$	7
ν_s	Surface number density		
P_{vap}	Solid vapor pressure	equation 4.17	7
P_T	Total bubble pressure	equation 4.8	
K	Solid thermal conductivity	$0.3 \text{ W}/(\text{m}\cdot\text{K})$	101
K'	Bubble thermal conductivity		
∇T_∞	Thermal gradient in the solid		
Q_s^*	Surface diffusion heat of transport	$\approx 1500 \text{ J/mol}$	Estimated
ΔH_s	Solid heat of sublimation	1580 J/mol	7
Q_{vol}^*	Volume diffusion heat of transport		

where m_1 and m_2 are the masses of the two species.

The definitions and values for these equations are listed in table 4.1. The parameters for the vapor and volume transport cases are either known or can be accurately estimated, whereas the surface diffusion coefficient and heat of transport are unknown for D-T.

It is often stated in the literature that the velocity of bubbles moving by vapor transport is inversely proportional to the bubble radius. Although this is applicable to all previously studied cases, it is true only when P_T is dominated by the Laplace pressure. In D-T, by contrast, the total bubble pressure is given by equation 4.8 and bubbles larger than a few microns are dominated by P_{vap} , as shown earlier. There is no size dependence in equation 4.13, hence the bubble velocity becomes independent of size for bubbles large enough to be observable with an optical microscope. Further, in addition to the explicit temperature dependence of equations 4.13, 4.15, and 4.16, there is an implicit temperature dependence in the equilibrium vapor pressure. The D-T vapor pressure at temperature T

is given by the three constant formula,⁷

$$P_{\text{vap}} = \exp \left(2.2389 \ln(T) - \frac{150.34}{T} + 10.831 \right) \text{ Pa.} \quad (4.17)$$

4.2.3 Diffusion calculations

Bubble diffusion and thermal migration rates can be calculated for vapor transport, volume transport, and surface diffusion to determine which mechanism dominates the bubble motion. The relevant quantities for surface diffusion are currently unknown for ^3He in D-T. Comparison with the other two diffusion mechanisms is performed in the section 4.9.1 based on experimentally measured parameters. Since nearly all variables for vapor and volume transport have either been measured or can be estimated accurately, these two diffusion mechanisms are compared here.

The collision cross section σ is πd^2 for molecules of size d . This will be on the order of the nearest neighbor distance in the solid, 0.36 nm. Using the values in table 4.1,

$$D_{\text{vol}}^b = 2.68 \times 10^{-34} \frac{\exp(-372\text{K}/T)}{r^3} \text{ m}^5/\text{s}, \quad (4.18)$$

$$D_{\text{vt}}^b = 6.06 \times 10^{-27} \sqrt{kT} \left(\frac{P_{\text{vap}}}{P_T r^3} \right) \text{ m}^4 \text{ kg}^{\frac{1}{2}}. \quad (4.19)$$

In the limit of small bubbles or low temperature, where the surface energy term dominates the total pressure, the bubble diffusion has a r^{-2} dependence for the vapor transport case. When the bubble pressure is dominated by the D-T vapor pressure the diffusion changes to r^{-3} .

The diffusivities at 19 K are plotted as a function of size in figure 4.7. The vapor transport mechanism dominates for all bubble sizes at 19 K. In both cases bubbles larger than 1 μm diffuse extremely slowly. The bubble diffusion constants are plotted vs temperature for a 10 nm bubble in figure 4.8. Again vapor transport is much faster than the

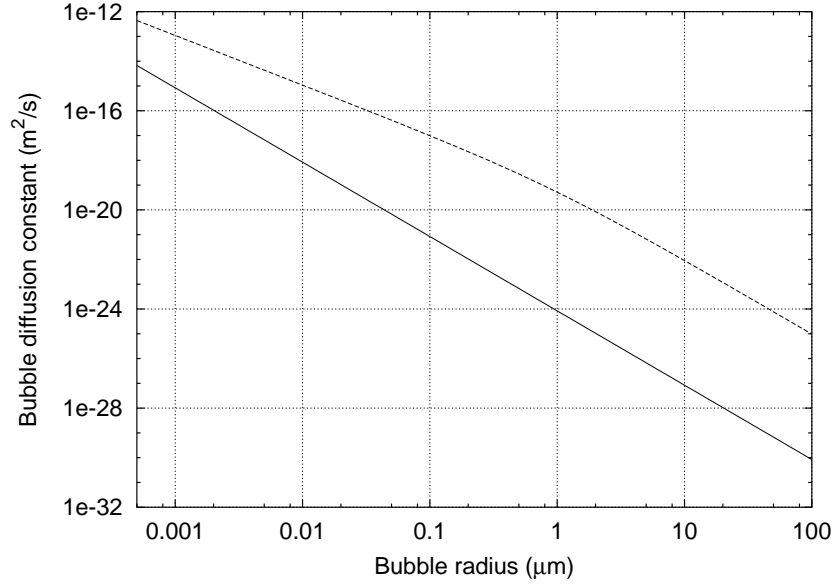


Figure 4.7: Calculated bubble diffusion constants vs radius at 19 K for volume (solid) and vapor (dashed) transport.

volume transport mechanism. The diffusivity only drops by a factor of 100 between 19 K and 13 K for vapor transport, compared to 10 000 for volume transport over the same range.

4.2.4 Thermal migration

The calculated diffusion coefficients indicate bubbles larger than about 10 nm diffuse very slowly through the layer at all temperatures, taking months to move completely through a 100 μm thick D-T layer. As previously stated, the D-T self heating creates a thermal gradient in the layer. Equations 4.13 and 4.15 allow us to calculate the expected bubble velocity in a thermal gradient. The bubble thermal conductivity will be neglected compared to the solid, giving an upper estimate on the bubble velocity. Similarly, Q_{vol}^* is not known, but should be on the order of half the heat of sublimation.^{93,102} Making the

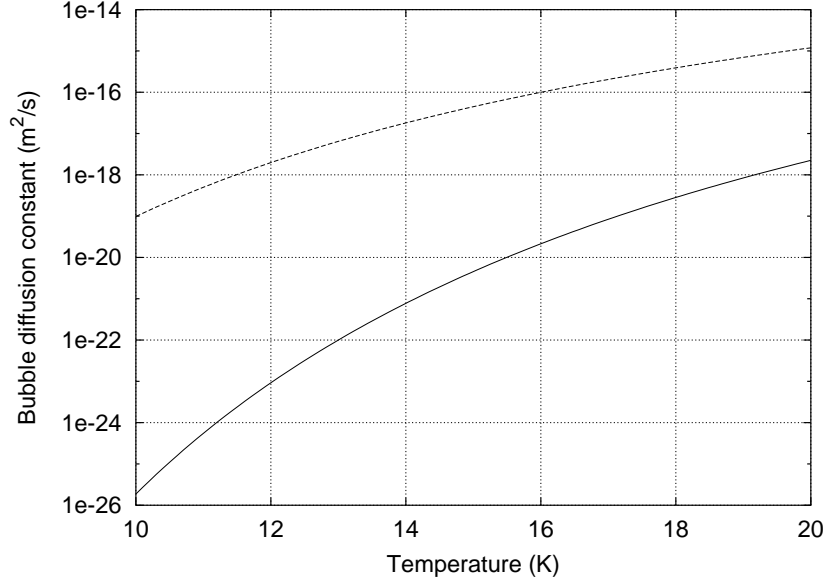


Figure 4.8: Calculated bubble diffusion constant vs temperature for a 10 nm bubble migrating via volume (solid) and vapor (dashed) transport.

appropriate substitution,

$$V_{\text{Vol}} = 3.4 \times 10^{-5} \frac{\exp(-372\text{K}/T) Q_{\text{vol}}^*}{kT^2} \nabla T_{\infty}, \quad (4.20)$$

$$V_{\text{vt}} = \frac{\Omega P_{\text{vap}} \Delta H_v}{kT^2 P_T \sigma} \sqrt{\frac{2kT}{\pi} \left(\frac{1}{m_1} + \frac{1}{m_2} \right)} \nabla T_{\infty}. \quad (4.21)$$

The velocities at 19 K are plotted in figure 4.9 as a function of bubble size, where 8 K/m has been used for ∇T_{∞} , the value halfway in a 100 μm thick D-T layer. The volume mechanism is independent of size, but the vapor transport, through the Laplace pressure, includes a size dependence. Thermal migration occurs much faster by vapor transport than volume transport for all sizes. Only at very low temperatures and very small bubble sizes will the vapor transport be slower. The thermal migration velocity is shown vs temperature for a 1 μm bubble transported by both mechanisms. Bubbles greater than 0.5 μm move rapidly and should traverse most of the layer in about 5 hours.

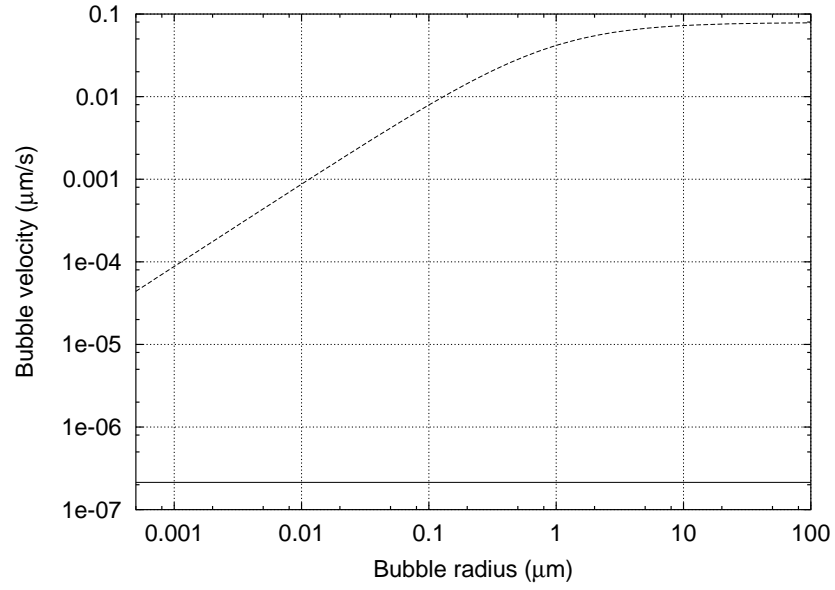


Figure 4.9: Thermal migration velocity of bubbles at 19 K traveling by volume transport (solid) and vapor transport (dashed) in a thermal gradient in the middle of a 100 μm thick D-T layer.

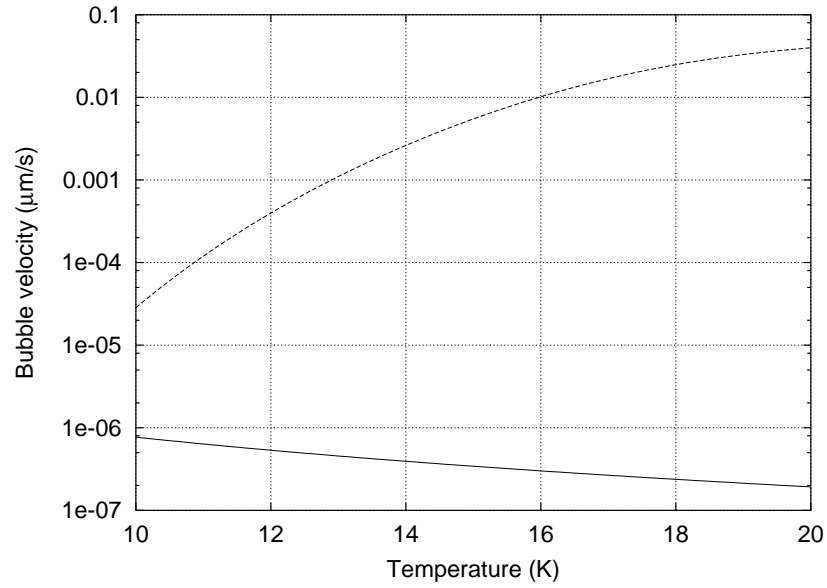


Figure 4.10: Thermal migration velocity a 1 μm bubble in a thermal gradient in the middle of a 100 μm thick D-T layer traveling by volume transport (solid) and vapor transport (dashed).

4.3 Bubble growth

Bubble growth has been modeled for surface diffusion controlled migration⁸¹ and more general conditions⁷⁸ based on Chandrasekhar's colloidal collision rate model.⁹² The model calculates the probability for two particles traveling by Brownian motion to collide per unit time. The probability for a particle undergoing Brownian motion to move a distance x in time t is given by

$$w(x, t) = \frac{1}{2(\pi Dt)^{1/2}} \exp\left(-\frac{x^2}{4Dt}\right), \quad (4.22)$$

where D is the particle diffusion coefficient. The probability of a collision is the probability for two particles to be at the same position at the same time. Using the statistical independence of the particle motion,

$$\begin{aligned} w_{1,2}(x_c, t) &= w(x_c - x_2, t)w(x_c - x_1, t) \\ &= \frac{1}{4\pi Dt} \exp\left(-\frac{(x_c - x_2)^2 + (x_c - x_1)^2}{4Dt}\right), \end{aligned} \quad (4.23)$$

where x_c is the collision point of two particles initially at x_1 and x_2 . The total probability for a collision after time t is obtained by integrating over all possible x_c ,

$$w^c(t) = \frac{1}{4\pi Dt} \int dx_c \exp\left(-\frac{(x_c - x_1)^2 + (x_c - x_2)^2}{4Dt}\right). \quad (4.24)$$

Integration gives

$$w^c(t) = \frac{1}{\sqrt{8\pi Dt}} \exp\left(-\frac{(x_1 - x_2)^2}{8Dt}\right), \quad (4.25)$$

which is simply the Brownian probability distribution with the distance between the two particles and twice their diffusion coefficient. The more general case where the particles may have different diffusion coefficients is easy to derive and yields

$$w^c(t) = \frac{1}{\sqrt{4\pi t\sqrt{D_1 + D_2}}} \exp\left(-\frac{(x_1 - x_2)^2}{4(D_1 + D_2)t}\right), \quad (4.26)$$

simply the diffusion probability with the sum of the two diffusion constants. The number of diffusing particles crossing a surface area is given by the diffusion flux equation,

$$J = -D\nabla\nu \quad (4.27)$$

where ν is the concentration. A sphere of radius R absorbs particles at a rate given by equation 4.7.

The generalization to the rate of collisions between particles with differing concentrations, sizes, and diffusion constants is⁹²

$$\Delta\nu_{ij} = 4\pi D_{ij} R_{ij} \nu_i \nu_j \left(1 + \frac{R_{ij}}{(\pi D_{ij} t)^{1/2}} \right) \Delta t. \quad (4.28)$$

For Brownian motion D_{ij} is the sum of the two individual diffusion coefficients, R_{ij} is the interaction distance which is typically the sum of the individual radii $R_i + R_j$, and ν_i is the concentration of particles of size i . The second term in the parenthesis can be ignored when the bubble size is less than the mean displacements.

Analytical solutions for equation 4.28 are possible only for trivial cases. Instead, a number of numerical solutions have been reported^{78,81,103,104} for bubbles. Gruber and Goodhew do not consider the constant supply of new gas atoms nor the possible escape through the solid surface in their models, both necessary to correctly model the size distribution in D-T. The works by Preininger and Kaletta include the generation of new gas atoms, but only model bubble sizes up to 6 nm. They report a bimodal bubble size distribution for both surface and volume diffusion with a power law increase in the mean bubble size which depends on the bubble diffusion mechanism and the single atom production rate.

4.3.1 Single bubble growth

Whereas many experiments measure only bubble size distributions, the optically transparent D-T enables individual bubble growth rate measurements. Large bubbles observable with a microscope have a very small diffusion coefficient as shown earlier. The rate smaller bubble arrive at a large one is given by equation 4.7. Denoting, as before, a bubble of size R_i containing n_i atoms, the number of atoms incorporated into the larger bubble by absorbing all smaller bubbles is

$$\begin{aligned}
 \Delta n &= R \sum_i 4\pi D_i \nu_i n_i \left(1 + \frac{R}{(\pi D_i t)^{1/2}} \right) \Delta t \\
 &= \kappa \sqrt{n} \sum_i 4\pi D_i \nu_i n_i \left(1 + \frac{\kappa \sqrt{n}}{(\pi D_i t)^{1/2}} \right) \Delta t \\
 &= \left(4\pi \kappa \sqrt{n} \sum_i D_i \nu_i n_i + 4\pi \kappa^2 n \sum_i \frac{D_i \nu_i n_i}{(\pi D_i t)^{1/2}} \right) \Delta t,
 \end{aligned} \tag{4.29}$$

where the bubble radius is related to the number of gas atoms according to equation 4.5, and $\kappa = \sqrt{\frac{3kT}{8\pi\gamma}}$.

The growth rate of a bubble has both a linear and square root dependence on its current size. The large size of optically observable bubbles prohibits ignoring the $R/(\pi Dt)^{1/2}$ term. To make further progress requires knowing the time dependence of ν_i . The simple case, where ν_i is constant, gives

$$\Delta n = \left(C_1 \sqrt{n} + C_2 \frac{n}{\sqrt{t}} \right) \Delta t, \tag{4.30}$$

where $C_1 = 4\pi \kappa \sum D_i \nu_i n_i$ and $C_2 = 4\pi \kappa^2 \sum D_i \nu_i n_i / \sqrt{\pi D_i}$ are constant in time.

4.4 Dynamic Light Scattering

Light is scattered by bubbles because of the index of refraction change at the bubble – solid interface. Light scattered by ^3He bubbles in D-T contains both static and dynamic

information about the bubbles. Static information, such as the bubble size distribution and shape is obtained from the angular and polarization dependent intensity collected over a short time period.¹⁰⁵ Dynamic light scattering (DLS) uses the time dependent intensity variation of scattered light to obtain information about the underlying dynamical processes causing the intensity fluctuations. DLS is often employed to measure the diffusion and drift velocity of particles.

The region of the sample which is illuminated by the incident light source and imaged onto the detector is known as the scattering volume. Because the scattering particles move through the scattering volume, the local dielectric constant is dependent on both time and position. The deviations from the background medium value of ϵ_0 are given by $\delta\epsilon(\vec{r}, t) = \epsilon(\vec{r}, t) - \epsilon_0$ and lead to a time dependent intensity. Both the speed of the particles and the magnitude of the scattering vector set the time scale of the intensity fluctuations.

The intensity autocorrelation,

$$\begin{aligned} G^{(2)}(\tau) &= \langle I(t + \tau)I(t) \rangle \\ &= \frac{1}{T} \int_0^T I(t + \tau)I(t)dt, \end{aligned} \quad (4.31)$$

is used to determine the characteristic fluctuation time scale. At long delay time τ such that the intensity is uncorrelated,⁹⁶

$$\begin{aligned} G^{(2)}(\tau \rightarrow \infty) &= \langle I(t + \tau) \rangle \langle I(t) \rangle \\ &= \langle I \rangle^2, \end{aligned} \quad (4.32)$$

where $\langle I \rangle$ is the mean intensity. Similarly, for $\tau = 0$, $G^{(2)}$ is

$$G^{(2)}(0) = \langle I(t)^2 \rangle. \quad (4.33)$$

$G^{(2)}$ decays from its maximum $\langle I(t)^2 \rangle$ at $\tau = 0$ to $\langle I \rangle^2$ for very long times. The measured decay time of $G^{(2)}$ characterizes the statistical process.

The relationship between the statistical properties of the scattered light and the dynamics of the scattering particles has been modeled and is well understood for many different types of motion.^{106,107} In particular, dynamic light scattering is often applied to measure the diffusion constant, and using the Einstein-Stokes equation, mass, of molecules in solutions undergoing Brownian motion. The following example illustrates the important concepts required to employ dynamic light scattering to study diffusive motion.

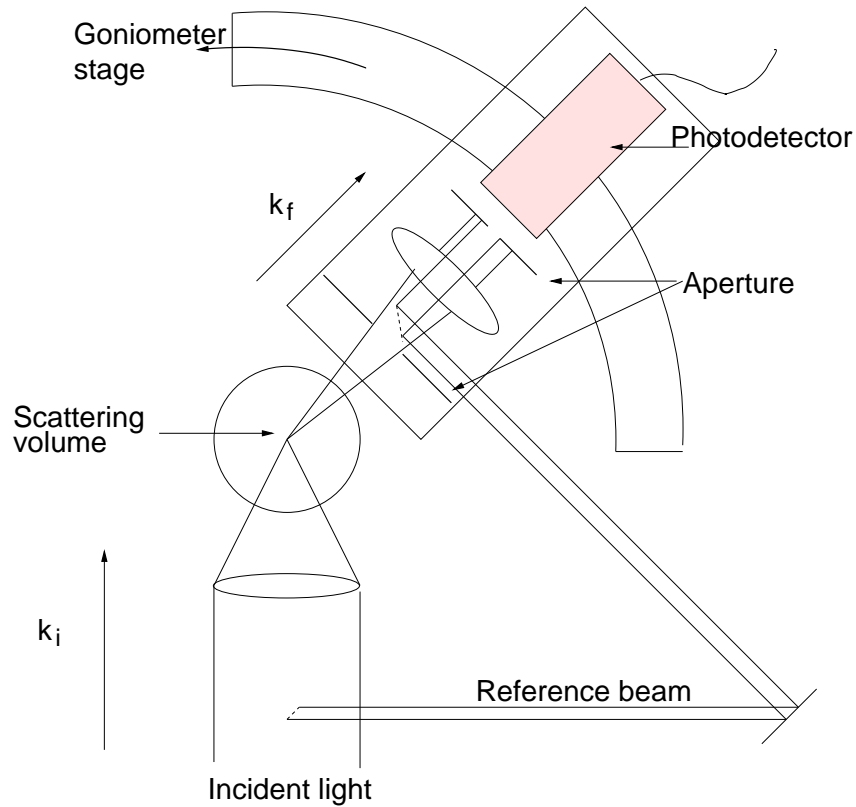


Figure 4.11: A general dynamic light scattering experiment. A sample is illuminated by the incident beam and the scattered light is collected on the photodetector. The goniometer enables analysis over a number of scattering vectors $\vec{k}_f - \vec{k}_i$, and the optional reference beam is used in the homodyne measurements.

A typical scattering experiment is shown in figure 4.11. A laser is focused onto a sample, and a photomultiplier detects the scattered light. The region of the sample il-

illuminated by the laser and imaged onto the photomultiplier tube selects the scattering volume. The total electric field at the detector is the summation over the field produced by each of the scattering particles. The incident electric field is assumed to be a plane wave with wave vector \vec{k}_i , and the direction from the scatterer to the detector is specified by \vec{k}_f . The scattering is elastic so that $|\vec{k}_i| = |\vec{k}_f|$. If the scattered electric field due to each of the N scatters is given by $E_k e^{i\phi_k(t)}$, the total scattered field at the detector is

$$E_s = \sum_{k=1}^N E_k e^{i\phi_k(t)}. \quad (4.34)$$

Here $\phi_k(t) = \vec{q} \cdot \vec{r}_k(t)$ is the time dependent phase for particle k , \vec{q} is the scattering vector, $\vec{q} = \vec{k}_f - \vec{k}_i$, and $\vec{r}_k(t)$ is the position of the scatterer with respect to the center of the sample.^{105,106,108} If there are no changes internal to the scattering particles, for instance, molecular rotations or chemical reactions, then the scattering amplitude due to one particular scatter, E_k , is time independent. The autocorrelation of the electric field at the detector is then given by

$$\begin{aligned} G^{(1)}(\tau) &= \langle E^*(0) E(\tau) \rangle = \left\langle \sum_k^N E_k^* e^{-i\phi_k(0)} \sum_j^N E_j e^{i\phi_j(\tau)} \right\rangle \\ &= \left\langle \sum_k^N |E_k|^2 e^{i(\phi_k(\tau) - \phi_k(0))} \right\rangle + \left\langle \sum_{k \neq j}^N E_k^* E_j e^{i(\phi_j(\tau) - \phi_k(0))} \right\rangle. \end{aligned} \quad (4.35)$$

Because the positions, and consequently ϕ_k , of different Brownian motion particles are uncorrelated, the second term in $G^{(1)}(\tau)$ vanishes. $G^{(1)}(\tau)$ is further simplified by assuming the particles are identical and obey the same diffusion law, then E_k is the same for each term in the summation, and $G^{(1)}(\tau)$ reduces to

$$\begin{aligned} G^{(1)}(\tau) &= N |E|^2 \langle e^{i(\phi(\tau) - \phi(0))} \rangle \\ &= N |E|^2 \langle e^{i\vec{q} \cdot (\vec{r}(\tau) - \vec{r}(0))} \rangle. \end{aligned} \quad (4.36)$$

The latter form makes it apparent that for a given detector position, which selects a particular \vec{q} , the measured autocorrelation is a function of the scattering particle displacement in a time τ . The interference pattern at the detector changes as the particles move relative to each other, shown in figure 4.12. In the limiting case where the particles are frozen in

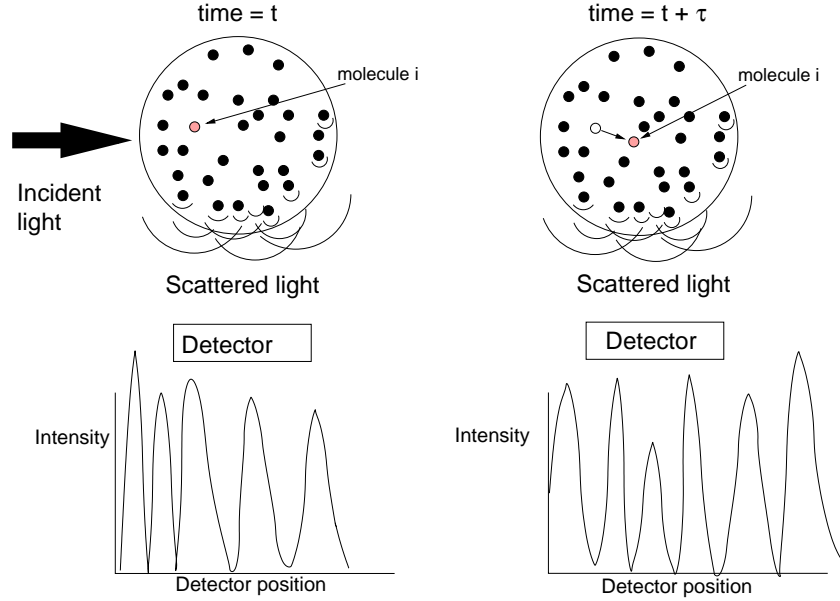


Figure 4.12: Light scattered to the detector by a collection of particles interferes at the detector. As the scattering particles move the interference pattern changes.

place, $\vec{r}(\tau) = \vec{r}(0) = r$, giving $G^{(1)}(\tau) = N|E|^2\langle 1 \rangle$, so the correlation and intensity are independent of time, as one would expect. The relation

$$\langle \exp(i\psi) \rangle = \exp\left(-\frac{\langle \psi^2 \rangle}{2}\right) \quad (4.37)$$

is used when ψ is a Gaussian distributed variable, as for Brownian motion. Then using $\langle (r(t) - r(0))^2 \rangle = 2Dt$, equation 4.36 reduces to

$$G^{(1)}(\tau) = N|E|^2 \exp(-q^2 D \tau), \quad (4.38)$$

where D is the diffusion constant.

It should to be noted that in almost all cases it is not the electric field which is measured, but rather the intensity of the light falling onto a detector. Instead of $G^{(1)}(\tau)$,

the intensity correlation of a signal from a photomultiplier is $G^{(2)}(\tau) = \langle I(\tau)I(0) \rangle$. It is straight forward to show that for Brownian motion, $G^{(1)}(\tau)$ is related to $G^{(2)}(\tau)$ by¹⁰⁶

$$G^{(2)}(\tau) = |I(0)|^2 \left(1 + \frac{|G^{(1)}(\tau)|^2}{|G^{(1)}(0)|^2} \right), \quad (4.39)$$

which is simply an exponential decay $e^{-2q^2 D \tau}$ plus a constant. Thus, the diffusion constant is obtained from the measured correlation decay time of the scattered light detected by a photomultiplier at a specified scattering angle. Figure 4.12 shows several interference peaks sampled by the detector. Limiting the detector area to one fringe reduces the average intensity but increases the fluctuation signal relative to the average.

4.4.1 Bubble scattering efficiency

As was shown in equation 4.5, the gas density is a function of both size and temperature. The scattering intensity is typically specified as r^6 for particles, but this is not necessarily true for the gas bubbles because the gas density is size dependent. Since bubbles dominated by D-T vapor pressure will be at a much lower density than the solid, only the small bubbles, obeying the Laplace pressure need be considered. The ideal gas law used with the Laplace pressure, equation 4.4, gives the bubble density as a function of size. The total electric susceptibility χ_b is the product of the gas density and the atomic polarizability α_{He} ,¹⁰⁹

$$\chi_b = \left(\frac{2\gamma}{rkT} \right) \left(\frac{\alpha_{\text{He}}}{\epsilon_0} \right) \quad (4.40)$$

The susceptibility of D-T solid is obtained from the index of refraction or from the atomic polarizability and the density. The scattering cross section of a particle in medium depends on the relative dielectric constants,¹⁰⁵

$$m^2 = \frac{1}{n_{DT}^2} \left(1 + \frac{2\gamma\alpha_{He}}{kTr\epsilon_0} \right). \quad (4.41)$$

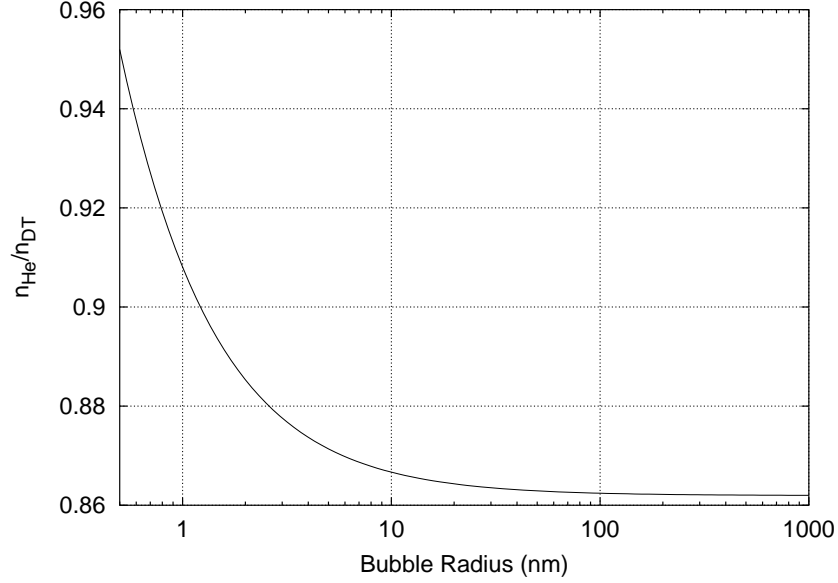


Figure 4.13: Calculated index of refraction ratio for a ^3He bubble in D-T using equation 4.41 with $T = 20$ K and $\alpha_{\text{He}} = 2.24 \times 10^{-41} \text{ C}^2\text{s}^2/\text{kg}$. The Laplace pressure and ideal gas law determine the ^3He density.

Figure 4.13 shows the relative dielectric constant as a function of bubble radius. There is little change for bubbles larger than a few nanometers. The scattering efficiency term,

$$\left(\frac{m^2 - 1}{m^2 + 2} r^3 \right)^2 \quad (4.42)$$

is plotted in figure 4.14 as a function of radius for D-T at the triple point temperature. This goes as r^6 to a very good approximation for all bubble sizes greater than 1 nm. Lowering the temperature reduces the bubble density and makes the approximation better.

4.5 Measuring correlation times

The diffusion constant is obtained from the correlation decay time as described above. A simple example was presented above, with only a single time constant and under ideal conditions. The D-T bubbles have a continuous size distribution, making the analysis more challenging. The relatively slow motion of the D-T bubbles further complicates the

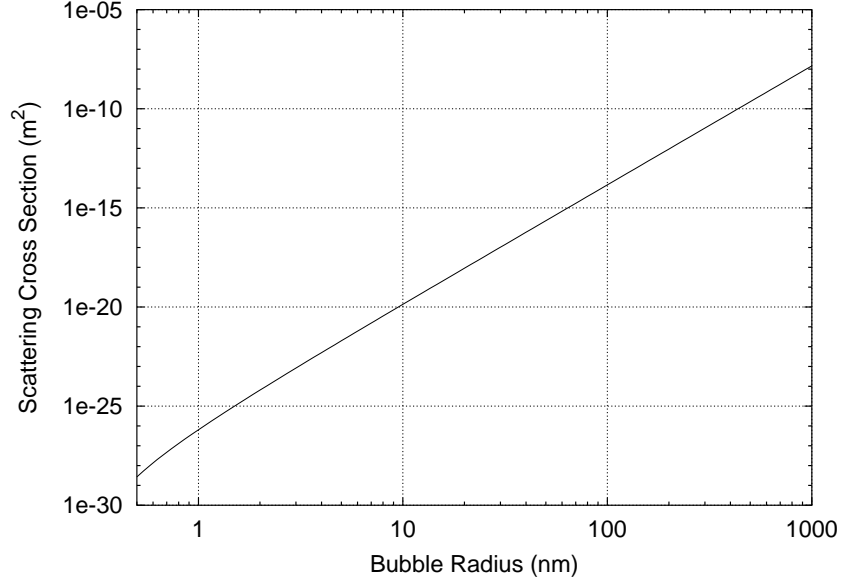


Figure 4.14: Scattering cross section for a ${}^3\text{He}$ in D-T using equation 4.42. The Laplace pressure and ideal gas law determine the ${}^3\text{He}$ density.

experiment. These issues are addressed in the following sections.

4.5.1 Polydisperse scattering

Polydisperse systems, where the scattering particles are not all of one size, have an intensity autocorrelation that is not a single exponential decay. Instead, the measured correlation will be a sum of exponentials, which can be written as^{110,111}

$$G^P(\tau) = \int_0^\infty f(\Gamma) \exp(-\Gamma\tau) d\Gamma, \quad (4.43)$$

where Γ is the inverse decay time, and $f(\Gamma)$ is the distribution of particles which have time constant $1/\Gamma$. $f(\Gamma)$ is not simply the number of particles, but instead must be weighted by the size of the scattering particles since larger particles scatter more light. Since equation 4.43 is a Laplace transform of $f(\Gamma)$ it is in principle possible to obtain the distribution by an inverse Laplace transform. However, because the data is sampled at discrete intervals the Laplace transform is not robust.^{110–113}

A moment analysis of the autocorrelation function is less subject to error but is unable to obtain the complete size distribution. Only a finite number of moments are calculated by fitting a polynomial to the data. The mean size and variance are obtained from the linear and quadratic polynomial coefficients.^{106,114–116} This is illustrated by expanding the exponential in equation 4.43 in a Taylor series to give

$$\begin{aligned} G^P(\tau) &= \int_0^\infty f(\Gamma) \left(1 - (\Gamma\tau) + \frac{1}{2} (\Gamma\tau)^2 + \dots \right) d\Gamma \\ &= \int_0^\infty f(\Gamma) d\Gamma - \tau \int_0^\infty \Gamma f(\Gamma) d\Gamma + \frac{1}{2} \tau^2 \int_0^\infty \Gamma^2 f(\Gamma) d\Gamma + \dots \end{aligned} \quad (4.44)$$

If $f(\Gamma)$ is properly normalized then

$$\begin{aligned} 1 &= \int_0^\infty f(\Gamma) d\Gamma \\ \langle \Gamma \rangle &= \int_0^\infty \Gamma f(\Gamma) d\Gamma \\ \langle \Gamma^2 \rangle &= \int_0^\infty \Gamma^2 f(\Gamma) d\Gamma \end{aligned} \quad (4.45)$$

Hence, the coefficients of a polynomial fit of the correlation function in τ are directly related to the mean and variance of the size distribution.

A note on the polynomial fitting is in order. Fitting a low order polynomial over too large a range introduces truncation errors. For example, to obtain the variance only the first and second moment are needed. However, as shown in figure 4.15, when the exponential has decayed to the $1/e$ value the second order polynomial deviates from the exponential by 35%. Because of this, the data analysis using second order polynomial fitting was applied only to less than 60% of the $1/e$ time.

Fitting a double exponential, $a_1 \exp(-t/\tau_1) + a_2 \exp(-t/\tau_2)$, to a polydisperse system often seems to be the obvious choice. However, the choice of parameters depends sensitively on the starting values in the fitting routine, subject to getting trapped in local

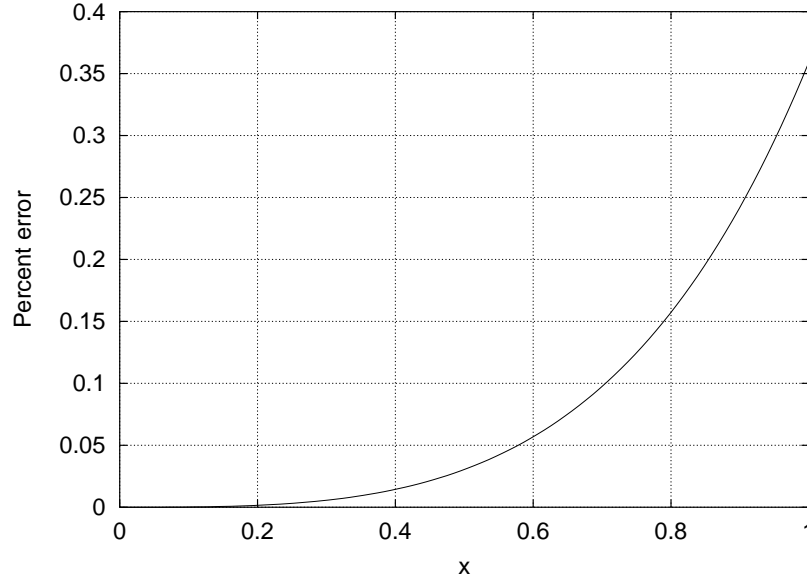


Figure 4.15: Error introduced by fitting $1 - x + x^2/2$ to $\exp(-x)$.

minima. Equally good fits are found with very different fitting parameters. Therefore, this model was not used in the data analysis.

4.5.2 Application to slow systems

Dynamic light scattering has found frequent application to biological and chemical fluid systems where the correlation times are typically much less than a second.^{106,117,118,107} A requirement easily overlooked is that the correlation needs to be performed over a time long compared to the decay time. It is only in the long time limit that Brownian motion take on the familiar $\langle x^2 \rangle = 2Dt$ form.⁹⁶ This requirement is trivial for systems with time constants of milliseconds, it takes only a few seconds to average many time constants. However, the ^3He bubbles in D-T move at a rate just on the edge of detection with DLS. It was necessary to record the intensity for hours in order to obtain a reasonable amount of data. However, even at this rate, it still proves to be too short at 13 K.

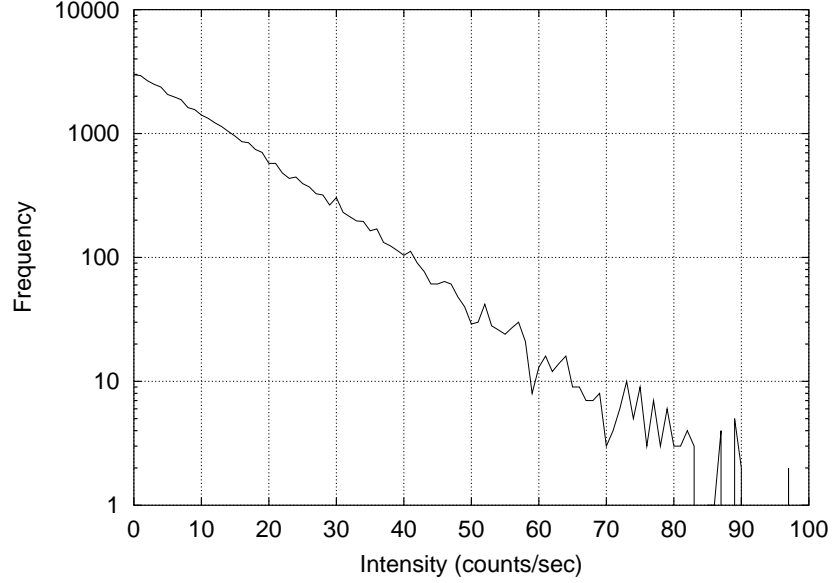


Figure 4.16: Measured frequency of intensity measurements for light scattered by Brownian motion particles. The data was simulated from 200 particles over 40 000 time steps.

The intensity distribution helps discriminate acceptable signals from those dominated by noise. Particles undergoing Brownian motion scatter light according to^{92,119}

$$P(I) = \frac{1}{\langle I \rangle} \exp \left(-\frac{I}{\langle I \rangle} \right), \quad (4.46)$$

where $P(I)$ is the probability for the intensity to take the value I and $\langle I \rangle$ is the mean intensity. By contrast, the intensity distribution is Gaussian for a coherent source.¹²⁰ The simulated light scattered by Brownian particles has the intensity distribution shown in figure 4.16. By contrast, distribution of the photomultiplier dark count rate is shown in figure 4.17. The probability distribution is clearly Gaussian with a mean count rate of 80 counts/sec.

4.5.3 Self-beating, homodyne and heterodyne

The light scattering discussion assumed that the light falling on the detector was “self-beating”, meaning that only the scattered light from the particles of interest was illumi-

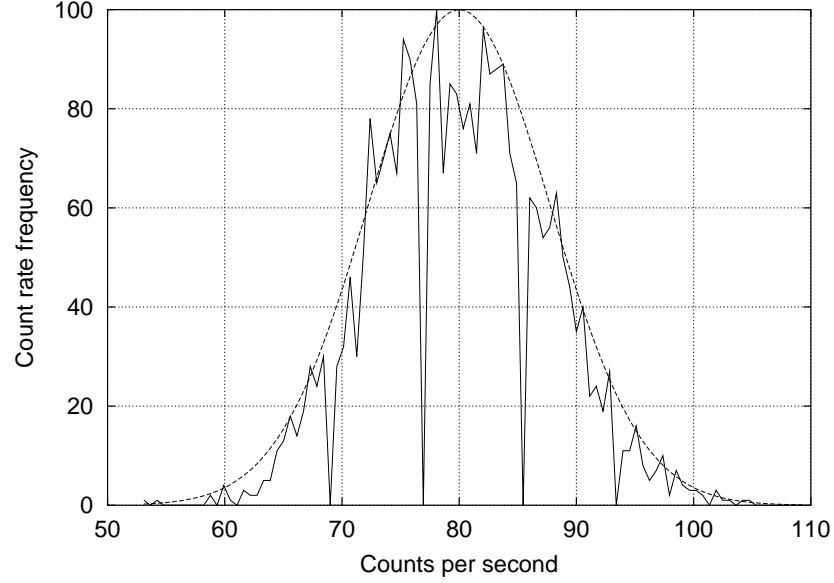


Figure 4.17: Count rate distribution for the photomultiplier dark counts (solid) and Gaussian distribution with a mean of 80 counts/second (dashed). The histogram was generated from 2700 data points.

nating the detector. In some circumstances it is desirable to operate in either a homodyne or heterodyne configuration. Homodyning is the result of mixing the scattered light with the unscattered portion of the incident beam, and heterodyning is mixing the scattered light with a different source. There is some confusion as to the correct application of the terms homodyne and heterodyne that needs be remembered when referencing various authors. Only the homodyne technique will be discussed here as the heterodyne was not applicable.

The advantage of the homodyne technique is its ability to obtain the phase information lost in the self-beating. The relative particle displacements are responsible for the interference at the detector in self-beating. However, in an ideal flow all particles move with the same velocity, and there is no relative displacement. By mixing the scattered light with a reference signal, termed the local oscillator (LO) in the literature, the intensity is modulated by the interference of the scattered and LO fields. The intensity correlation

function is

$$\begin{aligned}
G^{(2)}(\tau) &= \langle I^*(0)I(\tau) \rangle \\
&= \langle E_T(0)E_T^*(0)E_T^*(\tau)E_T(\tau) \rangle \\
&= \langle (E_s(0) + E_{LO}(0))(E_s(0) + E_{LO}(0))^*(E_s(\tau) + E_{LO}(\tau))^*(E_s(\tau) + E_{LO}(\tau)) \rangle,
\end{aligned}
\tag{4.47}$$

where E_s is the scattered electric field and E_{LO} is the local oscillator field. Whereas the phase information was lost in the self-beating case, the E_s and E_{LO} cross terms will create a beating signal.

Particles moving through a sample with a uniform drift velocity are the most relevant example of the homodyne technique. Known as laser Doppler velocimetry,^{106,107,121,122} the phase of the scattering particles changes in a regular way relative to the local oscillator. Because the particles are in constant motion the phase difference cycles continuously through the full 2π range with a $\vec{q} \cdot \vec{v}$ dependence.^{106,107} The measured correlation has an oscillatory behavior which depends on the scattering vector and the particle velocity.

Even though the light scattering experiment was set up for self-beating, light scattered by other surfaces may provide the local oscillator signal. Scattering from the cell walls was blocked by using apertures. The strongly scattering, low temperature samples could be providing a reference signal. By providing a constant background to the scattering volume it may be acting as a reference signal. This is not a problem when the bubbles are moving only by Brownian motion, however, an external driving force leads to a drift velocity. The optical cell was designed to have the thermal gradient vertical, which will not contribute to the homodyne signal. However, both the D-T and the glass will be heated by the laser and a gradient is likely in the horizontal plane.

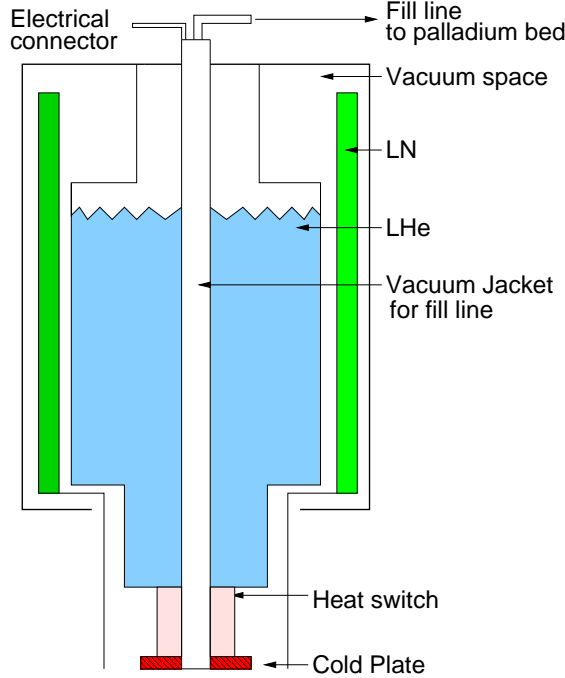


Figure 4.18: Cryostat dewar design.

4.6 Experimental design

The following experiments were undertaken to measure the ^3He bubble diffusion and response to a thermal gradient in D-T. Dynamic light scattering is used to measure bubbles less than the wavelength of light, and optical microscopy measures bubbles from several microns and up. Both the light scattering and the thermal gradient measurements were performed in the light scattering cell.

4.6.1 Cryostat

The main cryostat, shown in figure 4.18, was a Kadel KC192 50 liter liquid helium dewar with a five day typical hold time. A liquid nitrogen cooled radiation shield surrounded the liquid helium space to reduce helium consumption. A copper cold plate was connected to the liquid helium bath by a helium gas heat switch. The conductivity of the heat

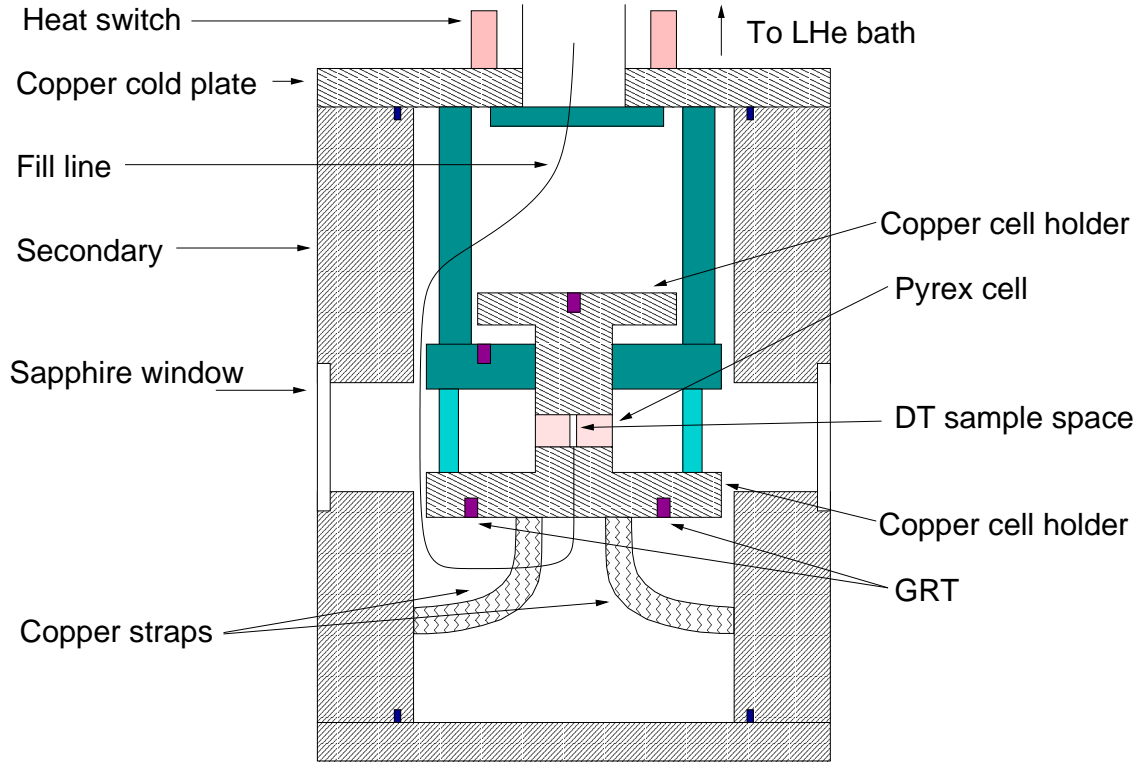


Figure 4.19: Cell Layout

switch was controlled by adjusting the amount of helium gas in the switch. The minimum operating temperature of the cold plate was 4.3 K. An aluminum secondary containment vessel was sealed with an indium gasket to the cold plate. If the D-T leaks out of the optical cell, the secondary container prevents release into the environment. The secondary also served as the main conduction path for the optical cell via a pair of copper straps between the two.

The optical cell design was chosen to minimize the D-T lost in the event of a cell leak and to conform to the optical layout of the existing vacuum chamber. The optical cell consisted of an 8 mm tall Pyrex octagonal cylinder sealed with indium gaskets to oxygen free hardened copper disks. The center of a 1 mm diameter bore along the cylinder axis with a 3 mm long copper plug inserted from the top and a 3 mm copper tube inserted from

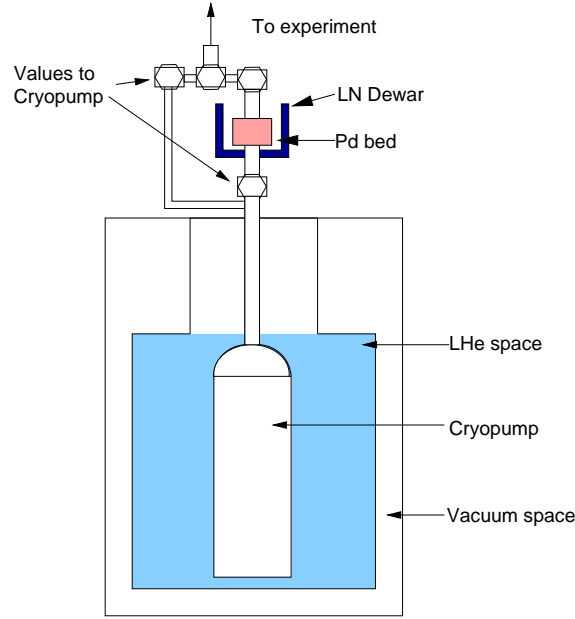


Figure 4.20: Diagram of palladium bed D-T storage system.

bottom was the D-T sample space. The sample space volume was $1.5 \times 10^{-9} \text{ m}^3$, capable of holding 2 Curies of solid D-T. The copper tube had a $150 \text{ } \mu\text{m}$ ID and allowed the sample volume to be filled with D-T. The low thermal conductivity Pyrex enabled control of the temperature difference across the cell with $130 \text{ } \Omega$, 40 gauge manganin wires wrapped around each of the the copper disks. Two Lakeshore germanium resistance thermometers (GRT) monitored the temperature of the lower copper disk, and one GRT was used on the upper copper disk. The GRT signal was used by Conductus temperature controllers to drive the heaters on the copper disks. The temperature on the copper disks was able to be controlled to less than $\pm 2 \text{ mK}$ over the span of several days.

4.6.2 Tritium handling system

The D-T storage and delivery system was constructed by EG&G Mound Applied Technologies and is shown in figure 4.20. The system consists of a palladium bed and charcoal

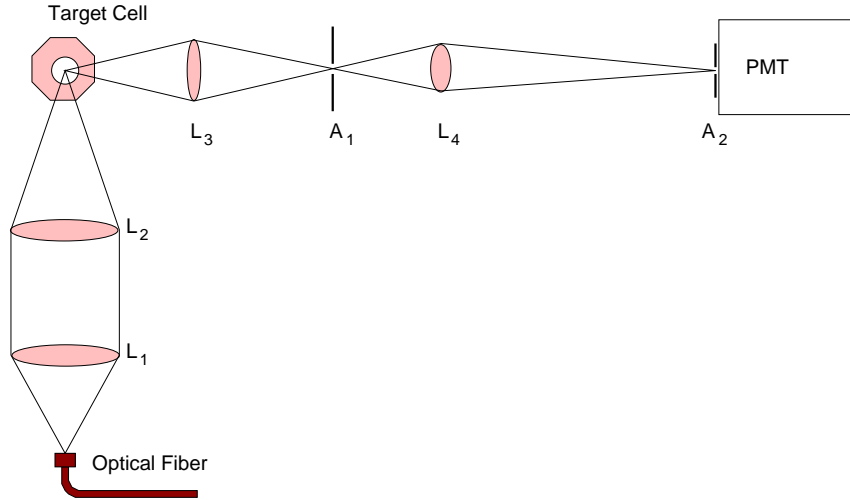


Figure 4.21: Diagram (not to scale) of the optical layout of the light scattering experiment. Lenses L_1 and L_2 focus laser light from the fiber into the optical cell. The scattered light is collected and magnified by lenses L_3 and L_4 onto the PMT. Aperture A_1 and A_2 limit the scattered light collected by the PMT.

cryopump. The D-T pressure over the bed is controlled by adjusting the bed temperature. Reducing the bed temperature absorbs more D-T onto the bed, and raising the temperature desorbs the D-T. The ^3He is not absorbed onto the bed and can be removed by the liquid helium cooled charcoal cryopump. Once the ^3He was removed the bed temperature was raised and the D-T gas admitted to the experimental cell cooled close to the D-T melting temperature. This procedure allowed us to start with a D-T sample that was free of ^3He .

4.6.3 Optical layout

The optical layout is shown in figure 4.21. The optical fiber was a Newport SPA single mode, polarization preserving 488 nm fiber which was coupled to a Spectra Physics Model 165 Argon ion laser. The laser polarization emitted at the fiber was perpendicular to the scattering plane. The injection optics, L_1 was a 160 mm fl, 40 mm diameter doublet, and L_2 was a 140 mm fl, 40 mm diameter doublet. The 8 mm thick fused silica, 1 mm

thick BK-7, and 2 mm thick sapphire windows on the vacuum chamber, radiation shield, and secondary container, respectively, between L_2 and the target cell are not shown. The collection optics consist of L_3 , a 65 mm fl, 30 mm diameter doublet and L_4 , a 38.1 mm fl, 35 mm diameter singlet. The collection system magnified the cell 10x and images onto the 100 μm diameter pinhole aperture A_2 mounted directly onto the Brookhaven Instruments BI-DS photomultiplier tube (PMT), operated at a bias of -1280 V. The detector collects light from 10 μm length scale of the D-T, much larger than the $1/q = 4.7 \times 10^{-8}$ m length scale which sets the correlation decay time. Aperture A_1 , placed at the image plane of L_3 , prevented stray scattered light from the cell edge from entering the PMT. The PMT output was input into the Brookhaven Instruments BI-9000 digital correlator. Both the intensity and the intensity autocorrelation were recorded for later analysis.

Not shown in 4.21 is the imaging system opposite the light scattering collection optics. A Questar QM-100 telescope images the optical cell onto a Photometrics 12 bit, 1024x1024 CCD camera and a Hamamatsu CCD video camera. The Photometrics images were transferred and stored on a computer while the Hamamatsu output was recorded on video tape.

4.7 Dynamic light scattering measurements

The following experiments use dynamic light scattering to measure the bubble diffusion. The D-T in the light scattering cell was grown from the vapor by initially freezing the D-T on one side of the cell and subsequently driving it to the other side by adjusting the thermal gradient across the cell. The solid grown this way was typically optically clear with few visible defects. The DLS signal was recorded as the sample aged at several different temperatures. The data from three temperatures, 19 K, 17.5 K, and 13 K is

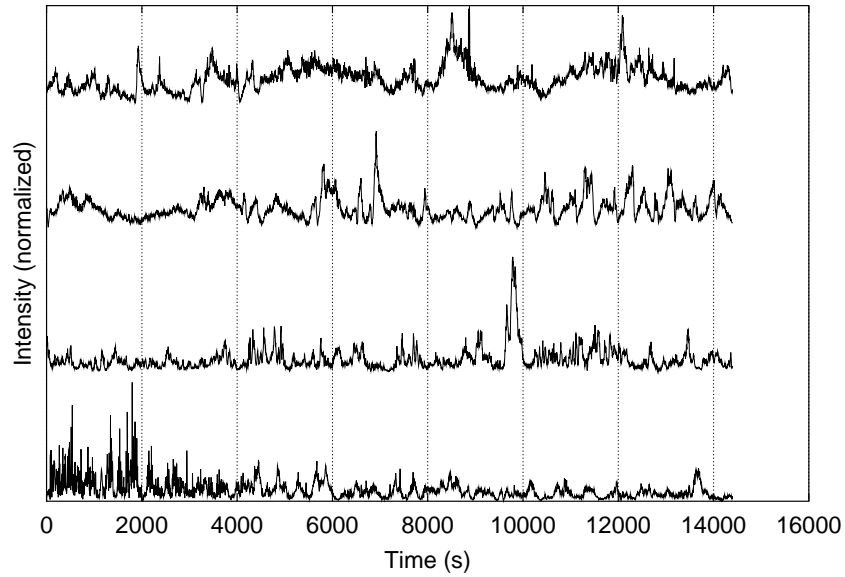


Figure 4.22: Measured scattered intensity vs time for D-T at 19.5 K. The records start at (bottom to top) 1.25 hours, 14.5 hours, 22 hours, and 31 hours after freezing the solid.

reported and shows the difference ^3He diffusivity as the temperature is reduced.

4.7.1 DLS at 19 K

The measured scattered light intensity for a sample at 19.5K is shown in figure 4.22. The intensities have been scaled to the same range for comparison. The intensity fluctuations gain more lower frequency modes as the sample ages. The large spikes at 9500 s in the second and 8200 s in the last record are likely due to a large scattering particle moving through the scattering volume and were removed before the autocorrelation was calculated. Figure 4.23 shows the autocorrelation for figure 4.22. The solid line is the autocorrelation for the first 4000 seconds and has a both an initial fast decay as well as a slower decay. The long dashed line is the correlation for the remainder of the first record. The short dash line corresponds to the second intensity record, with the spike at 9500 seconds removed. The intensity distribution for the first and last runs are shown in figure 4.24. The distribution decays exponentially as expected from equation 4.46, but a background signal is also

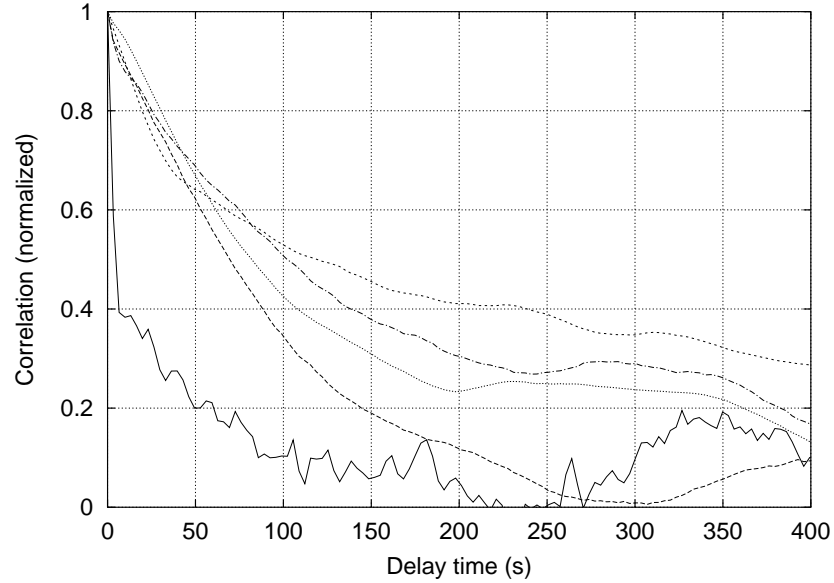


Figure 4.23: Measured intensity autocorrelation for D-T at 19.5 K for the intensities shown in figure 4.22. The solid line is the first 4000 seconds, the long dashes the remainder of curve a. The short dash, dotted, and dash-dotted lines correspond to the second, third and fourth curves, respectively.

evident.

The correlations are not simple exponential decays. Instead, both an oscillatory signal and multiple decay constants are evident. The last intensity plot clearly has a high frequency signal superimposed on a much lower mode. Multiple decays times are indicative of a distribution of bubble sizes. The data shows, as one would expect, that the mean bubble size is increasing as the sample ages. The measured time constants are plotted in figure 4.30, and the corresponding bubble diffusivities are shown in figure 4.31.

4.7.2 DLS at 17.5K

As the temperature is lowered, the bubble diffusivity decreases, as described in equations 4.10 and 4.12. The measured light intensity scattered by the D-T sample at 17.5 K for several times is shown in figure 4.25. The intensity fluctuation frequency shortly after freezing is comparable to the aged 19.5 K sample. Although high frequency modes

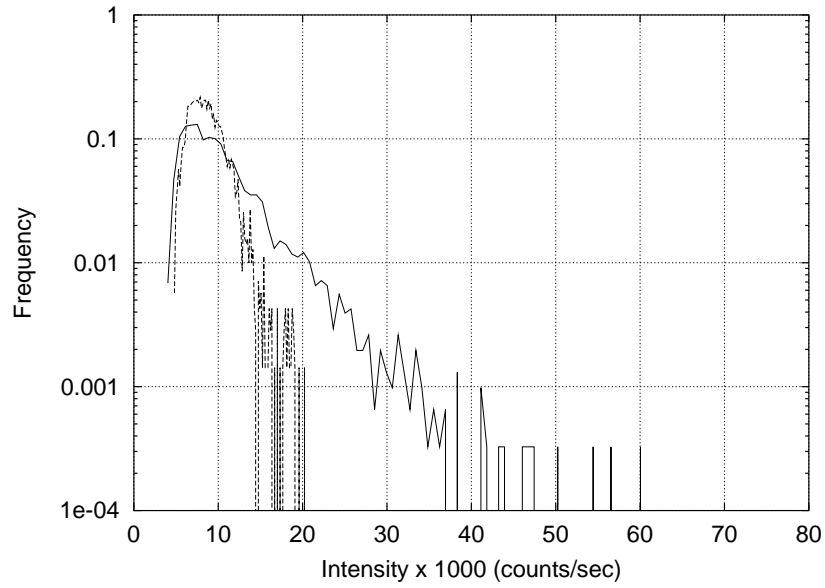


Figure 4.24: Measured intensity distribution for the first (solid) and last (dashed) traces in figure 4.22. The decay is exponential, however, background noise is present.

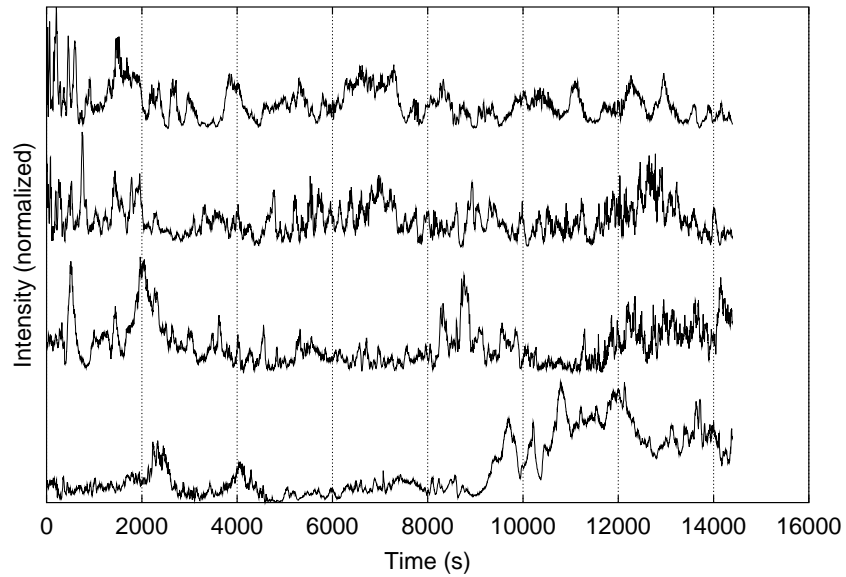


Figure 4.25: Measured intensity for D-T at 17.5K. The records start at (bottom to top) 2 hours, 6.5 hours, 11.3 hours, and 16.5 hours after the freezing.

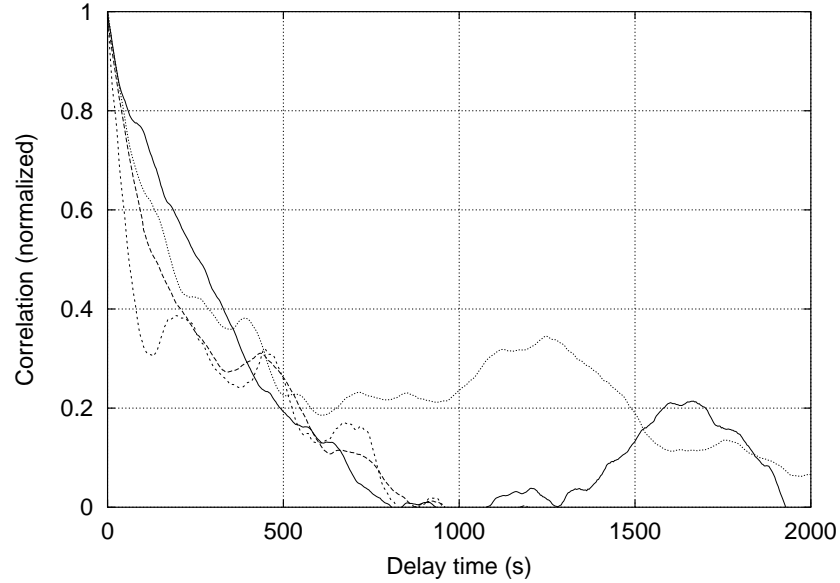


Figure 4.26: Measured intensity autocorrelation for D-T frozen at 17.5K, where the curves correspond to the intensities in figure 4.25

remain visible throughout the run, the low frequency components become more prominent with age. The autocorrelation functions, figure 4.26, have a quick initial decay and a subsequently slower decay. The autocorrelation was calculated up to 9000 seconds for the first curve to eliminate the broad feature late in the run.

4.7.3 DLS at 13 K

The intensity vs time is shown in figure 4.27 for D-T frozen at 13K. It is clear that the intensity fluctuation frequency is much lower than measured at 19 K and 17.5 K. Except for the second record, there is not a very large change in the fluctuation time constant over the length of observation. However, longer fluctuations cannot be discerned from these short plots. Comparison with both 19 K and 17.5 K samples shows that the time scale of fluctuations are much longer at 13 K than the higher temperatures. At the latest time the 13 K sample is completely dominated by a few low frequency modes, with little high frequency components present. This differs from both the 19 K and 17.5 K measurements.

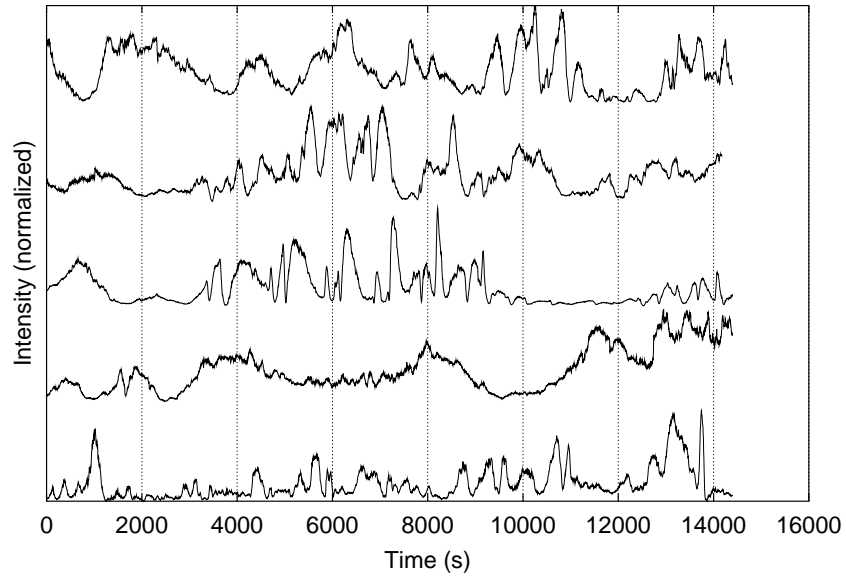


Figure 4.27: Measured intensity for D-T at 13 K. The records start at (bottom to top) 15 minutes, 4.5 hours, 8.5 hours, 21 hours and 45 hours after the D-T was frozen.

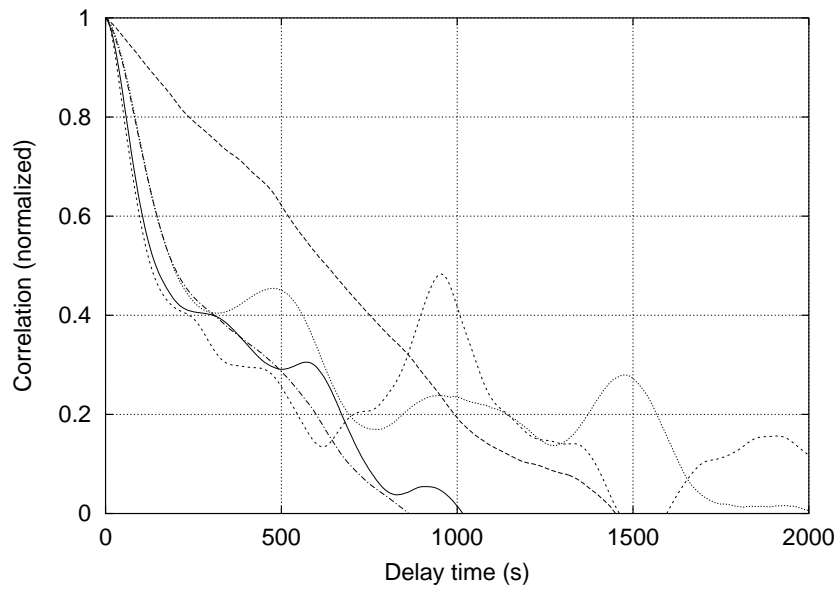


Figure 4.28: Measured intensity autocorrelation for D-T frozen at 13 K, where the curves correspond to the intensities in figure 4.27

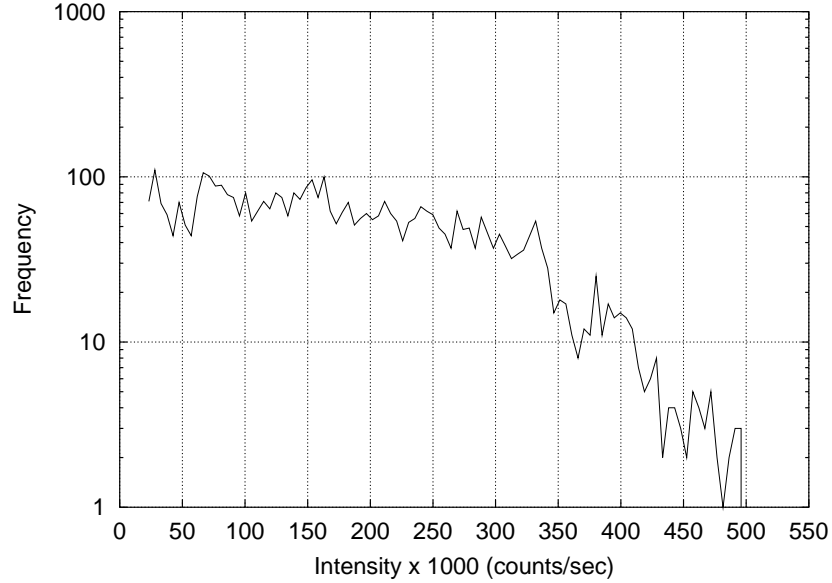


Figure 4.29: Histogram of the measured intensities for the last 13 K run shown in figure 4.27. The distribution does not have Poisson statistics.

The low temperature prevents the ^3He bubbles from diffusing through the lattice. As shown from theory in figure 4.8 for bubbles and experimentally by Gaines *et. al.* for molecules,⁹¹ the diffusion constant decreases by 2-3 orders of magnitude from 19.5 K to 13 K. The slower diffusion is the source of the reduced intensity fluctuation frequency observed at 13 K.

The autocorrelation of these intensities are shown in figure 4.28. The measured time constants are very likely to be misleading in this case. The intensity distribution shown in figure 4.29 is not Poissonian, hence the dynamics measured are not Gaussian for the time measured. Nevertheless, the best fit time constants and bubble diffusivities are included in figures 4.30 and 4.31 to allow comparison and are likely to be within an order of magnitude of the actual values.

The average bubble diffusion coefficient derived from the correlation times according to $D = 1/(2q^2\tau)$ are plotted in figure 4.31. Although there is much scatter in the data,

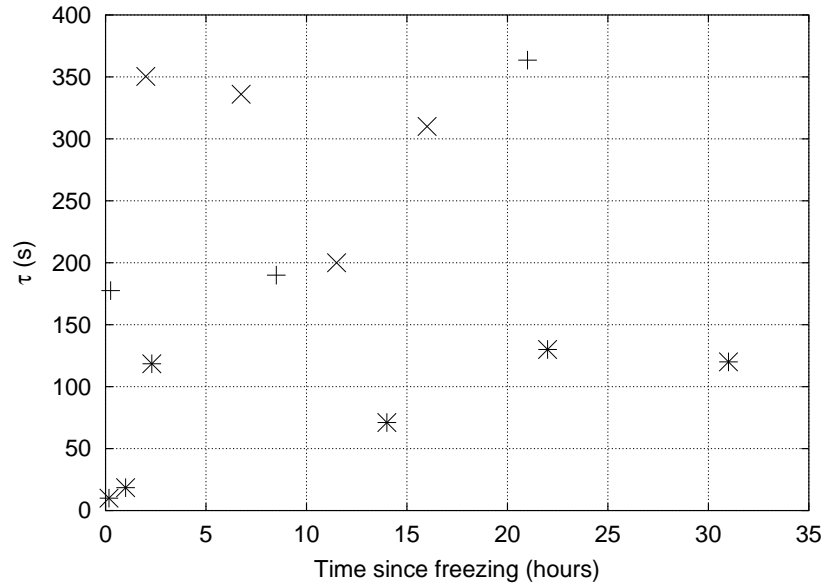


Figure 4.30: The correlation decay times for 19 K (*), 17.5 K (+), and 13 K (x) plotted as the sample ages.

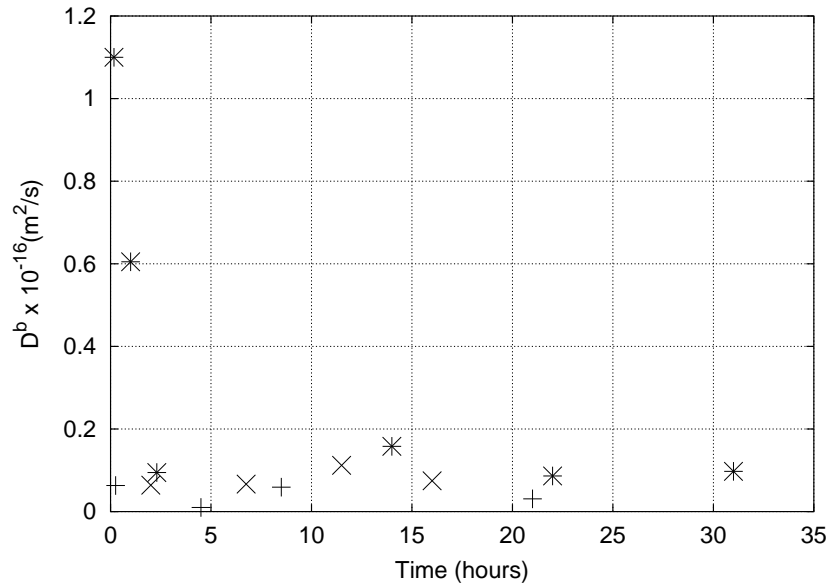


Figure 4.31: Measured diffusion constants for 19 K (*), 17.5 K (+), and 13 K (x) as the sample ages.

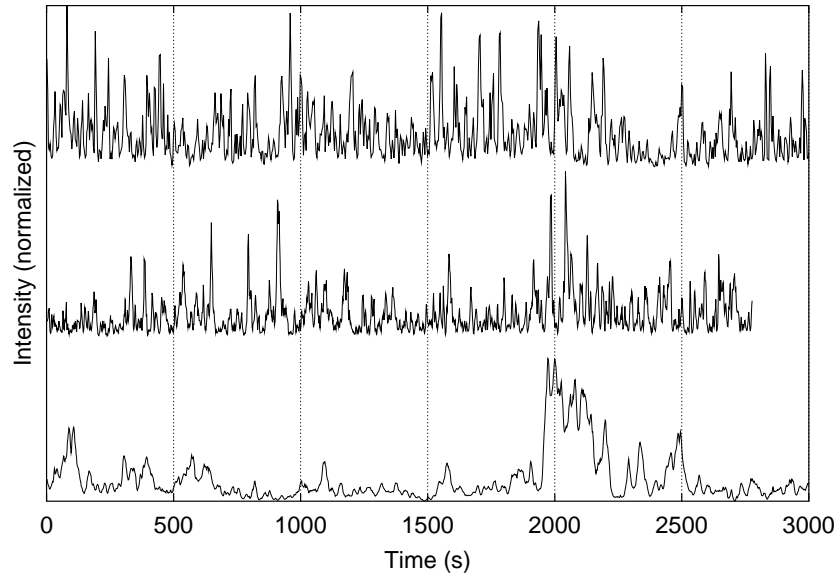


Figure 4.32: Measured scattered intensity at 13 K (bottom curve), shortly after heating the D-T to 18 K (middle curve), and further increasing to 19.5 K (top curve).

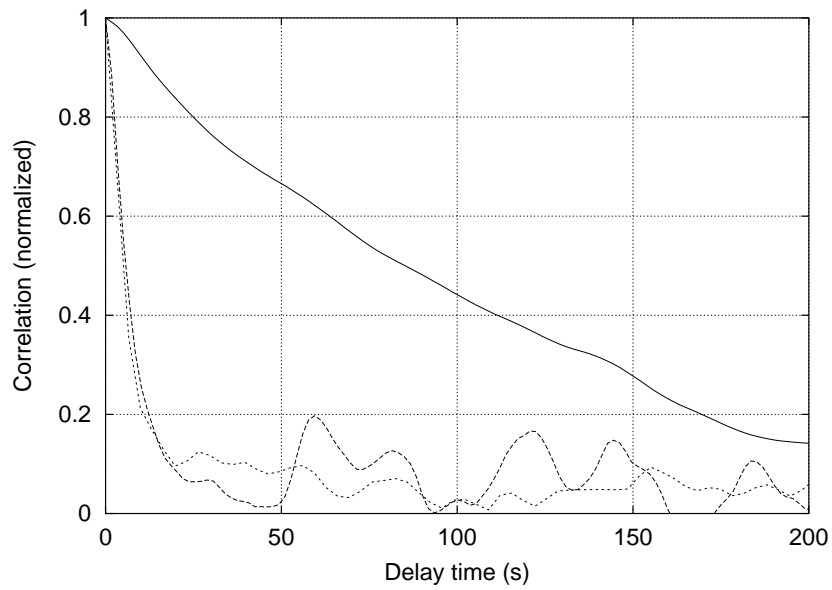


Figure 4.33: Measured intensity autocorrelation at 13 K (solid), 18 K (long dash) and 19.5 K (short dash) for the intensities shown in figure 4.32

the diffusion constants are consistent with the expected value for vapor transport of 50 nm sized bubbles. A rapid decrease in the bubble diffusivity at 19 K is observed, while the runs at lower temperature do not show a consistent increase. Because the bubble size distribution could not be measured in this configuration it is not possible to further compare and determine the accuracy of the model using only this data.

4.7.4 Temperature steps

The bubble diffusion constant depends on both the bubble size and temperature. To determine the temperature dependence at constant size, the D-T was first held at constant temperature for a long time, then quickly stepped to a higher or lower temperature. The first case, shown in figures 4.32 and 4.33, shows the intensity spectrum and autocorrelation of a sample initially at 13 K for 2.5 days, raised to 18 K, and then 19.5 K. The fluctuation time scale decreases upon warming. The measured diffusion constants are 9.2×10^{-18} m²/s, 1.0×10^{-16} m²/s, and 2.0×10^{-16} m²/s at 13 K, 18 K, and 19.5 K, respectively. The measured diffusion coefficient in this case compares well with the values shown in figure 4.31, shortly after freezing at 19.5 K. Assuming that the mean bubble size is not changing too quickly upon warming the sample, the diffusion constant change is in agreement with the expected change for vapor transport shown in figure 4.8. This also shows that the mean bubble size decreases with temperature.

Similarly, when the temperature is lowered, the intensity fluctuation frequency decreases. The intensity of a second sample is shown before and after the temperature was lowered from 17 K to 15 K in figure 4.34. The lower two curves were recorded at 17 K, while the upper two were recorded starting immediately after reducing the sample temperature to 15 K. The fluctuation time scale is clearly slower at 15 K and appears to remain

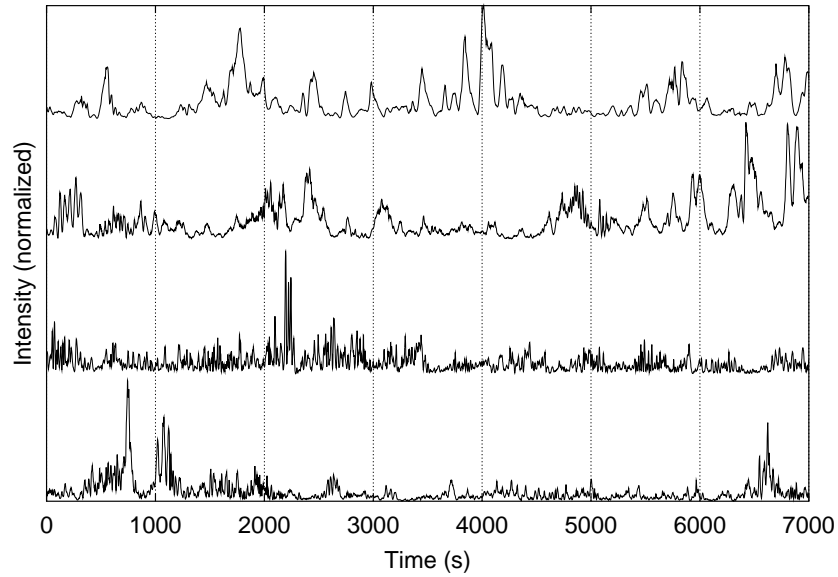


Figure 4.34: Measured scattered intensity at 17 K (lower two curves) and shortly after cooling the D-T to 15 K (upper two curves).

constant for the sampling time.

4.7.5 Scattering wave vector dependence

The correlation decay time depends on the scattering vector q as $\tau = 1/(2q^2D)$ for Brownian motion. Changing q provides a check to determine if the light scattering is due to Brownian motion. This measurement is traditionally performed by rotating the detector through a range of angles relative to the incident beam. The vacuum chamber design prevented measuring q as a function of angle. Instead, the scattering was measured after changing the input laser wavelength from 488 nm to a 830 nm laser diode. Figure 4.36 shows the increased time constant when using 830 nm light instead of 488 nm. The time constant could not be determined in this case because of the slow decay, however the intensity fluctuation frequency decreases going from 488 nm to 830 nm. This shows the intensity fluctuations are due to the diffusion of scatters in the sample and not, for instance, due to movement of the cryostat or cell which do not depend on the laser wavelength.

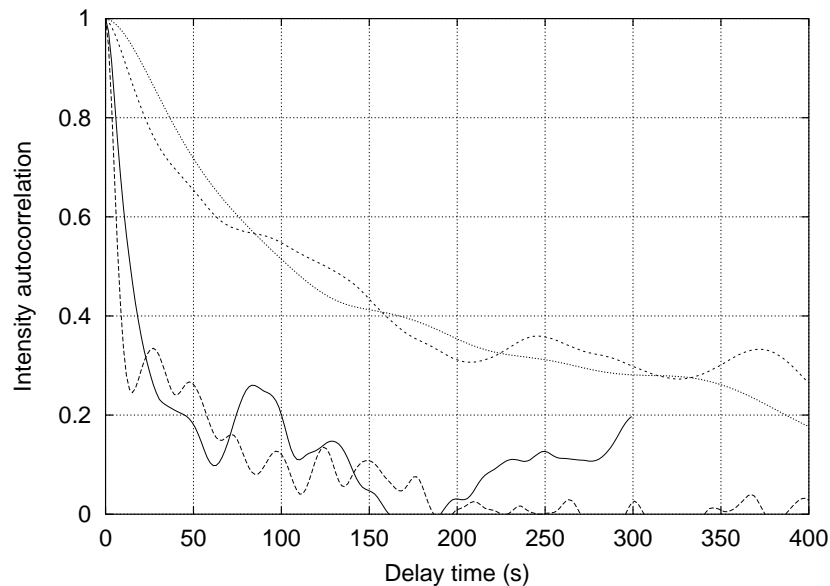


Figure 4.35: Measured intensity autocorrelation at 17 K (solid and dashed) and 15 K (short dash and dotted) for the intensities shown in figure 4.34

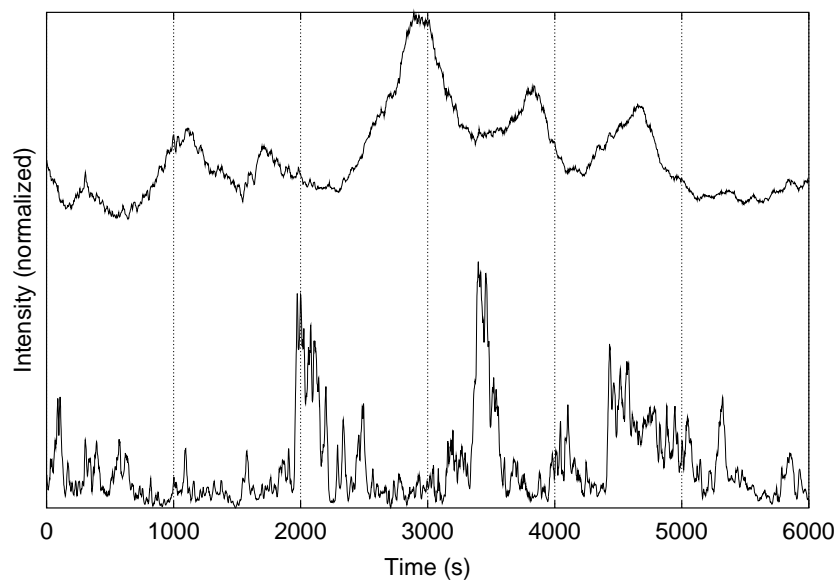


Figure 4.36: Measured intensity vs time using 488 nm (lower) and 830 nm (upper) light for D-T at 12 K.

4.8 Bubble growth and morphology

The growth rates of bubbles large enough to be observed with the optical microscope were measured for a number of bubbles. The sample cell in this case was 2 mm diameter, 30 μm wall plastic shell with a 250 μm layer of D-T. A few large bubbles were observed after the layer had been cooled at a rate of 1 mK/min to 18.4 K (figure 4.37).

The D-T was furthered cooled to 17.7 K and the subsequent bubble growth observed. A large number of small bubbles grew in the layer within a few hours, as seen in figures 4.38 and 4.39. The size of the bubbles was measured as a function of time and is shown in figure 4.41. The temperature was further lowered to 16.8 K and observed. Bubbles continue to grow at this temperature, and the size of selected bubbles are shown in figure 4.42.

The growth rate vs initial size is shown in figure 4.43. Although the data is scattered, especially for small bubbles, the area growth rate increases linearly with initial bubble area. From equations 4.5 and 4.30, the bubble area goes as $K_1\sqrt{A} + K_2A$. K_1 and K_2 cannot be evaluated without knowing the bubble size distribution, but for $> 10 \mu\text{m}$ bubbles the linear dependent term dominates the growth rate. This simple model shows the correct behavior

An 80 μm thick D-T layer with a history similar to the 250 μm thick layers is shown in figure 4.40. Very few bubbles are visible in the image, taken 14 hours after the temperature was decreased from 18.5 K to 17.7 K. The high diffusivity and thin layer enables single atoms and small bubbles to escape from the thin layers before large bubble can form. Neglecting bubble formation, the steady state atom concentration from equation 4.2 is reduced by a factor of 10 compared to the 250 μm layer. The bubble formation rate is difficult to predict without fully solving equation 4.28 but probably scales as ν^2 or faster.

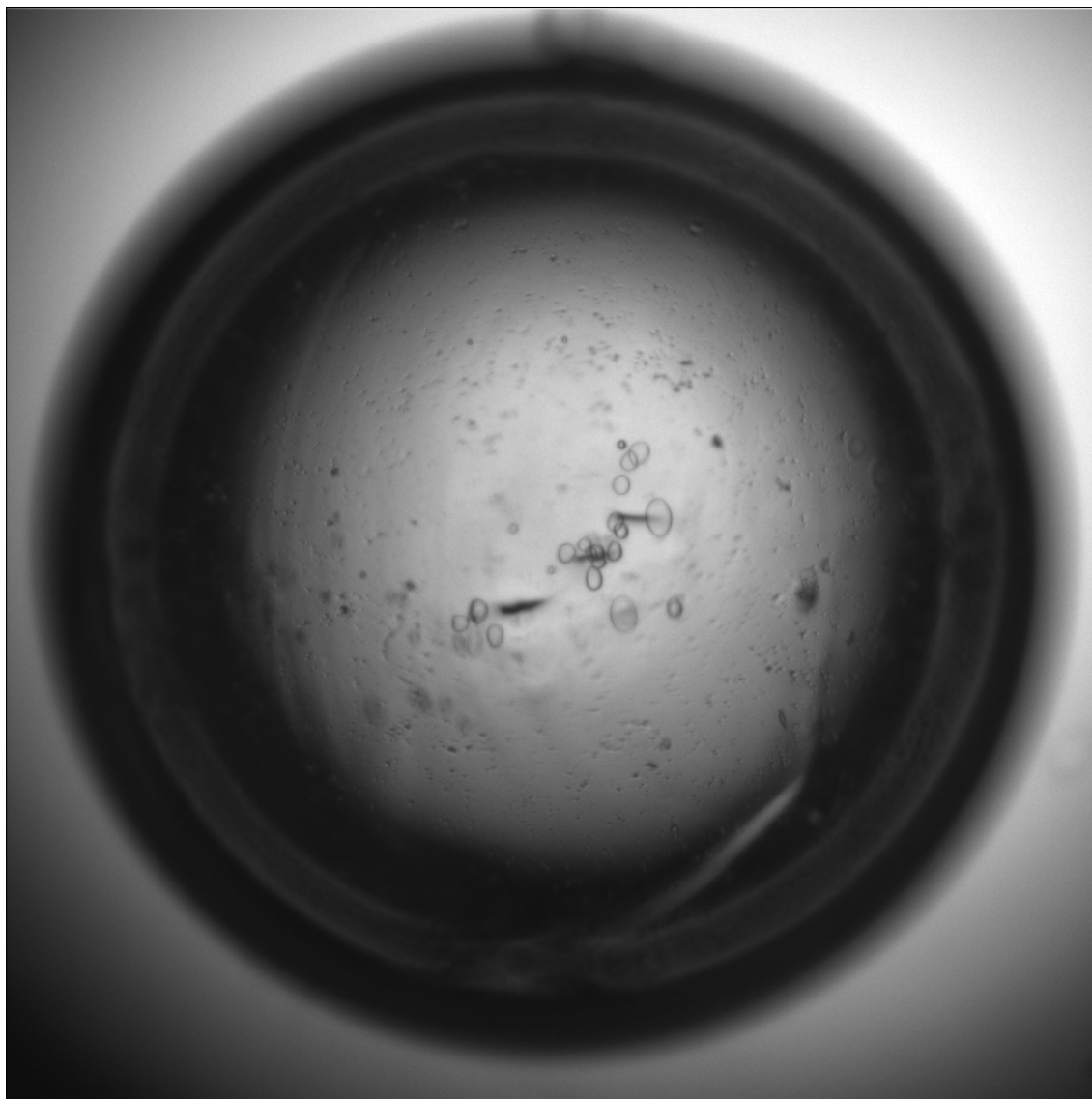


Figure 4.37: ^3He bubbles visible in a $250\ \mu\text{m}$ thick D-T layer in a 2 mm diameter shell. The D-T was cooled at 1 mK/min from the melt to 18.4 K.

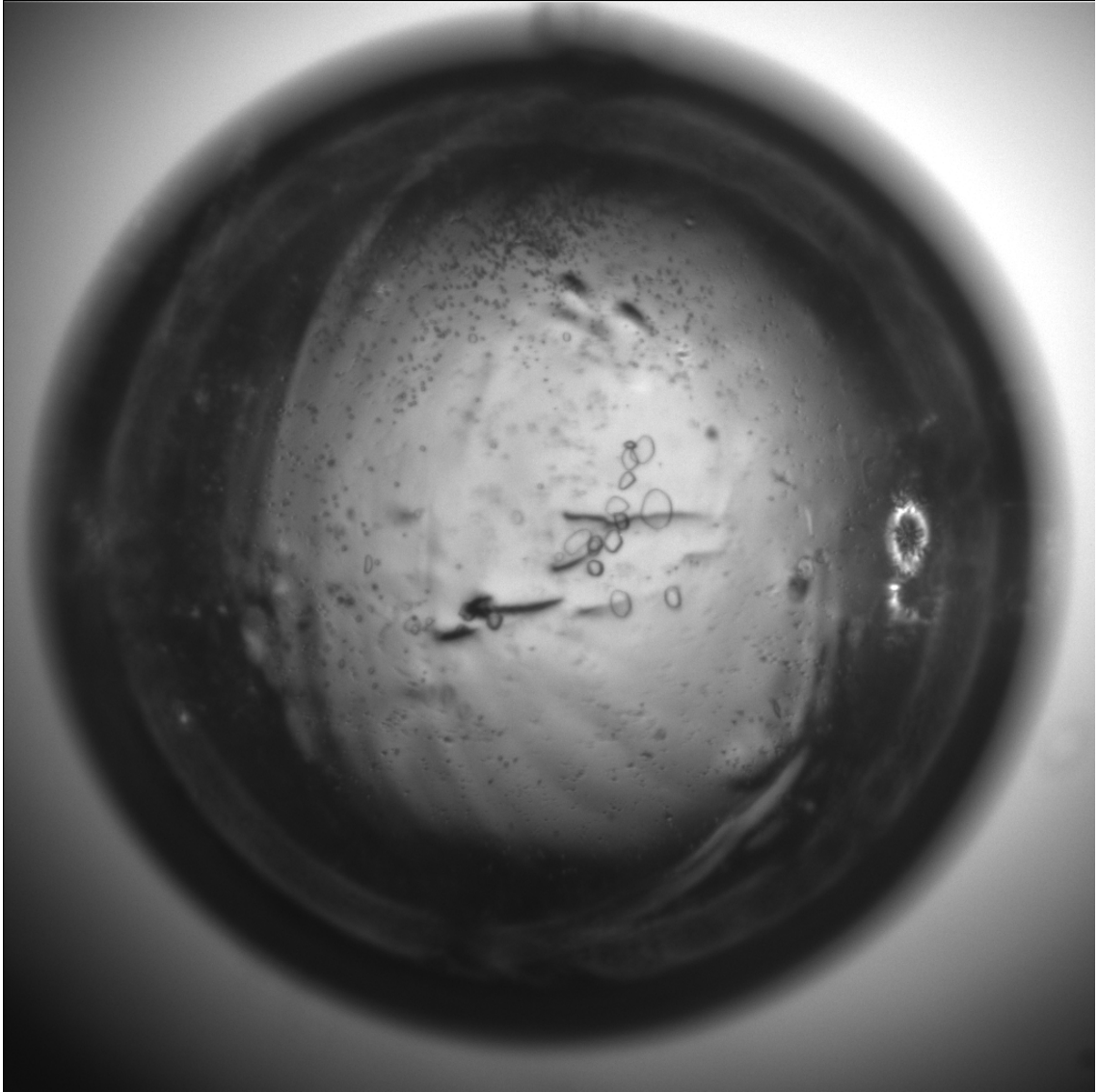


Figure 4.38: ^3He bubbles in a 250 μm thick D-T layer in a 2 mm diameter shell 2 hours after cooling from 18.4 K to 17.7 K. The white spot on the right side is the interferometry illumination in the orthogonal view.

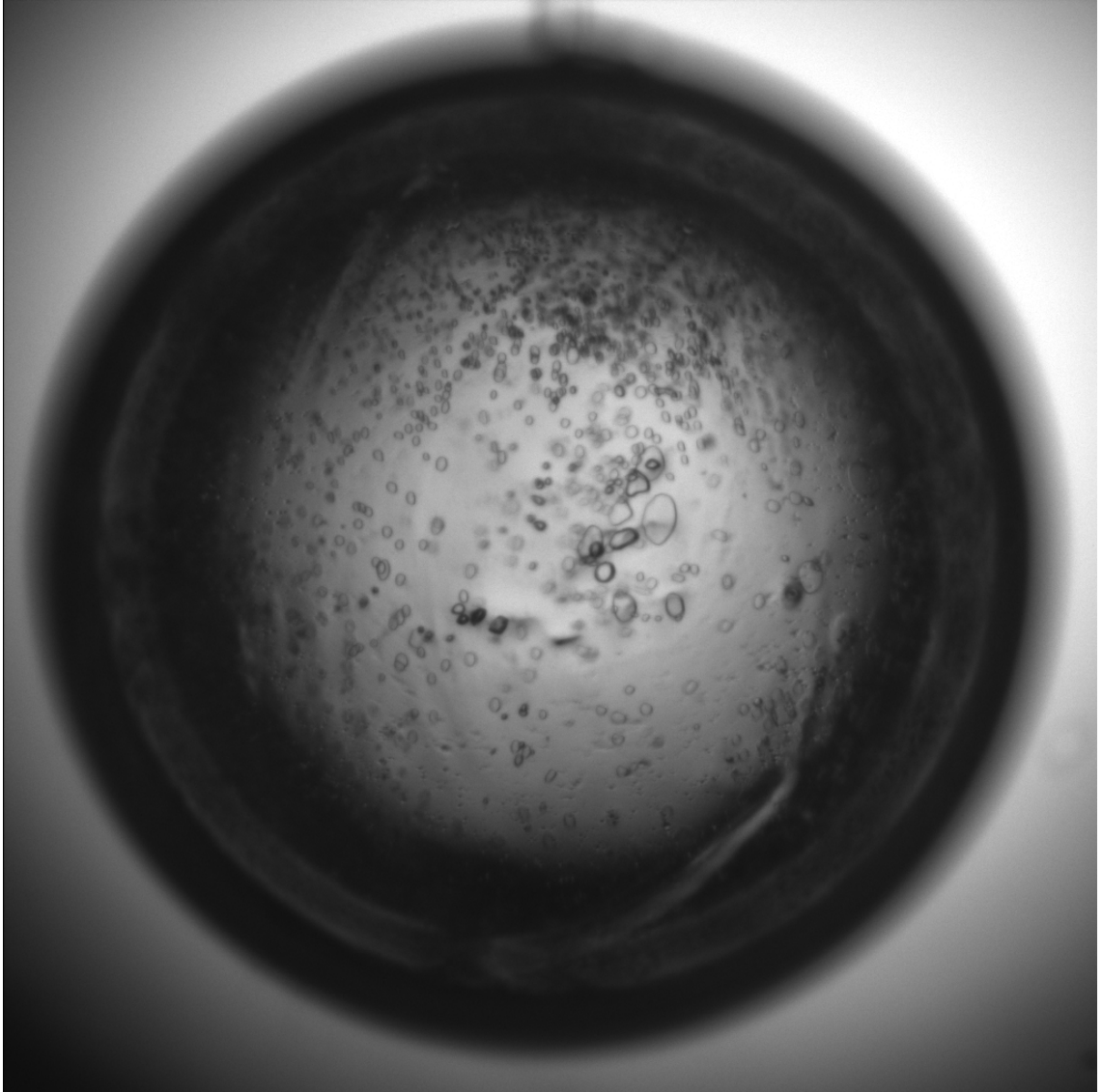


Figure 4.39: ^3He bubbles in a $250\ \mu\text{m}$ thick D-T layer in a 2 mm diameter shell 7 hours after cooling from 18.4 K to 17.7 K.

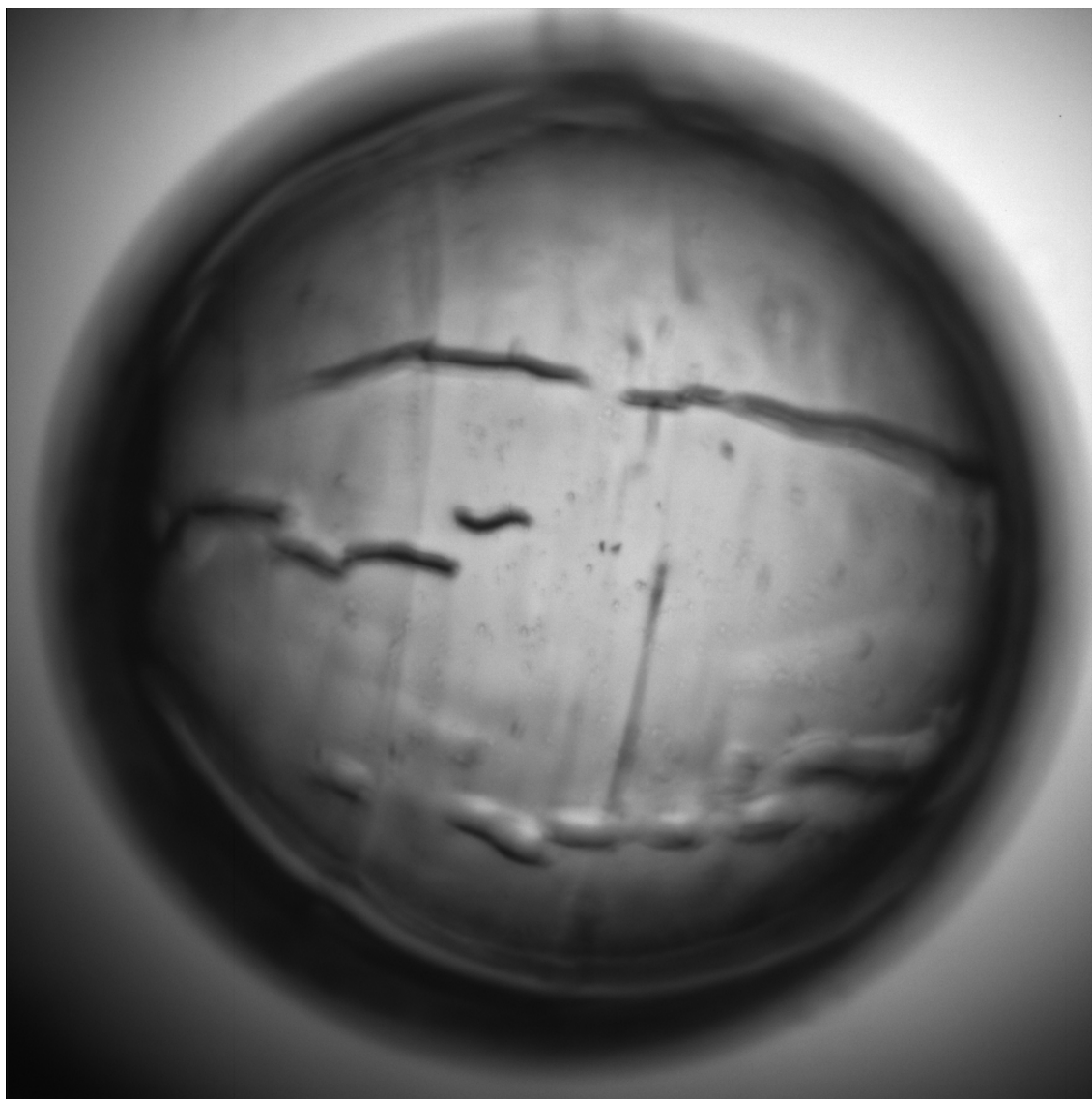


Figure 4.40: An $80\text{ }\mu\text{m}$ thick D-T layer at 17.5 K , 14 hours after cooling from 18.4 K . ^3He bubbles are not evident as they were in the $250\text{ }\mu\text{m}$ thick layer.

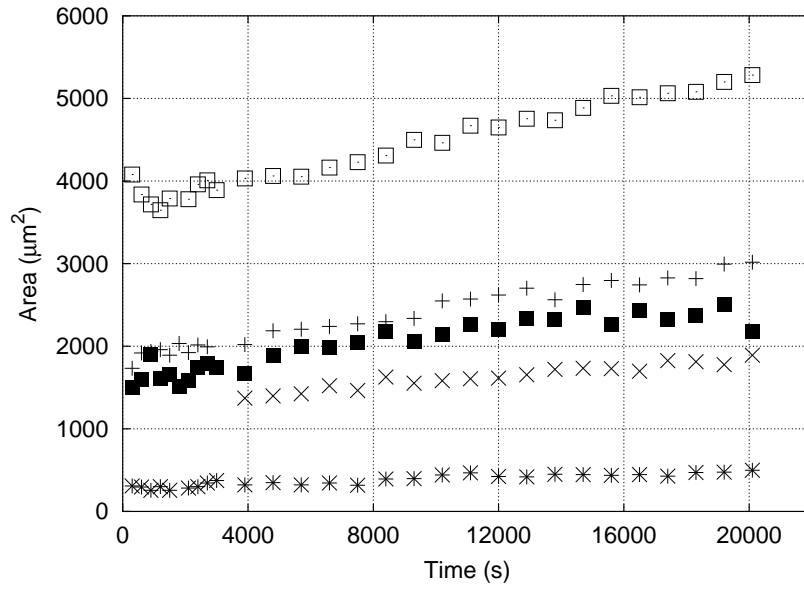


Figure 4.41: Measured area of ^3He bubbles in a $250\ \mu\text{m}$ thick D-T layer at 17.7 K.

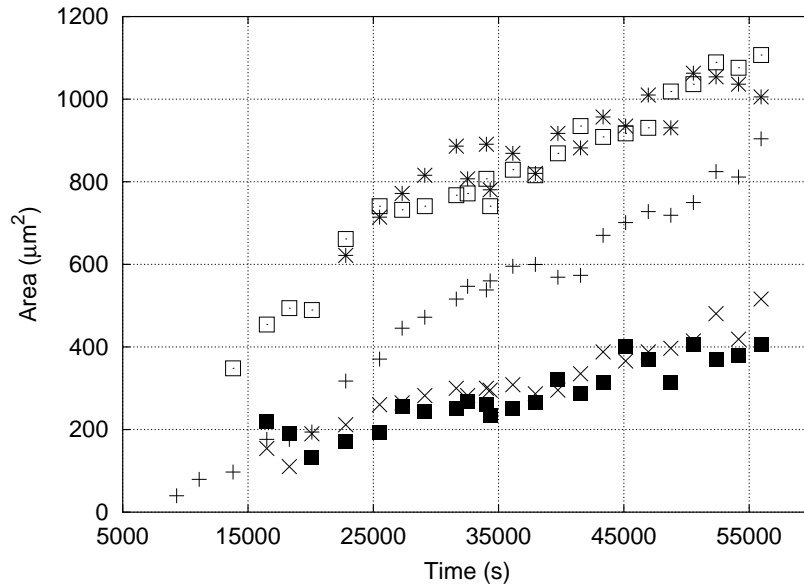


Figure 4.42: Measured area of ^3He bubbles in a $250\ \mu\text{m}$ thick D-T layer at 16.8 K.

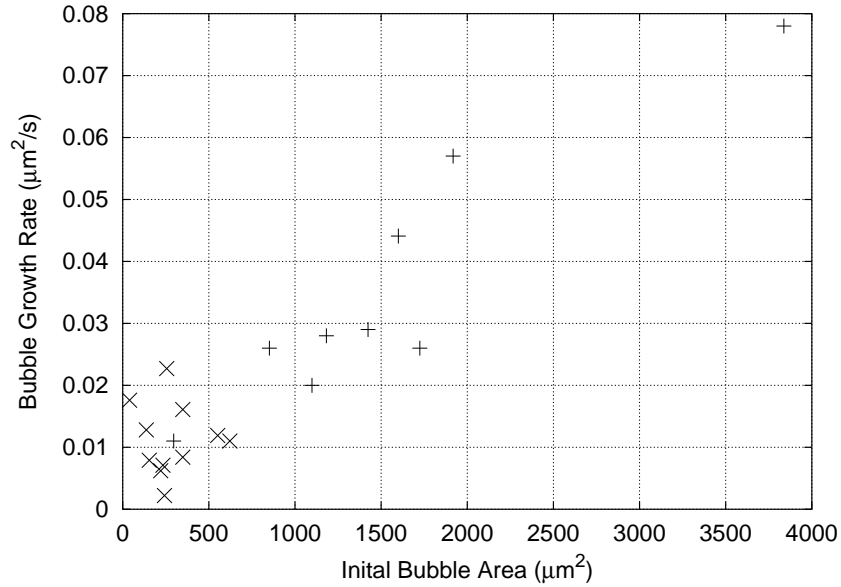


Figure 4.43: Measured growth rates of bubbles plotted as a function of their initial size at 17.7 K (+) and 16.8 K (x)

The scattered intensity from 19.5 K samples was much lower than that from samples 16 K and colder. Furthermore, the intensity increased steadily while at the lower temperatures, often by a factor of 1000 or more over 24 hours, whereas the higher temperature samples did not exhibit such an increase. This qualitative observation suggests that the one dimensional diffusion model, given by equations 4.2 and 4.3, describes the approach to a steady state population. The reduced diffusion at low temperature required a longer time to reach steady state with an ultimately higher concentration.

4.8.1 Coalescence

The large bubbles were often observed to coalesce. A few examples are shown in figure 4.44. The D-T is at 17.7 K for all images. The coalescence and subsequent shape adjustment is seen to be very slow, especially for the larger bubbles. Assuming that the bubbles were in equilibrium before coalescence the time required to return to equilibrium after coalescence

is determined by the vacancy flux, given by equation 4.7. The number of vacancies in a bubble is the difference between the number of gas atoms and the equivalent number of solid lattice sites. For the large bubbles shown in figure 4.44a with initial sizes of 18.1 μm and 15.1 μm , the number of gas atoms is much smaller than the number of vacancies and can be neglected in calculating the required number of vacancies. The number of ^3He atoms do, however, determine the bubble radius according to equation 4.5. Conservation of ^3He atoms for the bubbles in 4.44a requires an equilibrium radius of 23.6 μm after coalescence. The required number of vacancies is

$$\begin{aligned} N_v &= \frac{4\pi}{3} \rho_{\text{solid}} \left((23.6 \times 10^{-6} \text{m})^3 - (18.1 \times 10^{-6} \text{m})^3 - (15.1 \times 10^{-6} \text{m})^3 \right) \\ &= 4.7 \times 10^{14}, \end{aligned} \tag{4.48}$$

where ρ_{solid} is $3 \times 10^{28} \text{ 1/m}^3$. The vacancy concentration at 17.7 K from equation 4.6 is $1.3 \times 10^{25} \text{ 1/m}^3$ and the diffusivity is about $1 \times 10^{-13} \text{ m}^2/\text{s}$. Using equation 4.7 with $R = 20 \mu\text{m}$, vacancies arrive at a rate of 1.2×10^{10} per second. It should take the bubble about 40 000 seconds to return to equilibrium. Figure 4.44a shows substantial shape change after 3000 s, but has not yet reached complete equilibrium. Although it is not completely round, an effective radius calculated from the measured area is 24.5 μm and is close to the 23.6 μm predicted above.

The bubble in figure 4.44c does return to a circular shape after coalescence within 3000 seconds. Because the bubbles in c) are smaller than those in a), they require fewer vacancies. Using the measured radius of 10.7 μm for both bubbles the number of vacancies needed for the equilibrium radius of 15.1 μm after coalescence is 1.3×10^{14} . The smaller bubbles should return to equilibrium in about 1/3 of the time of 4.44a, or about 13 000 seconds. In this case the bubble profile is very close to circular after 3600 seconds, and the measured

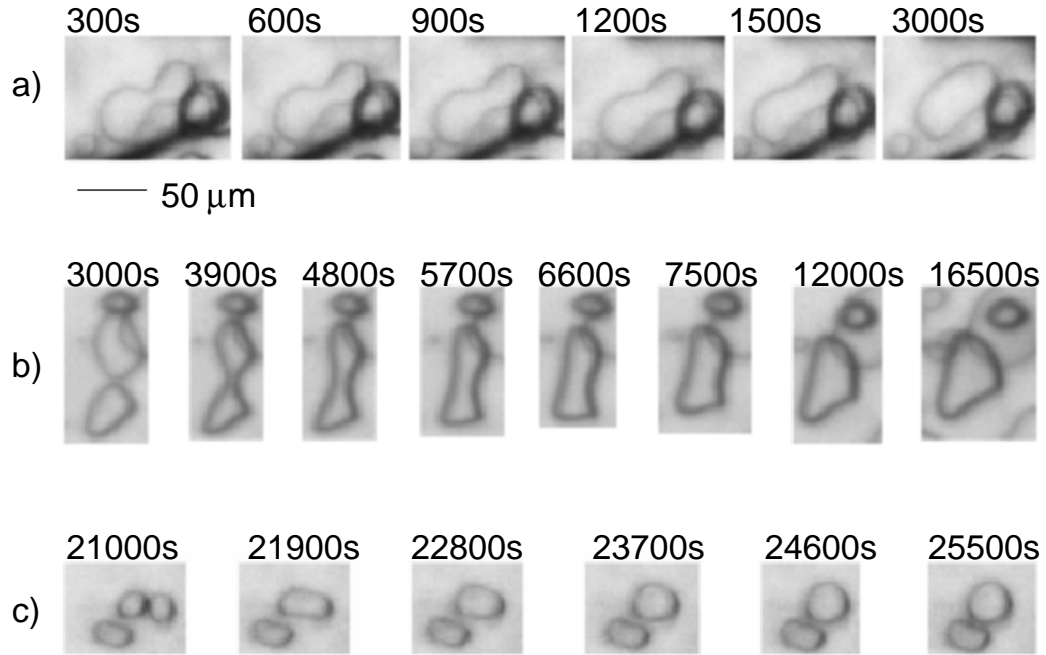


Figure 4.44: Several ^3He bubbles in D-T at 17.7 K coalescing. All images have the same scale indicated by the bar.

radius is $15.6 \mu\text{m}$. In both a) and c) the bubbles relax faster than predicted. The faster relaxation is likely due to a higher number of vacancies from radiation damage than is calculated assuming an equilibrium solid. However, both are oval, but nearly completely convex after 2700 and 900 seconds respectively, in agreement with the prediction that the larger bubble pair takes three times longer to reach equilibrium.

Since the shape of the bubble is determined by the surface energy of the D-T, a bubble inside the solid takes the same shape as an isolated D-T crystal of the same volume and crystal orientation. Hence, ^3He bubbles are expected to have the same shape as crystals previously measured, and in particular, should also exhibit facets as the roughening transition is passed for the respective crystal orientations. The images in figure 4.45 show a

number of bubbles at $17.7 \text{ K} = 0.90 \text{ T}_{\text{TP}}$ as a function of time. In each case it is clear that the bubbles are not completely faceted, but do show what looks to be a shape that is almost faceted. Bubble *a* starts in a shape close to hexagonal but subsequently the facets tend to round out and become less well defined as it continues to grow. The shape of *b* seems to suggest facets, as does *c*. *d* has sharp edges but is not in the hexagonal shape. It is surprising that even though the shape clearly changes on the time scales observed, the bubbles do not become cleanly faceted. This suggests that the D-T is still below the roughening transition temperature for these facets, but still warm enough that the facets are still rounded. This is in good agreement with the experiments on D_2 , where the facets were clearly visible at 16 K, but not as much at higher temperatures. Given the 1 K offset of the D_2 and the D-T triple point, the surface energy of the D-T is very close to the D_2 .

The bubble shape shows that substrate did not influence the crystal shapes and facet transitions observed in chapter 3. Similarly, the D-T surface energy does not differ from that of pure D_2 , justifying the use of the D_2 surface energy and surface smoothing model for D-T layers.

4.8.2 Bubbles driven by a thermal gradient

The bubble response to an applied thermal gradient was studied. Since the D-T self heating and infrared layer smoothing techniques rely on creating a thermal gradient within a layer this is of particular relevance. The thermal gradient in the experiment was a combination of the applied gradient by adjusting the temperature difference across the optical cell, and the internal D-T self heating. Since the self heating makes the thermal gradient position dependent within the layer, that needs to be taken into account. The thermal analysis finite element code COSMOS was used to model the thermal gradient throughout the

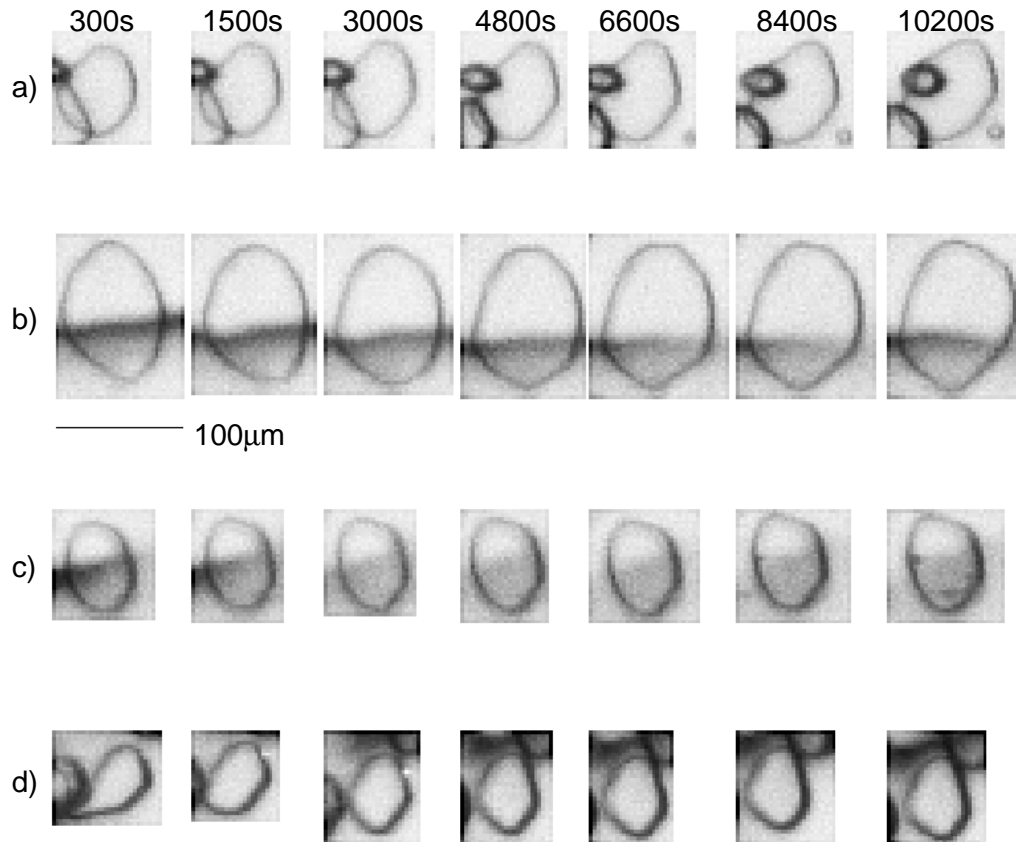


Figure 4.45: Several ^3He bubbles in D-T at 17.7 K. The bubbles are not cleanly faceted even though their shape evolves with time. The dark line though b) is a defect in the solid surface out of the plane of the bubble.

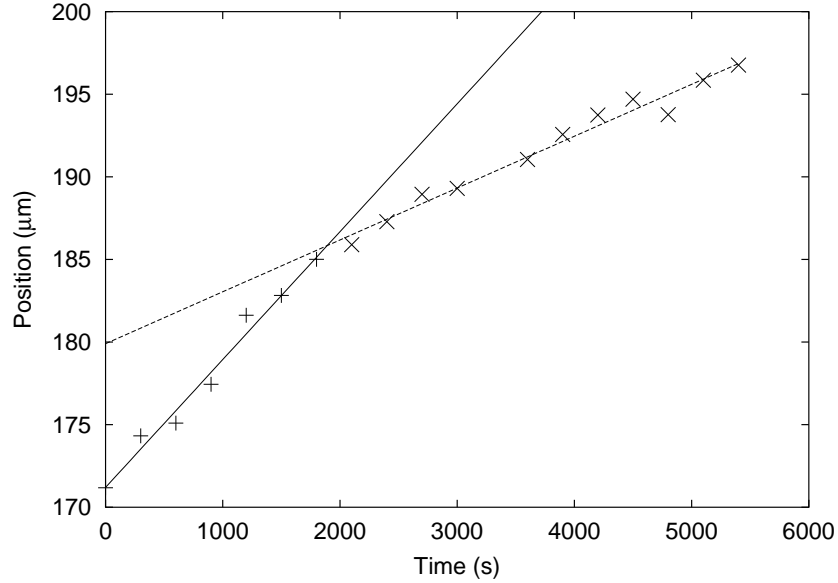


Figure 4.46: The vertical position of a bubble as a function of time in a sample at 16.7K. At $t = 1800$ s the thermal gradient is reduced from 72 K/m to 39 K/m. The solid line is a least squares fit to the first 1800s, and the dashed line to the remaining.

solid. The model showed the thermal gradient to be vertical in the D-T.

The positions of bubbles were recorded using the Photometrics camera set to record pictures at a set time interval. The bubble position within the layer vs time was later measured. Figure 4.46 shows the measured position of one bubble in D-T at 16.7K vs time. The thermal gradient was reduced from 72 K/m to 39 K/m at $t = 1800$ s. A least squares linear fit to the data gives the velocity of 7.7 nm/sec before and 3.1 nm/sec after the change. The factor of 2.5 change in the velocity is close to the 1.8 change in ∇T , hence the bubble velocity depends linearly on the thermal gradient as expected by the models.

Figure 4.47 shows the velocity for a number of bubbles in D-T at 16.7 K at a number of different thermal gradient values. Although there is a lot of scatter in the data, an increase in the velocity is evident, as indicated by the least squares fit. The fit is $(-2.8 \times 10^{-3} + 2.10 \times 10^{-4} \nabla T) \mu\text{m/sec}$, where ∇T is the thermal gradient in K/m. There are a number of possible reasons for the spread in data. First is the difference in size of

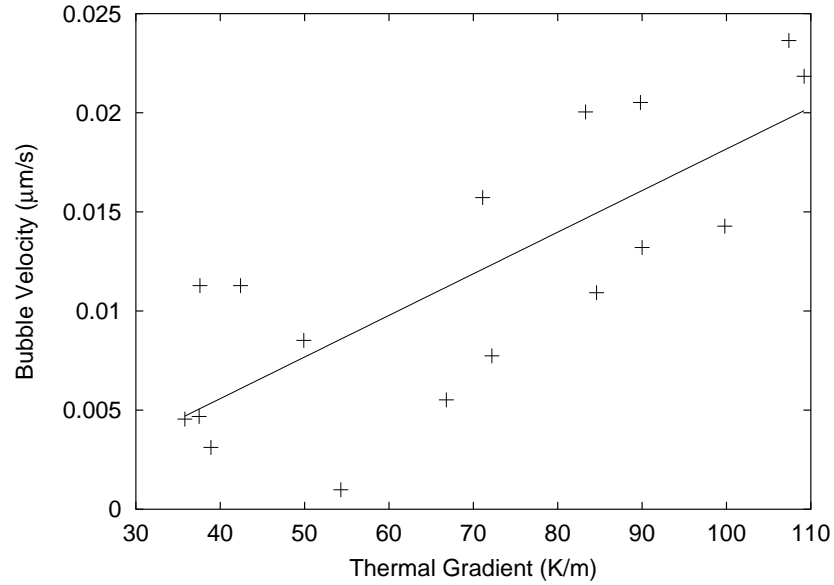


Figure 4.47: Bubble velocities vs thermal gradient in D-T at 16.7 K. The solid line is a linear least squares fit to the data.

the bubbles. There is no clear size dependence in the data. However, because it is only possible to see a small slice of the bubble the complete three dimensional shape is not known. Similarly, some of the randomness may be due to the nucleation requirement for movement of the bubble. Finally, any defects in the D-T may trap bubbles. This is shown in figure 4.48. The D-T sample at 19 K has a number of bubbles which move very little over the observation time. However, the white arrow shows one bubble which moves in response to the $\nabla T = 50$ K/m at $0.054 \mu\text{m}/\text{sec}$, consistent with bubble velocities at this temperature and ∇T . Near the end of the layer it appears to get trapped as its position stops changing. This may be due to a grain boundary in the solid, which explains why the bubbles seem to be trapped along a line, or interaction with a strain field around the neighboring bubble.

This large run to run variation is also evident in the velocities. The bubble speed was measured at several different temperatures, sizes, and thermal gradient values and is

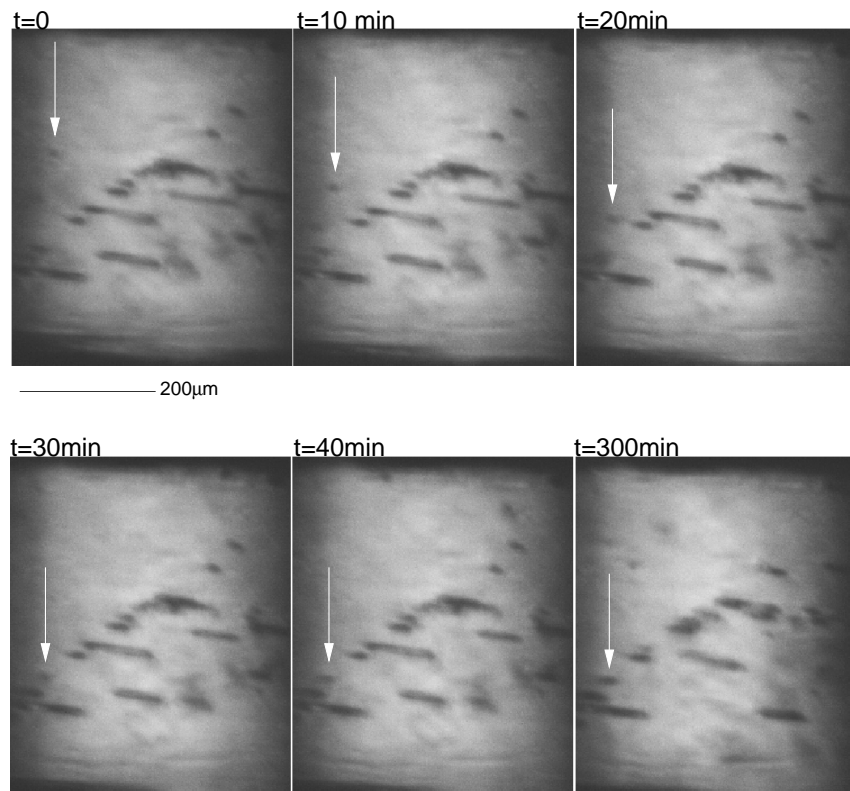


Figure 4.48: D-T sample at 19 K with bubbles. Most bubbles do not move during the observation time. The bubble with the arrow moves through the solid at $0.054 \mu\text{m}/\text{sec}$ until it comes to a stop.

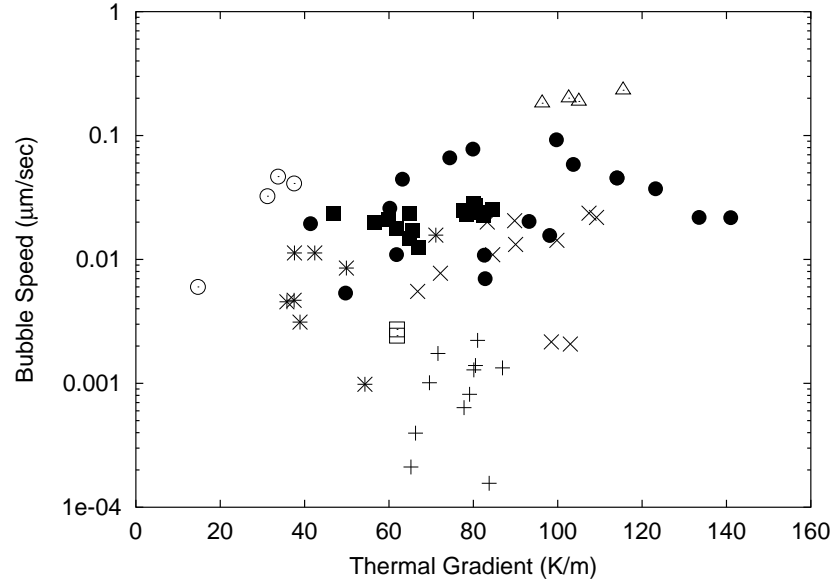


Figure 4.49: Measured bubble velocity at several different temperatures and thermal gradient values. The temperatures are 15.940K (+), 16.65 K (\times), 16.85 K (*), 16.93 K (\square), 17.8 K (\blacksquare), 19.0 K (\odot), 19.42 K (\triangle), 19.5 K (\bullet).

shown in figure 4.49. There is a slight trend for bubbles at higher temperatures to move faster than at lower temperatures for a given thermal gradient, but it is far from clear. There was no clear dependence on bubble size in the data. Brownian motion of bubbles large enough to be observed with the microscope was not observed nor was it expected based on the rapid decrease of the diffusion coefficient with increasing bubble size as shown earlier in figure 4.7.

Comparison with figure 4.9 shows that the measured velocities are within a factor of 10 of the values predicted for vapor transport. Unfortunately, the measurements were made on bubble sizes for which the model predicts little size dependence which prevents further confirmation of the model. Although volume transport is clearly much slower, surface diffusion cannot be ruled out.

4.9 Analysis

4.9.1 Surface diffusion

There are currently no measured values for the D-T surface diffusion coefficient, jump distance, or heat of transport. Order of magnitude estimates are possible for the jump distance and heat of transport, but the diffusion constant is very difficult to predict accurately. Instead, the measured bubble velocity data is used to set an upper bound on the surface diffusion coefficient and predict trends of the model.

The velocity at 19 K is on the order of $0.05 \mu\text{m/s}$ for bubbles $10 \mu\text{m}$ in radius with $\nabla T = 80 \text{ K/m}$. Q_s^* should be less than the heat of sublimation but about that order of magnitude^{93,102} so 1500 J/mole is a reasonable value. The D-T lattice spacing of 0.36 nm provides the surface density, ν_s . Then D_s is found to be $1.2 \times 10^{-5} \text{ m}^2/\text{s}$ using equation 4.11. This value is used in equation 4.10 to plot the bubble diffusivity in figure 4.50. For comparison, the VT diffusion coefficient is also plotted. The r^{-4} dependence makes surface diffusion transport much faster for small bubbles than either volume or vapor transport. However, care must be taken when applying this model to very small bubbles. Bubbles less than $\approx 1 \text{ nm}$ have less than ≈ 200 ^3He atoms and are much closer to the solid density than a vapor. The bubble diffusion must be the same rate as vacancy transport in the limit of a single atom ^3He bubble. The surface diffusion model of equation 4.10 fails to satisfy this requirement. Instead, it is likely there exists a cross over between the different mechanisms. The trend is probably correct, with VT dominating bubble motion for bubbles larger than $\approx 0.1 \mu\text{m} - 1 \mu\text{m}$ and SD controlling migration for smaller sizes.

Similarly, the r^{-1} drift velocity dependence of equation 4.11 predicts 1 nm bubbles traveling at $500 \mu\text{m/s}$ under the above conditions. All ^3He generated would be removed

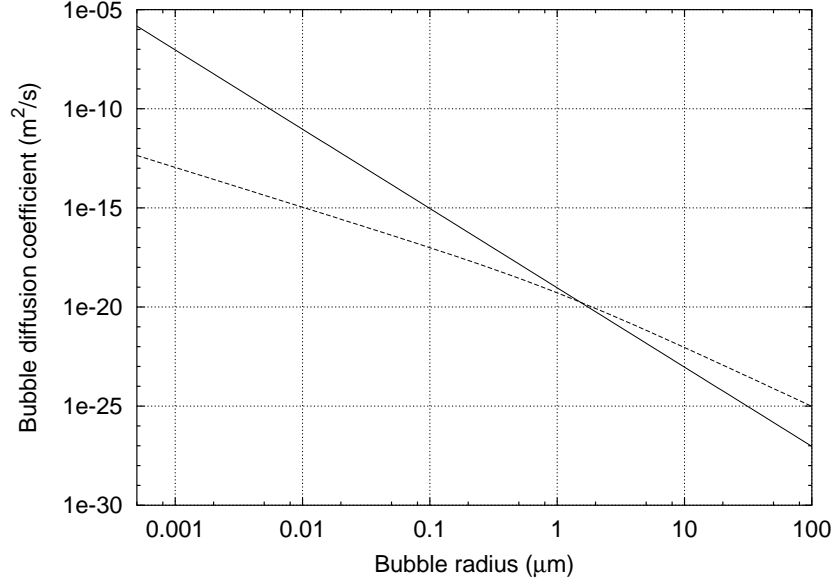


Figure 4.50: Bubble diffusion coefficient as a function of size for surface diffusion (solid) and vapor transport (dashed) controlled migration at 19 K. The surface diffusion coefficient was estimated using bubble velocities in a thermal gradient.

from the solid in a very short time, which does not agree with observations. D_s has likely been overestimated by equation 4.11. However, other rate limiting processes such as ledge nucleation⁷⁸ cannot be ruled out. Buescher and Meyer⁹³ found helium bubbles in UO_2 failed to follow the simple models and propose a surface-gas model to explain their results. More detailed experiments must be performed to determine which, if any, model is applicable to ^3He in D-T.

4.10 Conclusions

The diffusion constant of $< 1 \mu\text{m}$ ^3He bubbles in D-T was measured using dynamic light scattering and found to decrease from $1.1 \times 10^{-16} \text{ m}^2/\text{s}$ to $< 1 \times 10^{-17} \text{ m}^2/\text{s}$ at 19 K within 2.5 hours after freezing. The mean bubble growth rate and diffusion constant decrease with decreasing temperature. The growth rate of micron sized bubbles depends on the D-T temperature, layer thickness, and bubble size. These bubbles move in response to a

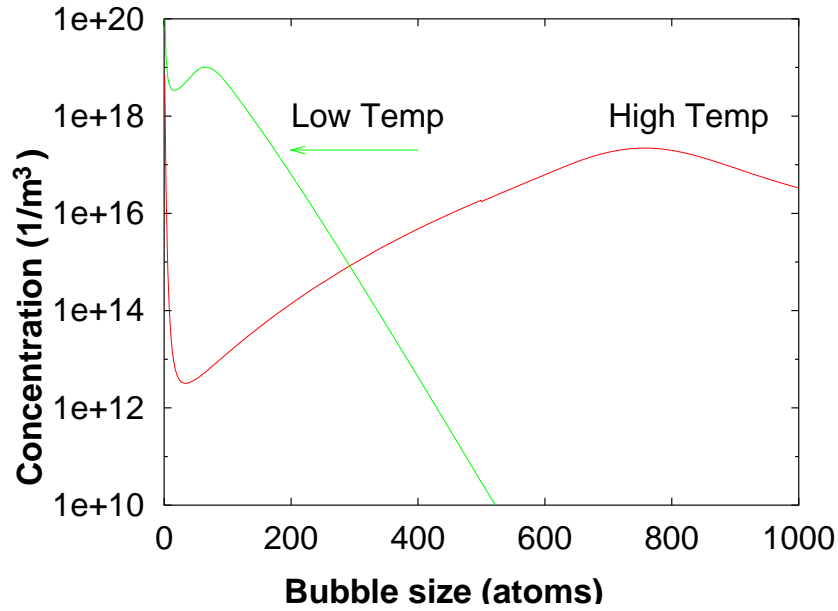


Figure 4.51: Modeled bubble size distribution for two different temperatures after the same time has elapsed based on a diffusion limited coalescence model.

thermal gradient, but they can be trapped or slowed by defects such as grain boundaries in D-T. The relatively fast migration of the bubbles indicates either vapor transport or surface diffusion dominate the motion. The measured velocities are sample dependent, but typically very close to the predicted vapor transport values.

Figure 4.51 shows the general trend for the bubble size distribution using Chandrasekhar's collision probability model⁹² discussed in section 4.3. The distribution is bimodal, with beta-decay constantly creating new atoms, and coalescence of small bubbles forming larger bubbles. At high temperatures the bubbles diffuse rapidly and quickly grow into large bubbles. The slower diffusion at low temperature reduces the bubble growth rate but has a higher peak concentration than the higher temperature case. This model agrees qualitatively with the light scattering experiments as well as the images shown in figure 4.2. Further, the rapid diffusion at high temperature allows atoms and small bubbles to escape from the solid before forming bubbles, particularly evident for layers less

than 100 μm thick, reducing the overall concentration.

The current NIF target design, filling, and transport results in nearly all ^3He produced entering the vapor region. Equation 4.1 and figure 4.3 accurately model the ^3He buildup in the vapor region for 100 μm thick layers above 18.5 K. NIF targets must be shot within a week after filling to obtain high yields.

Chapter 5

Conclusions

The results from several experiments were presented in this thesis. The Raman experiments indicate the D-T crystal structure is hcp. It was found that the Raman rotational line shape of is broadened in D-T, compared to the pure isotopes. The $J = 0-2$ hcp triplet was observed on T_2 but not for D_2 in D-T. The rotational lineshape was found to be a property of a mixture of hydrogen isotopes and not due to radiation damage in the solid as a similar broadening was observed in a mixture of H_2 -HD- D_2 . The Raman vibrational spectrum is shifted to higher energies and the $Q_1(1)/Q_1(0)$ intensity ratio is reduced in the mixture. Both effects result from the reduced molecular coupling due to the large vibrational energy difference of the isotopes.

The $J = 1-0$ $1/e$ time constant was found to be 1.9 hours for T_2 and 7.0 hours for D_2 between 5.4 and 10.2 K. The $1/e$ time increases rapidly above 10.2 K for both isotopes. These results show a similar trend as the NMR data.

Two facets exist on D_2 and HD crystals below $0.9 T_{TP}$. The a facet roughens between $0.9 T_{TP}$ and T_{TP} , while the c facet persists until the crystal melts. The surface energy of the c face is estimated to be $6.0 \times 10^{-3} \text{ J/m}^2$. The crystals grew very differently compared

to the rare gas solids which grow completely rounded above $0.8 T_{TP}$. The crystal facets set a lower limit on the roughness of D-T layers in NIF targets achievable using thermal smoothing methods.

Helium bubbles were observed in D-T. Light scattering shows that near 19 K the bubble diffusion constant decreases from $1 \times 10^{-16} \text{ m}^2/\text{s}$ to $1 \times 10^{-17} \text{ m}^2/\text{s}$ within a few hours of freezing. The diffusion is less than $1 \times 10^{-17} \text{ m}^2/\text{s}$ for lower temperatures. Small bubbles are trapped at low temperatures but become free as the temperature is raised. The bubble growth rate of bubbles observable with a microscope is size dependent, varying from $\approx 0.005 \mu\text{m}^2/\text{s}$ to $0.08 \mu\text{m}^2/\text{s}$ for bubbles from $8 \mu\text{m}$ up to $35 \mu\text{m}$ in radius. The bubbles are driven by a thermal gradient, with the velocity linear in the applied gradient. Bubbles are observed to become trapped in the solid, apparently at grain boundaries.

These experiments provide a better understanding of the physical properties of D-T that influence the layer uniformity in NIF targets. This information can be used to better plan target production, transport, and handling as well as model target performance.

Bibliography

1. J. Lindl, "Development of the Indirect-Drive Approach to Inertial Confinement Fusion and the Target Physics Basis for Ignition and Gain," *Physics of Plasmas* **2**, 3933–4024 (1995).
2. M. D. Rosen, "The Physics Issues that Determine Inertial Confinement Fusion Target Gain and Driver Requirements: A Tutorial," *Phys. Plasmas* **6**, 1690–1699 (1999).
3. P. A. Bradley and D. C. Wilson, "Physics of One-dimensional Capsule Designs for the National Ignition Facility," *Phys. Plasmas* **6**, 4293–4303 (1999).
4. A. J. Martin, R. J. Simms, and R. B. Jacobs, "Beta Energy Driven Uniform Deuterium-Tritium Ice Layer in Reactor-Size Cryogenic Inertial Fusion Targets," *J. Vac. Sci. Technol. A* **6**, 1885–1888 (1988).
5. J. K. Hoffer and L. R. Foreman, "Radioactive Induced Sublimation in Solid Tritium," *Phys. Rev. Lett.* **60**, 1310–1313 (1988).
6. J. K. Hoffer and L. R. Foreman, "Uniform Solid Deuterium-Tritium Layers Resulting From Radioactively Induced Sublimation," *J. Vac. Sci. Technol. A* **7**, 1161–1164 (1989).
7. P. C. Souers, *Hydrogen Properties for Fusion Energy* (University of California, Berkeley, 1986).
8. J. Sater, B. Kozioziemski, G. W. Collins, E. R. Mapoles, J. Pipes, J. Burmann, and T. P. Bernat, "Cryogenic D-T Fuel Layers Formed in 1 mm Spheres by Beta-Layering," *Fusion Tech.* **35**, 229–233 (1998).
9. J. K. Hoffer, L. R. Foreman, J. J. Sanchez, E. R. Mapoles, and J. D. Sheliak, "Surface Roughness Measurements of Beta-Layered Solid Deuterium-Tritium in Toroidal Geometries," *Fusion Tech.* **30**, 529–533 (1996).
10. I. F. Silvera, "The Solid Molecular Hydrogens in the Condensed Phase: Fundamentals and Static Properties," *Rev. Mod. Phys.* **52**, 393–452 (1980).
11. G. W. Collins, W. G. Unites, E. R. Mapoles, and T. P. Bernat, "Metastable Structures of Solid Hydrogen," *Phys. Rev. B* **53**, 102–106 (1996).
12. A. F. Schuch, R. L. Mills, and D. A. Depatie, *Phys. Rev.* **165**, 1032 (1968).

13. J. L. Yarnell, R. L. Mills, and A. F. Schuch, "Neutron Diffraction Studies of Deuterium Solid Structures and Transitions," *Fizika Nizkikh Temperatur* **1**, 760–769 (1975).
14. W. N. Hardy, I. F. Silvera, and J. P. McTague, "Raman Scattering in Oriented Crystals of Paradeuterium and Orthohydrogen," *Phys. Rev. B* **12**, 753–789 (1975).
15. N. S. Sullivan, "Orientational Ordering in Solid Hydrogen," *J. de Phys.* **37**, 981–989 (1976).
16. C. Kittel, *Introduction to Solid State Physics*, 7th ed. (John Wiley and Sons, 1996).
17. G. W. Collins, P. C. Souers, J. L. Maienschein, E. R. Mapoles, and J. R. Gaines, "Atomic-hydrogen Concentration in Solid D-T and T₂," *Phys. Rev. B* **45**, 549–556 (1992).
18. R. M. Kulsrud, H. P. Furth, E. J. Valeo, and M. Goldhaber, "Fusion Reactor Plasmas with Polarized Nuclei," *Phys. Rev. Lett.* **49**, 1248–1251 .
19. J. D. Sater, J. R. Gaines, E. M. Fearon, P. C. Souers, F. E. McMurphy, and E. R. Mapoles, "Ortho-to-para Conversion in Solid Tritium. II. Experimental Values," *Phys. Rev. B* **37**, 1482–1491 (1988).
20. G. W. Collins, E. M. Fearon, E. R. Mapoles, R. T. Tsugawa, P. C. Souers, and P. A. Fedders, "J=1 to J=0 D₂ Conversion in Solid D-T," *Phys. Rev. B* **44**, 6598–6607 (1991).
21. S. S. Bhatnagar, E. J. Allin, and H. L. Welsh, "The Raman Spectra of Liquid and Solid H₂, D₂, and HD at High Resolution," *Can. J. Phys.* **40**, 9 (1962).
22. V. Soots, E. J. Allin, and H. L. Welsh, "Variation of the Raman Spectrum of Solid Hydrogen with Ortho-Para Ratio," *Can. J. Phys.* **43**, 1985–1995 (1965).
23. J. V. Kranendonk, *Solid Hydrogen* (Plenum Press, New York, 1983).
24. H. M. James and J. V. Kranendonk, "Theory of the Anomalous Intensities in the Vibrational Raman Spectra of Solid Hydrogen and Deuterium," *Phys. Rev.* **164**, 1159–1168 (1967).
25. J. V. Kranendonk, "Theory of the Infrared and Raman Spectrum of Solid Parahydrogen," *Can. J. Phys.* **38**, 240–261 (1960).
26. L. D. Landau and E. M. Lifshitz, *Statistical Physics*, 3rd ed. (Pergamon, 1980).
27. G. Baym, in *Lectures on Quantum Mechanics* (Addison–Wesley, Reading, Massachusetts, 1990), Chap. 15, pp. 332–338.
28. J. A. Berlinsky and W. N. Hardy, "Theory of Ortho-Para Conversion and its Effect on the NMR Spectrum of Ordered Solid Ortho-Hydrogen," *Phys. Rev. B* **8**, 5013–5027 (1973).
29. Y. Cao, J. R. Gaines, P. A. Fedders, and P. C. Souers, "Ortho-to-para Conversion in Solid Tritium. I. Theoretical Models," *Phys. Rev. B* **37**, 1474–1481 (1988).

30. J. R. Ferraro and K. Nakamoto, *Introductory Raman Spectroscopy* (Academic Press, 1994).
31. E. J. Allin and S. M. Till, "The Vibrational Raman Spectrum of Compressed Solid Hydrogen," *Can. J. Phys.* **57**, 442–448 (1979).
32. D. M. Brown and W. B. Daniels, "Vibrational Raman Spectra of Hydrogen and Deuterium Mixtures at High Pressures," *Phys. Rev. A* **45**, 6429–6435 (1992).
33. K. Veirs, "A Raman Spectroscopic Investigation of Molecular Hydrogen," Technical Report No. LBL-20565, Lawrence Berkeley Laboratory (1985) .
34. W. Kolos and L. Wolniewicz, "Polarizability of the Hydrogen Molecule," *J. Chem. Phys.* **46**, 1426–1432 (1968).
35. C. Schwartz and R. J. Le Roy, "Nonadiabatic Eigenvalues and Adiabatic Matrix Elements for all Isotopes of Diatomic Hydrogen," *J. Mol. Spec.* **121**, 420–439 (1987).
36. M. C. Drake, G. J. Rosasco, R. Schneggenburger, and R. L. Nolen, Jr, "Nondestructive Analysis of Laser Fusion Microsphere Targets Using Rotational Raman Spectroscopy," *J. Appl. Phys.* **50**, 7894–7897 (1979).
37. W. R. C. Prior and E. J. Allin, "Fundamental and Overtone Vibrational Transitions in the Raman Spectrum of hcp Solid Hydrogen," *Can. J. Phys.* **50**, 1471–1479 (1972).
38. W. R. C. Prior and E. J. Allin, "The Q Branch of the Fundamental Raman Band of the Ordered Phase of Solid Hydrogen and Deuterium," *Can. J. Phys.* **51**, 1935–1943 (1973).
39. H. G. M. Edwards, D. A. Long, H. R. Mansour, and K. A. B. Najm, "The Pure Rotational and Vibrational-Rotational Raman Spectra of $^1\text{H}^3\text{H}$ and $^2\text{H}^3\text{H}$," *J. Raman Spec.* **8**, 251–254 (1979).
40. R. J. Wijngaarden and I. F. Silvera, "Raman Spectrum of Solid Orthodeuterium to 150 kbar at 5 K," *Phys. Rev. Lett.* **44**, 456–459 (1980).
41. E. R. Mapoles, J. Sater, J. Pipes, and E. Monsler, "Smoothing of Deuterium-Tritium Ice by Electrical Heating of the Saturated Vapor," *Phys. Rev. E* **55**, 3473–3480 (1997).
42. D. N. Bittner, G. W. Collins, E. Monsler, and S. Letts, "Forming Uniform HD Layers in Shells Using Infrared Radiation," *Fusion Technology* **35**, 244–249 (1999).
43. G. W. Collins, T. P. Bernat, E. R. Mapoles, B. J. Kozioziemski, and C. Duriez, submitted to *J. Appl. Phys. Lett.* (unpublished).
44. M. Maruyama, "Growth and Roughening Transition of Rare Gas Crystals," *J. Crystal Growth* **89**, 415–422 (1988).
45. M. Maruyama, "Surface Premelting Phenomena of Rare Gas Crystals," *J. Crystal Growth* **94**, 757–761 (1989).

46. D.-M. Zhu and J. G. Dash, "Surface Melting and Roughening of Adsorbed Argon Films," *Phys. Rev. Lett.* **57**, 2959–2962 (1986).
47. D.-M. Zhu and J. G. Dash, "Evolution of Multilayer Ar and Ne Films From Two-Dimensional to Bulk Behavior," *Phys. Rev. B* **38**, 11673–11687 (1988).
48. J. Ma, D. L. Kingsbury, F. Liu, and O. E. Vilches, "Multilayer Adsorption of H_2 on Uniform MgO Substrates," *Phys. Rev. Lett.* **61**, 2348–2351 (1988).
49. C. Herring, "Some Theorems on the Free Energies of Crystal Surfaces," *Phys. Rev.* **82**, 87–93 (1951).
50. I. V. Markov, *Crystal Growth for Beginners* (World Scientific, 1995).
51. *Collected Papers of L. D. Landau*, D. Ter Haar, ed., (Gordon and Breach, New York, 1965), pp. 540–545.
52. C. Godrèche, *Solids Far From Equilibrium* (Cambridge University Press, Cambridge, 1992).
53. C. Jayaprakash, W. F. Saam, and S. Teitel, "Roughening and Facet Formation in Crystals," *Phys. Rev. Lett.* **50**, 2017–2020 (1983).
54. C. Rottman and M. Wortis, "Equilibrium Crystal Shapes for Lattice Models with Nearest- and Next-nearest-neighbor interactions," *Phys. Rev. B* **29**, 328–339 (1984).
55. S. Toschev, in *Crystal Growth: An Introduction*, P. Hartman, ed., (North Holland, 1973), Chap. Equilibrium Forms, pp. 328–341.
56. P. Nozières, in *Shape and Growth of Crystals*, C. Godrèche, ed., (Cambridge University Press, 1992), Chap. 1.
57. W. K. Burton, N. Cabrera, and F. C. Frank, "The Growth of Crystals and the Equilibrium Structure of Their Surfaces," *Phil. Trans. R. Soc.* **243**, 299 (1951).
58. P. E. Wolf, F. Gallet, S. Balibar, E. Rolley, and P. Nozières, "Crystal Growth and Crystal Curvature Near Roughening Transitions in HCP 4He ," *J. de Physique* **46**, 1987–2007 (1985).
59. D. S. Fisher and J. D. Weeks, "Shape of Crystals at Low Temperatures: Absence of Quantum Roughening," *Phys. Rev. Lett.* **50**, 1077–1080 (1983).
60. J. D. Weeks, in *Ordering in Strongly Fluctuating Condensed Matter Systems*, T. Riste, ed., (Plenum, 1980), pp. 293–317.
61. R. V. Ramanujan, "Equilibrium Crystal Shapes and Their Application to Nucleation in Solid," *Materials Science and Engineering B* **32**, 125–135 (1995).
62. M. Touzani and M. Wortis, "Simple Model for the Equilibrium Shape of 4He Crystals," *Phys. Rev. B* **36**, 3598–3602 (1987).
63. A. V. Babkin, D. B. Kopeliovich, and A. Y. Parshin, "An Experimental Investigation of Roughening Phase Transitions in 4He Crystals," *Sov. Phys. JETP* **62**, 1322–1327 (1985).

64. A. V. Babkin, K. O. Keshishev, D. B. Kopeliovich, and A. Y. Parshin, "Investigation of the Equilibrium Form of Helium Crystals in the Vicinity of Faceting Phase Transitions," *JETP Lett.* **39**, 633–636 (1984).
65. J. E. Avron, L. S. Balfour, C. G. Kuper, J. Landau, S. G. Lipson, and L. S. Schulman, "Roughening Transition in the ^4He Solid-Superfluid Interface," *Phys. Rev. Lett.* **45**, 814–817 (1980).
66. C. Jayaprakash and W. F. Saam, "Thermal Evolution of Crystal Shapes: The fcc Crystal," *Phys. Rev. B* **30**, 3916–3928 (1984).
67. J. E. Avron, J. E. Taylor, and R. K. P. Zia, "Equilibrium Shapes of Crystals in a Gravitational Field: Crystals on a Table," *J. Stat. Phys.* **33**, 493–522 (1983).
68. P. E. Wolf, S. Balibar, and F. Gallet, "Experimental Observation of a Third Roughening Transition on hcp ^4He Crystals," *Phys. Rev. Lett.* **51**, 1366–1369 (1983).
69. J. Bodensohn, K. Nicolai, and P. Leiderer, "The Growth of Atomically Rough ^4He Crystals," *Zeitschrift fur Physik B.* **64**, 55–64 (1986).
70. Y. Carmi, E. Polturak, and S. G. Lipson, "Roughening Transition in Dilute ^3He - ^4He Mixture Crystals," *Phys. Rev. Lett.* **62**, 1364–1367 (1989).
71. V. L. Tsymbalenko, "Study of the Growth Kinetics of Facets in a Free-Growing ^4He Crystal," *Low Temp. Phys.* **21**, 120–128 (1995).
72. Y. Carmi, S. G. Lipson, and E. Polturak, "Continuous and First-Order Wetting Transitions of hcp ^4He Crystals," *Phys. Rev. Lett.* **54**, 2042–2044 (1985).
73. W. A. Miller, G. J. C. Carpenter, and G. A. Chadwick, "Anisotropy of Interfacial Free Energy of some Hexagonal Close-packed Metals," *Phil. Mag.* **19**, 305–319 (1969).
74. J. D. Sater, Private communication.
75. O. V. Kantur and V. M. Kyashkin, "Fragmentation of Crystals Growing on Bent Surfaces," *Phys. Met. Metall.* **44**, 1097–1099 (1977).
76. R. S. Barnes, "A Theory of Swelling and Gas Release for Reactor Materials," *J. Nucl. Mat.* **11**, 135–148 (1964).
77. F. A. Nichols, "Kinetics of Diffusional Motion of Pores in Solids," *J. Nucl. Mat.* **30**, 149–165 (1969).
78. P. J. Goodhew and S. K. Tyler, "Helium Bubble Behaviour in b.c.c Metals Below $0.65 T_m$," *Proc. R. Soc. Lond. A* **377**, 151–184 (1981).
79. P. J. Goodhew, "On the Migration of Helium Bubbles," *Radiation Effects* **78**, 381–383 (1983).
80. G. W. Greenwood and M. V. Speight, "An Analysis of the Diffusion of Fission Gas Bubbles and its Effect on the Behaviour of Reactor Fuels," *J. Nucl. Mat.* **10**, 140–144 (1963).

81. E. E. Gruber, "Calculated Size Distribution for Gas Bubble Migration and Coalescence in Solids," *J. Appl. Phys.* **38**, 243–250 (1967).
82. K. Ono, S. Furuno, K. Hojou, T. Kino, K. Izui, O. Takaoka, N. Kubo, K. Mizuno, and K. Ito, "In-situ Observation of the Migration and Growth of Helium Bubbles in Aluminum," *J. Nucl. Mat.* **191-194**, 1269–1273 (1992).
83. H. Trinkaus, "Modeling of Helium Effects in Metals: High Temperature Embrittlement," *J. Nucl. Mat.* **133&134**, 105–112 (1985).
84. H. Ullmaier, "Introductory Remarks: Helium in Metals," *Radiation Effects* **78**, 1–10 (1983).
85. B. N. Singh and H. Trinkaus, "An Analysis of the Bubble Formation Behaviour Under Different Experimental Conditions," *J. Nucl. Matl.* **186**, 153–165 (1992).
86. S. E. Donnelly, "The Density and Pressure of Helium in Bubbles in Implanted Metals: A Critical Review," *Radiation Effects* **90**, 1–47 (1985).
87. *CRC Handbook of Chemistry and Physics*, 71st ed., D. R. Lide, ed., (CRC Press, 1990).
88. *American Institute of Physics Handbook* (McGraw-Hill, New York, 1972).
89. D. Kaletta, "The Growth of Gas Bubbles in Solids Under Irradiation at Elevated Temperatures Around $0.5 T_m$," *Radiation Effects* **78**, 245–259 (1983).
90. *Solid State Physics* (Holt, Rinehart and Winston, New York, 1976), pp. 616–621.
91. J. R. Gaines, P. A. Fedder, G. W. Collins, J. D. Sater, and P. C. Souers, "Diffusion of Atoms and Molecules in the Solid Hydrogens," *Phys. Rev. B* **52**, 7243–7251 (1995).
92. S. Chandrasekar, "Stochastic Problems in Physics and Astronomy," *Reviews of Modern Physics* **15**, 1 (1943).
93. B. J. Buescher and R. O. Meyer, "Thermal-Gradient Migration of Helium Bubbles in Uranium Dioxide," *J. Nucl. Mat.* **48**, 143–156 (1973).
94. R. J. Ackermann, E. G. Rauh, and M. H. Rand, "A Re-Determination and Re-Assessment of the Thermodynamics of Sublimation of Uranium Dioxide," In *International Symposium on Thermodynamics of Nuclear Materials*, **1**, 11–27 (IAEA, Vienna, 1980).
95. A. J. E. Foreman and B. N. Singh, "Gas Diffusion and Temperature Dependence of Bubble Nucleation During Irradiation," *J. Nucl. Matl.* **141-143**, 672–676 (1986).
96. F. Reif, *Fundamentals of Statistical and Thermal Physics* (McGraw-Hill, New York, 1965).
97. J. Volkl and G. Alefeld, "The Gorsky Effect: Recent Results," *Nuovo Cimento* **33**, 190–204 (1976).

98. J. A. Bierlein, "A Phenomenological Theory of the Soret Diffusion," *J. Chem. Phys.* **23**, 10–14 (1955).
99. L. S. Darken and R. A. Oriani, "Thermal Diffusion in Solid Alloys," *Acta Metallurgica* **2**, 841–847 (1954).
100. H. B. Huntington, "Driving Forces for Thermal Mass Transport," *J. Phys. Chem. Solids* **29**, 1641–1651 (1968).
101. G. W. Collins, P. C. Souers, E. M. Fearon, E. R. Mapoles, R. T. Tsugawa, and J. R. Gaines, "Thermal Conductivity of Condensed D-T and T₂," *Phys. Rev. B* **41**, 1816–1823 (1990).
102. P. G. Shewmon, *Diffusion in Solids* (McGraw-Hill Book Company, Inc., New York, 1963).
103. D. Preininger and D. Kaletta, "The Effect of the Immobilization of Helium Bubbles Generated During Irradiation on Their Growth by Coalescence," *J. Nucl. Matl.* **122**, 520–522 (1984).
104. D. Preininger and D. Kaletta, "The Growth of Gas-Bubbles by Coalescence in Solid During Continuous Gas Generation," *J. Nucl. Matl.* **117**, 239–243 (1983).
105. H. C. van de Hulst, in *Light Scattering by Small Particles* (Dover, New York, 1981), Chap. 6.
106. B. J. Berne and R. Pecora, *Dynamic Light Scattering* (John Wiley and Sons, New York, 1976).
107. H. Z. Cummins and E. R. Pike, *Photon Correlation Spectroscopy and Velocimetry* (Plenum, New York, 1977).
108. J. D. Jackson, in *Classical Electrodynamics* (John Wiley and Sons, New York, 1975), Chap. 9.6, pp. 412,417.
109. D. J. Griffiths, *Introduction to Electrodynamics*, 2 ed. (Prentics Hall, 1989).
110. M. Bertero, P. Brianzi, E. R. Pike, G. de Villiers, K. H. Lan, and N. Ostrowsky, "Light Scattering Polydispersity Analysis of Molecular Diffusion by Laplace Transform Inversion in Weighted Spaces," *J. Chem. Phys.* **82**, 1551–1554 (1985).
111. N. Ostrowsky, D. Sornette, P. Parker, and E. R. Pike, "Exponential Sampling Method for Light Scattering Polydispersity Analysis," *Optica Acta* **28**, 1059–1070 (1981).
112. M. Bertero, P. Boccacci, and E. R. Pike, "On the Recovery and Resolution of Exponential Relaxation Rates from Experimental Data: A Singular-Value Analysis of the Laplace Transform Inversion in the Presence of Noise," *Proc. R. Soc. Lond. A* **383**, 15–29 (1982).
113. M. Bertero, F. A. Grünbaum, and L. Rebolia, "Spectral Properties of a Differential Operator Related to the Inversion of the Finite Laplace Transform," *Inverse Problems* **2**, 131–139 (1986).

- 114. D. E. Koppel, "Analysis of Macromolecular Polydispersity in Intensity Correlation Spectroscopy: The Method of Cumulants," *J. Chem. Phys.* **57**, 4814–4820 (1972).
- 115. G. A. Brehm and V. A. Bloomfield, "Analysis of Polydispersity in Polymer Solutions by Inelastic Laser Light Scattering," *Macromolecules* **8**, 663–665 (1975).
- 116. M. Schmidt, W. Burchard, and N. C. Ford, "Quasielastic Light Scattering: An Experimental Study of Polydispersity," *Macromolecules* **11**, 452–454 (1978).
- 117. B. Chu, *Laser Light Scattering: Basic Principles and Practice* (Academic Press, Inc., New York, 1991).
- 118. B. Crosignani, P. DiPorto, and M. Bertolotti, *Statistical Properties of Scattered Light* (Academic Press, New York, 1975).
- 119. E. Jakeman and E. R. Pike, "The Intensity-Fluctuation Distribution of Gaussian Light," *J. Phys. A.* **1**, 128–138 (1968).
- 120. E. Jakeman, C. J. Oliver, and E. R. Pike, "Measurements of the Factorization Properties of Higher-Order Optical Correlation Functions," *J. Phys. A.* **1**, 497–499 (1968).
- 121. Y. Yeh and H. Z. Cummins, "Localized Fluid Flow Measurements with an He-Ne Laser Spectrometer," *Appl. Phys. Lett.* **4**, 176–178 (1964).
- 122. R. V. Edwards, J. C. Angus, M. J. French, and J. W. Dunning, Jr, "Spectral Analysis of the Signal from the Laser Doppler Flowmeter: Time-Independent Systems," *J. Appl. Phys.* **42**, 837–850 (1971).